POLITECNICO
MILANO 1863

POLITECNICO DI MILANO
Corso di Laurea Magistrale in Ingegneria Elettrica
Dipartimento di Elettronica, Informazione e Bioingegneria

BEM Reconstruction of 2D Magnetic Field Maps from Measured Boundary Data in Accelerator Magnets

Relatore: Prof. Luca Di Rienzo
Correlatore: Dr. Stephan Russenschuck

Tesi di Laurea di:
Biccioli Leonardo
Matricola 854792

Anno Accademico 2016-2017

Abstract

IT La mappatura del campo magnetico all'interno dei magneti per acceleratori è uno dei compiti principali della sezione di misure magnetiche al CERN. Allo stato dell'arte, la misura del campo all'interno dell'apertura dei magneti viene effettuata per mezzo di bobine rotanti. Lo scopo di questa tesi è quello di investigare una soluzione alternativa che permetta di ottenere una mappatura 2D completa dell'apertura del magnete partendo dalle misure effettuate sul contorno. Le misure acquisite con la tecnica del filo teso sono processate e usate come condizioni al contorno per un problema di Dirichlet risolto con il Boundary Element Method (BEM).

EN The magnetic field mapping in accelerator magnets is one of the main competences of the magnetic measurements section at CERN. Rotating Coil Magnetometers are state-of-the-art devices for measuring integrated fields in the magnet aperture. The aim of this thesis is to investigate an alternative sampling technique which allows a two-dimensional field map reconstruction in the entire magnet aperture starting from measured boundary data. Stretched-wire measurements are processed and used as boundary conditions of a boundary value problem solved by means of the Boundary Element Method (BEM).

Contents

List of Figures

List of Tables

Chapter 1

Introduction

The European Organization for Nuclear Research, known as CERN, is a research organization that operates the largest particle physics laboratory in the world. Established in 1954, the organization is based in a northwest suburb of Geneva on the Franco-Swiss border, and its main function is to provide the particle accelerators and other infrastructure needed for high-energy physics research.

1.1 The accelerators technology

Accelerators were invented in the 1930s to provide energetic particles to investigate the structure of the atomic nucleus. Since then, they have been used to examine many aspects of particle physics. Their job is to speed up and increase the energy of a beam of particles, by generating electric fields that accelerate the particles and magnetic fields that steer and focus them. These experimental facilities come either in the form of a ring (circular accelerators), where a beam of particles travels repeatedly round a loop, or in a straight line (linear accelerators), where the particle beam travels from one end to the other. The type of particle used depends on the aim of the experiment. In particular, at CERN, a number of accelerators are joined together in sequence to reach successively higher energies [1].

1.2 The Large Hadron Collider

The Large Hadron Collider (LHC) is the world's largest and most powerful particle accelerator. It consists of a 27 kilometer underground ring, shown in Fig. 1.1, of superconducting magnets with a number of accelerating structures to boost the energy of the particles along the way. Inside the accelerator, two high-energy particle beams travel at close to the speed of light before they are made to collide. The beams travel in opposite directions in separate beam pipes (two tubes kept at ul-

trahigh vacuum). They are guided around the accelerator ring by a strong magnetic field maintained by superconducting electromagnets, which are built from coils of special electric cable that operates in a superconducting state, efficiently conducting electricity without resistance or loss of energy. This requires chilling the magnets to -271.3 ℃, a temperature colder than outer space. For this reason, much of the accelerator is connected to a distribution system of liquid helium, which cools the magnets, as well as to other supply services.

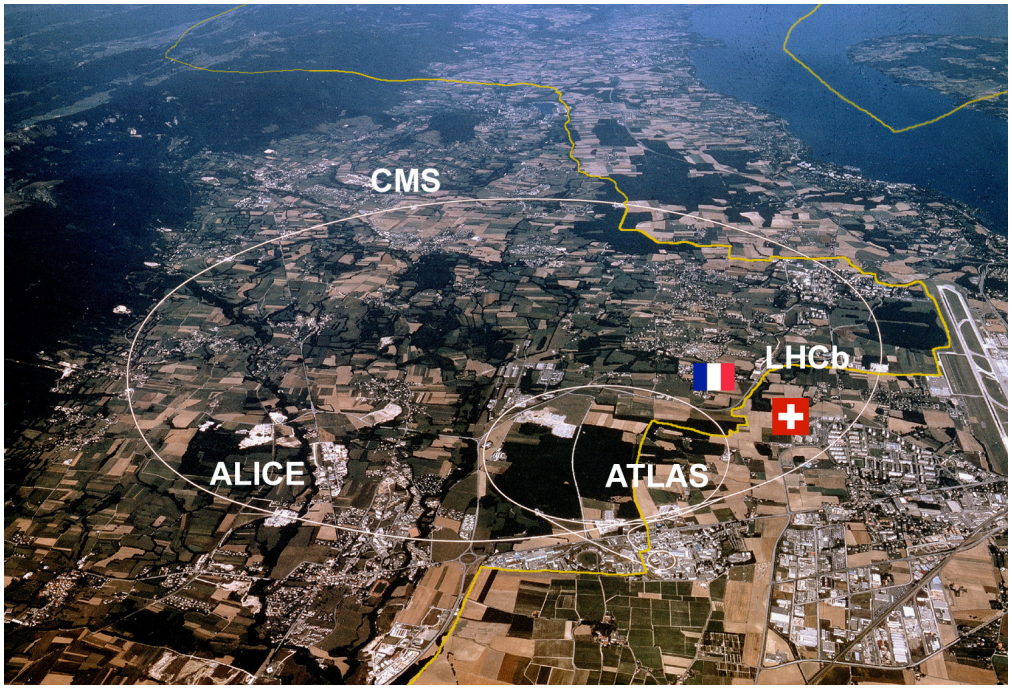

Figure 1.1: Layout of the LHC main ring with its physics experiments ATLAS, CMS, ALICE and LHC-B.

Thousands of magnets of different varieties and sizes are used to direct the beams around the accelerator. These include 1232 dipole magnets 15 meters in length which bend the beams, and 392 quadrupole magnets, each 5-7 meters long, which focus the beams. Just prior to collision, another type of magnet is used to "squeeze" the particles closer together to increase the chances of collisions [2].

The eight arcs of the main ring are composed of 23 regular arc cells of the so called FODO structure, schematically shown in Fig. 1.2. Each cell is made of two identical half-cells, each one consisting of a string of three main dipoles (MB) and one main quadrupole (MQ). Sextupole, decapole and octupole correctors are located at the ends of the main dipoles [3].

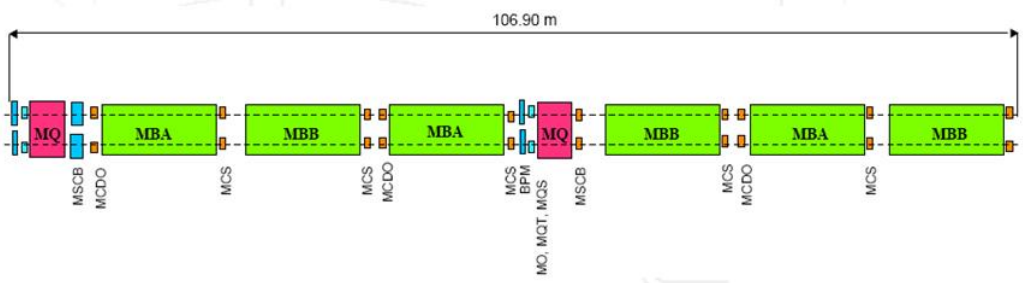

Figure 1.2: Layout of the FODO cells of the LHC main ring. Multipole corrector magnets are connected to the main dipoles (MBA and MBB).

1.3 The magnetic measurement section at CERN

The Magnets, Superconductors and Cryostats group, as a part of the CERN Technology Department, manages the development of the technology for accelerator magnets. One of the sections of this group is the magnetic measurement section, which is responsible for everything that concerns magnetic measurements in accelerator physics.

There are two principal working areas, the R&D area and the measurement area. The former deals with the study of the theory that governs the magnetic field and with the design of future measurements systems; the latter, instead, is in charge for the measurement of customer's magnets using well-known and well-proven techniques. Typical section's customers are the CERN itself but even external entities like research centers or private companies.

Different techniques are used to measure the field produced in the magnet aperture depending on the characteristic that has to be evaluated, which can be the transfer function, the magnetic axis, the field quality and harmonics or dynamic effects and transients. Here a list of the available techniques [4]:

- Rotating coils: the analysis of the flux intercepted by rotating a coil inside the magnet aperture provides information about the strength, the direction and the quality of the field.

- Stretched-wire: a conducting wire is inserted along the magnet aperture. The voltage induced by a displacement of the wire or the oscillations induced by an AC current flowing into the wire can be analyzed in order to retrieve a measurement of some characteristics of the integral field.

- 3D mapper: by means of a Hall sensor precisely driven into the magnet aperture, a map of the field can be drawn.

- Fluxmeters: one or more coils are positioned in the magnet aperture, and the voltage induced by a field change is measured.
- Nuclear magnetic resonance: sensors based on this principles are used only on dipoles. It is the most accurate techniques for measuring the absolute field. It is often used for the calibration of other sensors.
- 3D survey: by using a laser interferometer, precise measurements of the position of a geometrical point surrounding the magnet with respect to some reference points can be exploited.

Chapter 2

The Boundary Integral Equation Method

Nearly all physical phenomena occurring in nature can be described by differential equations. Boundary integral equations are reformulations for the solution of partial differential equations problems. The method is based on a mathematical formulation which reduces the dimensionality of a problem from $\mathbb{R}^n$ to $\mathbb{R}^{n-1}$. In the following, preliminary mathematical concepts are developed for a complete characterization of the boundary integral equation method in two dimensions.

2.1 The Gauss-Green theorem

This theorem is a fundamental identity, which relates the integral of the derivative of a function $f = f(x, y)$ over a domain Ω to the integral of that function on its boundary Γ. For the 2D case, consider the plane domain Ω bounded by the curve Γ [5]. Firstly, the relation for the derivative with respect to x is developed; then, the one related to the derivative on y is consequently obtained by interchanging the variables. The integral over Ω may be written as a double integral, for which the integration is carried out first with respect to x and then with respect to y. It is possible to write

$$\int_\Omega \frac{\partial f}{\partial x} d\Omega = \int_{y_1}^{y_2} \left(\int_{x_1}^{x_2} \frac{\partial f}{\partial x} dx \right) dy = \int_{y_1}^{y_2} \{ f(x_2, y) - f(x_1, y) \} dy \ , \tag{2.1}$$

where $x_1 = x_1(y)$ and $x_2 = x_2(y)$.

Considering Fig. 2.1 and focusing on the detail we get

$$\begin{aligned} \frac{dy}{ds} &= \cos\alpha = n_x \quad \rightarrow \quad dy = n_x ds \ , \\ -\frac{dx}{ds} &= \sin\alpha = n_y \quad \rightarrow \quad dx = -n_y ds \ , \end{aligned}$$

where n_x and n_y are the components of the unit vector $\mathbf{n}$ normal to the boundary Γ. The negative sign is due to the fact that dx and $\sin\alpha$ have opposite sign when the angle α is measured in the counterclockwise sense with respect to the positive x-direction.

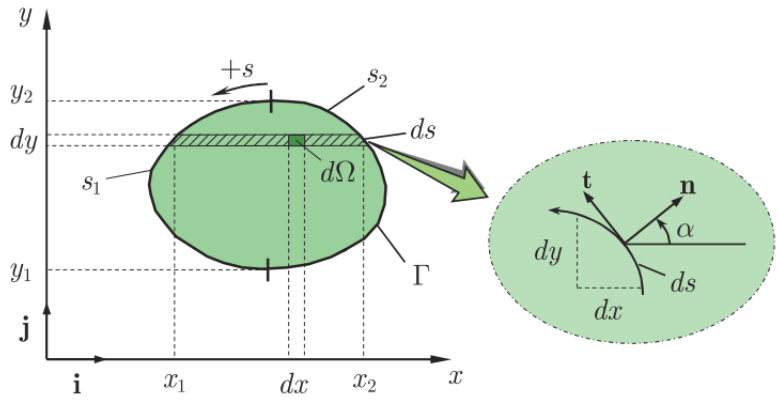

Figure 2.1: Integration over a plane domain Ω bounded by a curve Γ.

Consequently, (2.1) becomes

$$\int_{y_1}^{y_2} \{f(x_2,y) - f(x_1,y)\}dy = \int_{s_2} f(x_2,y)n_x ds - \int_{s_1} f(x_1,y)n_x ds \ . \tag{2.2}$$

The integration on s_1 is performed in the negative direction, i.e. clockwise, when y varies from y_1 to y_2.

Using uniform direction for the integration over s, both terms in (2.2) can be combined in a single expression

$$\int_\Omega \frac{\partial f}{\partial x} d\Omega = \int_\Gamma f n_x ds \ . \tag{2.3}$$

Interchanging x with y, the same expression is obtained for the second coordinate

$$\int_\Omega \frac{\partial f}{\partial y} d\Omega = \int_\Gamma f n_y ds \ . \tag{2.4}$$

If another function $g = g(x,y)$ is introduced, then (2.3) and (2.4) result in

$$\int_\Omega \frac{\partial (fg)}{\partial x} d\Omega = \int_\Omega \frac{\partial f}{\partial x} g d\Omega + \int_\Omega f \frac{\partial g}{\partial x} d\Omega = \int_\Gamma f g n_x ds \ , \tag{2.5}$$

$$\int_\Omega \frac{\partial (fg)}{\partial y} d\Omega = \int_\Omega \frac{\partial f}{\partial y} g d\Omega + \int_\Omega f \frac{\partial g}{\partial y} d\Omega = \int_\Gamma f g n_y ds \ . \tag{2.6}$$

Equations (2.5) and (2.6) state the integration by parts in two dimensions and are known as the Gauss-Green theorem.

2.2 The divergence theorem of Gauss

The divergence theorem results readily as an application of the Gauss-Green theorem. Consider the vector field $\mathbf{u} = u\mathbf{i} + v\mathbf{j}$, where $\mathbf{i}$ and $\mathbf{j}$ denote the unit vectors along the x and the y axes, respectively, while $u = u(x, y)$ and $v = v(x, y)$ denotes its components. Applying (2.3) for $f = u$, (2.4) for $f = v$ and adding them together, results

$$\int_{\Omega} \left(\frac{\partial u}{\partial x} + \frac{\partial v}{\partial y} \right) d\Omega = \int_{\Gamma} (u n_x + v n_y)\, ds \ . \tag{2.7}$$

If the coordinates x and y are represented by x_1 and x_2 respectively, then the components of the vector field $\mathbf{u}$ are denoted by u_i $(i = 1, 2)$ and those of the normal vector $\mathbf{n}$ by n_i. At this point (2.7) can be written as

$$\int_{\Omega} \left(\frac{\partial u_1}{\partial x_1} + \frac{\partial u_2}{\partial x_2} \right) d\Omega = \int_{\Gamma} (u_1 n_1 + v_2 n_2)\, ds \ , \tag{2.8}$$

or using the summation convention

$$\int_{\Omega} \left(\frac{\partial u_i}{\partial x_i} \right) d\Omega = \int_{\Gamma} (u_i n_i)\, ds \ . \tag{2.9}$$

Finally, (2.7), (2.8) and (2.9) can be written using vector notation as

$$\int_{\Omega} (\nabla \cdot \mathbf{u})\, d\Omega = \int_{\Gamma} (\mathbf{u} \cdot \mathbf{n})\, ds \ . \tag{2.10}$$

The quantity $\nabla \cdot \mathbf{u}$ is referred to as the divergence of a vector field $\mathbf{u}$ at a point inside the domain Ω, whereas the quantity $\mathbf{u} \cdot \mathbf{n}$ is referred to as the flux of the vector field directed in the $\mathbf{n}$ direction at a single point on the boundary Γ. Equation (2.10) is known as the divergence theorem of Gauss, and relates the total divergence to the total flux of a vector field.

2.3 Green's second identity

Consider the functions $u = u(x, y)$ and $v = v(x, y)$ which are twice continuously differentiable in Ω and once in Γ. Applying (2.5) for $g = v$, $f = \partial u/\partial x$ and also (2.6) for $g = v$, $f = \partial u/\partial y$, and finally adding the resulting equations, results

$$\begin{aligned} \int_{\Omega} v \left(\frac{\partial^2 u}{\partial x^2} + \frac{\partial^2 u}{\partial y^2} \right) d\Omega = &- \int_{\Omega} \left(\frac{\partial u}{\partial x}\frac{\partial v}{\partial x} + \frac{\partial u}{\partial y}\frac{\partial v}{\partial y} \right) d\Omega \\ &+ \int_{\Gamma} v \left(\frac{\partial u}{\partial x} n_x + \frac{\partial u}{\partial y} n_y \right) ds \ . \end{aligned} \tag{2.11}$$

Similarly, applying (2.5) for $g = u$, $f = \partial v/\partial x$ and (2.6) for $g = u$, $f = \partial v/\partial y$, and finally adding the resulting equations

$$\begin{aligned}\int_\Omega u\left(\frac{\partial^2 v}{\partial x^2}+\frac{\partial^2 v}{\partial y^2}\right)d\Omega = &-\int_\Omega\left(\frac{\partial u}{\partial x}\frac{\partial v}{\partial x}+\frac{\partial u}{\partial y}\frac{\partial v}{\partial y}\right)d\Omega \\ &+\int_\Gamma u\left(\frac{\partial v}{\partial x}n_x+\frac{\partial v}{\partial y}n_y\right)ds\ .\end{aligned} \tag{2.12}$$

Subtracting (2.12) from (2.11) yields

$$\int_\Omega\left(v\nabla^2 u - u\nabla^2 v\right)d\Omega = \int_\Gamma\left(v\frac{\partial u}{\partial \mathbf{n}}-u\frac{\partial v}{\partial \mathbf{n}}\right)ds\ , \tag{2.13}$$

where the Laplacian ∇^2 is defined as

$$\nabla^2 = \nabla\cdot\nabla = \left(\mathbf{i}\frac{\partial}{\partial x}+\mathbf{j}\frac{\partial}{\partial y}\right)\cdot\left(\mathbf{i}\frac{\partial}{\partial x}+\mathbf{j}\frac{\partial}{\partial y}\right) = \frac{\partial^2}{\partial x^2}+\frac{\partial^2}{\partial y^2}\ , \tag{2.14}$$

while

$$\frac{\partial}{\partial \mathbf{n}} = \mathbf{n}\cdot\nabla = (n_x\mathbf{i}+n_y\mathbf{j})\cdot\left(\mathbf{i}\frac{\partial}{\partial x}+\mathbf{j}\frac{\partial}{\partial y}\right) = n_x\frac{\partial}{\partial x}+n_y\frac{\partial}{\partial y}\ , \tag{2.15}$$

is the operator that produces the derivative of a scalar function in the direction of $\mathbf{n}$. Equation (2.13) is known as Green's second identity for ∇^2.

2.4 The Laplace equation

In mathematics, the second-order partial differential equation

$$\nabla^2 u = 0\ , \tag{2.16}$$

is known as the Laplace's equation. Defined Ω as an open and bounded subset of $\mathbb{R}^2$, the harmonic function u is a twice continuously differentiable function which satisfies $\nabla^2 u = 0$ everywhere on Ω.

2.4.1 Maximum principle

If u is an harmonic function on a bounded domain Ω in $\mathbb{R}^2$, then u attains its maximum value on the boundary Γ

$$\max_{\overline{\Omega}} u(x,y) = \max_{\Gamma} u(x,y)\ , \tag{2.17}$$

where $\overline{\Omega} = \Omega\cup\Gamma$. Consequently, if there is a point $(x_0, y_0)\in\Omega$ such that

$$u(x_0,y_0) = \max_{\overline{\Omega}} u(x,y)\ , \tag{2.18}$$

then u is definitely constant within Ω.

2.5 The boundary value problem

A boundary value problem is a differential equation together with a set of additional constraints, called boundary conditions, specified at the extremes of the connected domain. A solution to a boundary value problem is a solution to the differential equation which also satisfies the boundary conditions. To be useful in applications, a boundary value problem must be well posed. This means that given the input to the problem, there exists a unique solution, which depends continuously on the input.

In magnetostatics, a common problem is to find a function which describes the magnetic potential in a given region. If the region does not contain sources, the potential is a solution of the Laplace's equation (a so-called harmonic function). The boundary conditions in this case are the interface conditions for magnetic fields. Two-dimensional potential problems, defined in the xy-plane, are described by the equation

$$\nabla^2 u = f(x, y) \ , \tag{2.19}$$

whose solution $u = u(x, y)$ represents the potential produced at point (x, y) in the bounded domain Ω due to a source $f(x, y)$ distributed over Ω.

For $f(x, y) = 0$, the governing equation translates into the Laplace's equation, whose solution is sought in a closed plane domain Ω, having a boundary Γ on which either the function u or its derivative in the direction normal to the boundary is prescribed: this solution must satisfy the boundary conditions of the problem. Consequently, one can classify different boundary value problems on Γ, where the quantities denoted by $\bar{f}$ are known functions defined on the boundary

$$\nabla^2 u = f \quad \text{in } \Omega \quad \begin{cases} u = \bar{u} \quad \text{on } \Gamma \quad \Rightarrow \quad \text{Dirichlet problem} \\ \dfrac{\partial u}{\partial \mathbf{n}} = \partial_{\mathbf{n}} \bar{u} \quad \text{on } \Gamma \quad \Rightarrow \quad \text{Neumann problem} \\ \begin{array}{l} u = \bar{u} \quad \text{on } \Gamma_1 \\ \dfrac{\partial u}{\partial \mathbf{n}} = \partial_{\mathbf{n}} \bar{u} \quad \text{on } \Gamma_2 \end{array} \quad \Rightarrow \quad \text{Mixed problem} \end{cases} . \tag{2.20}$$

2.6 The fundamental solution

Consider a source point placed at $P(x, y)$ of the xy-plane. Its density at $Q(\xi, \eta)$ may be expressed mathematically by the delta function as

$$f(Q) = \delta(Q - P) \ , \tag{2.21}$$

and the potential $v = v(Q, P)$ produced at point Q satisfies the equation

$$\nabla^2 v = \delta(Q - P) \ . \tag{2.22}$$

A singular particular solution of (2.22) is called fundamental solution of the potential equation (2.19) [5]. It is determined by writing (2.22) in polar coordinates with origin at the source point P, such that it becomes

$$\frac{1}{r}\frac{d}{d\mathbf{r}}\left(r\frac{dv}{d\mathbf{r}}\right) = \delta(Q - P) \ , \tag{2.23}$$

where the absolute value of the vector $\mathbf{r}$ is defined as

$$r = |Q - P| = \sqrt{(\xi - x)^2 + (\eta - y)^2} \ , \tag{2.24}$$

being the solution axis-symmetric with respect to the source and consequently independent on the polar angle.

The right hand side of the last equation vanishes at all points of the plane, except at the origin $r = 0$, where it has an infinite value

$$\frac{1}{r}\frac{d}{d\mathbf{r}}\left(r\frac{dv}{d\mathbf{r}}\right) = 0 \ , \tag{2.25}$$

which gives, after integrating twice

$$v = A \ln r + B \ , \tag{2.26}$$

where A and B are arbitrary constants. Since a particular solution has to be found, B is set to 0, while A is determined from

$$A\frac{1}{r} = \frac{\partial v}{\partial \mathbf{r}} = \frac{\partial v}{\partial \mathbf{n}} \ , \tag{2.27}$$

and $ds = r d\Theta$. Application of Green's identity for $u = 1$ and $v = A \ln r$ yields

$$-\int_\Omega \nabla^2 v d\Omega = -\int_\Gamma \frac{\partial v}{\partial \mathbf{n}} ds \ , \tag{2.28}$$

where Ω is the circle with center P and radius ρ, as shown in Fig. 2.2.

Using (2.22) and (2.26), noting that for points on Γ it is $\rho = r$, the relation is written as

$$-\int_\Omega \delta(Q - P) d\Omega = -\int_0^{2\pi} A\frac{1}{\rho}\rho d\theta \ , \tag{2.29}$$

that is, for the property of the delta function, equivalent to

$$1 = 2\pi A \quad \Rightarrow \quad A = \frac{1}{2\pi} \ . \tag{2.30}$$

Hence, the fundamental solution becomes

$$v = \frac{1}{2\pi} \ln r \ , \tag{2.31}$$

which is also known as free space Green's function.

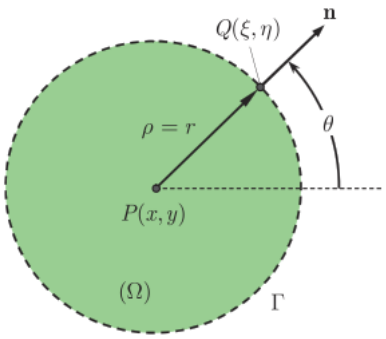

Figure 2.2: Circular domain with source point P at the center.

2.7 The representation formula

The next step is to represent the solution of the partial differential equation in the domain Ω by means of boundary conditions defined along Γ. We assume a problem with mixed boundary conditions

$$\begin{aligned} u &= \bar{u} \quad \text{on} \quad \Gamma_1 \ , \\ \frac{\partial u}{\partial \mathbf{n}} &= \partial_{\mathbf{n}} \bar{u} \quad \text{on} \quad \Gamma_2 \ , \end{aligned}$$

where $\Gamma = \Gamma_1 \cup \Gamma_2$.

Applying Green's second identity for the functions u and v that satisfy (2.16) and (2.22) in Ω, respectively

$$\begin{aligned} \nabla^2 u &= 0 \ , \\ \nabla^2 v &= \delta(Q-P) \ , \end{aligned}$$

and assuming that the source lies at point P, follows

$$-\int_{\Omega} u(Q)\delta(Q-P)d\Omega_Q = \int_{\Gamma} \left[v(q,P)\frac{\partial u(q)}{\partial \mathbf{n}_q} - u(q)\frac{\partial v(q,P)}{\partial \mathbf{n}_q} \right] ds_q \ , \tag{2.32}$$

where P, $Q \in \Omega$ and $q \in \Gamma$.

The last equation can be written also in the following formulation

$$u(P) = -\int_{\Gamma} \left[v(P,q)\frac{\partial u(q)}{\partial \mathbf{n}_q} - u(q)\frac{\partial v(P,q)}{\partial \mathbf{n}_q} \right] ds_q \ , \tag{2.33}$$

called representation formula (or integral representation) for the solution of the partial differential equation. The solution u is represented as the sum of two parts, called simple-layer and double-layer potential, respectively.

The terms related to the fundamental solution are both known quantities at any point q on the boundary

$$v = \frac{1}{2\pi} \ln r \ ,$$
$$\frac{\partial v}{\partial \mathbf{n}} = \frac{1}{2\pi} \frac{\cos \phi}{r} \ ,$$

with $r = |q - P|$ and $\phi = \angle(\mathbf{r}, \mathbf{n})$.

In order to solve the boundary problem and then find a solution for the entire domain starting from boundary conditions, it is necessary to extend the integral representation to the general case of P belonging to any position in the 2D plane. The general equation is defined as

$$\epsilon(P) u(P) = - \int_\Gamma \left[v(P,q) \frac{\partial u(q)}{\partial \mathbf{n}_q} - u(q) \frac{\partial v(P,q)}{\partial \mathbf{n}_q} \right] ds_q \ , \tag{2.34}$$

where $\epsilon(P)$ is a coefficient which depends on the position of point P

$$\epsilon(P) = \begin{cases} 1 & \text{for } P \text{ inside } \quad \Omega \\ \alpha/2\pi & \text{for } P \text{ on the boundary } \quad \Gamma \\ 0 & \text{for } P \text{ outside } \quad \Omega \end{cases} \ , \tag{2.35}$$

where α is the angle between the tangents of the boundary Γ at point P.

The general formulation constitutes a compatibility relation between the boundary values of the potential u and its derivative with respect to the normal direction, meaning that only one of the two quantities can be prescribed at each point of the boundary.

2.8 The boundary value problem in magnetostatics

In Appendix C it is proved that both the scalar potential ϕ_m and the vector potential $\mathbf{A}$ obey the Laplace's equation (2.16). Consequently, the solution at any point of a bounded domain Ω can be written in terms of (2.34). Follow

$$\epsilon \ \phi_m = - \int_\Gamma \left[v \frac{\partial \phi_m}{\partial \mathbf{n}} - \phi_m \frac{\partial v}{\partial \mathbf{n}} \right] ds \ , \tag{2.36}$$

$$\epsilon \ A_z = - \int_\Gamma \left[v \frac{\partial A_z}{\partial \mathbf{n}} - A_z \frac{\partial v}{\partial \mathbf{n}} \right] ds \ . \tag{2.37}$$

Important relations with the magnetic field $\mathbf{B}$ are derived applying (C.3) and (C.10) in 2D Cartesian coordinates

$$\mathbf{B} = \mathbf{i} \ \frac{\partial \phi_m}{\partial x} + \mathbf{j} \ \frac{\partial \phi_m}{\partial y} \ , \tag{2.38}$$

$$\mathbf{B} = \mathbf{i}\ \frac{\partial A_z}{\partial y} - \mathbf{j}\ \frac{\partial A_z}{\partial x}\ , \tag{2.39}$$

that lead to

$$B_x = +\frac{\partial \phi_m}{\partial x} = +\frac{\partial A_z}{\partial y}\ , \tag{2.40}$$

$$B_y = +\frac{\partial \phi_m}{\partial y} = -\frac{\partial A_z}{\partial x}\ . \tag{2.41}$$

This means that, for a boundary value problem formulated in ϕ_m or $\mathbf{A}$, one can compute the magnetic field $\mathbf{B}$ at any point P by means of the solution of (2.16) in the neighborhood of P.

Chapter 3

The Boundary Element Method

For practical applications, an exact solution of the integral equation (2.34) is not achievable. However, a numerical solution is feasible by employing the Boundary Element Method (BEM), which is able to solve the problem by the discretization of the boundary into a finite number of elements. This translates into the decomposition of Γ into a finite number of subsets, each of which has a regular parameter representation by some parameter domain in $\mathbb{R}^1$ [6]. Two approximations are carried out: one is about the geometry of the boundary, while the other has to do with the variation of the boundary quantities over the element. Depending on the degree of the polynomials used for these kind of approximations, the formulation can be classified as Sub-parametric, Iso-parametric or Super-parametric elements. The finitely many parameters determining the approximated solution are computed from finitely many linear equations. There are two methods to generate this system of discrete equations, Collocation and Galerkin method:

1. For the **Collocation method**, one chooses a suitable set of collocation points $\{p_i | i = 1, ..., I\} \subset \Gamma$ and requires that the equation (2.34) is satisfied in these points.

2. For the **Galerkin method**, one multiplies (2.34) for the approximated solution with test functions from a finite dimensional function space, integrates over Γ and equates the integrals.

As we will see, the collocation method is the simplest one because it involves only one integral, whereas the Galerkin requires two integrations. This may be the reason why collocation is the most frequently used in applications.

3.1 Collocation method

For the collocation method, one can distinguish, for each element, the end points and the nodal points. The first ones define the position of the element in the xy-plane, whereas the latter are the points at which values of the boundary quantities are assigned [5].

The discretized form, assumed J elements numbered in the counter-clockwise sense, is expressed for a given point p_i on Γ as

$$\epsilon(p_i)u(p_i) = -\sum_{j=1}^{J}\int_{\Gamma_j}\left[v(p_i,q)\frac{\partial u(q)}{\partial \mathbf{n}_q} - u(q)\frac{\partial v(p_i,q)}{\partial \mathbf{n}_q}\right]ds_q \ , \tag{3.1}$$

where Γ_j is the j-th element over which integration is carried out, p_i is the reference nodal point and $\epsilon(p_i)$ is the coefficient computed from (2.35).

It is possible to re-write (3.1) in a different form

$$\epsilon^i u^i = -\sum_{j=1}^{J}\int_{\Gamma_j} v\partial_{\mathbf{n}} u ds + \sum_{j=1}^{J}\int_{\Gamma_j} u\partial_{\mathbf{n}} v ds \ . \tag{3.2}$$

The last equation is applied consecutively for all the nodes p_i, yielding a system of linear algebraic equations.

3.1.1 Constant BEM

In case of constant boundary elements, the boundary element is approximated by a straight line, which connects its two extreme points. The node is placed at the mid point, while the boundary quantity is assumed to be constant along the element and equal to its value at the nodal point. Since the geometry is represented with high order polynomial than that used to approximate the boundary quantity, it is said to be depicted super-parametrically [7].

Given the last considerations, (3.2) becomes

$$-\frac{1}{2}u^i + \sum_{j=1}^{J}\left(\int_{\Gamma_j}\partial_{\mathbf{n}} v ds\right)u^j = \sum_{j=1}^{J}\left(\int_{\Gamma_j} v ds\right)\partial_{\mathbf{n}} u^j \ . \tag{3.3}$$

This result arises due to the fact that it is always $\alpha = \pi$ for the i-th boundary node placed at the mid-point, while the quantities u and $\partial_{\mathbf{n}} u$ are constant over the j-th element. The integrals involved in the above equation relate the node p_i, where the fundamental solution is applied, to the node p_j, where the boundary condition is

defined; they are often referred to as influence coefficients and defined as

$$\hat{H}_{ij} = \int_{\Gamma_j} \frac{\partial v(p_i, q)}{\partial \mathbf{n}_q} ds \ , \tag{3.4}$$

$$G_{ij} = \int_{\Gamma_j} v(p_i, q) ds \ , \tag{3.5}$$

where the reference point p_i remains constant while the integration point q varies over the j-th element.

Introducing the influence coefficients in (3.3), the solution becomes

$$-\frac{1}{2}u^i + \sum_{j=1}^{J} \hat{H}_{ij} u^j = \sum_{j=1}^{J} G_{ij} \partial_{\mathbf{n}} u^j \ . \tag{3.6}$$

Moreover, setting

$$H_{ij} = \hat{H}_{ij} - \frac{1}{2}\delta_{ij} \quad \begin{cases} \delta_{ij} = 0 & \text{for } i \neq j \\ \delta_{ij} = 1 & \text{for } i = j \end{cases} \ , \tag{3.7}$$

results the following liner system of equations

$$\sum_{j=1}^{J} H_{ij} u^j = \sum_{j=1}^{J} G_{ij} \partial_{\mathbf{n}} u^j \quad \Rightarrow \quad [H]\{u\} = [G]\{\partial_{\mathbf{n}} u\} \ . \tag{3.8}$$

3.1.2 Linear BEM

For linear elements, the boundary element is approximated again by a straight line connecting its end points. Two nodes are placed at the extreme points of the element and the boundary quantity is assumed to vary linearly between the nodal values. Since the geometry and the boundary quantity are approximated over the element by polynomials of the same degree, the former is said to be depicted iso-parametrically.

In order to establish the expression for the variation of the boundary quantity over the j-th element, it is convenient to introduce a local coordinate system, as shown in Fig. 3.1. In the local system of axes

$$-\frac{l_j}{2} \leq x' \leq +\frac{l_j}{2} \quad , \quad y = 0 \ ,$$

whereas in the global system of axes

$$x = \frac{x_{j+1} + x_j}{2} + \frac{x_{j+1} - x_j}{l_j} x' \ ,$$
$$y = \frac{y_{j+1} + y_j}{2} + \frac{y_{j+1} - y_j}{l_j} y' \ .$$

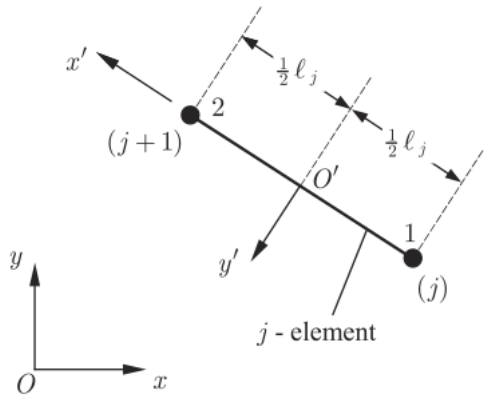

Figure 3.1: Global and local system of axes for the element j.

The interval $[-l_j/2, +l_j/2]$ is then normalized by the introduction of a parameter ξ defined as

$$\xi = \frac{x'}{l_j/2} \ ,$$

and it finally results the expression of the global coordinates as a function of ξ

$$\begin{aligned} x &= \frac{x_{j+1} + x_j}{2} + \frac{x_{j+1} - x_j}{2}\xi \\ y &= \frac{y_{j+1} + y_j}{2} + \frac{y_{j+1} - y_j}{2}\xi \end{aligned} \quad \Rightarrow \quad \begin{aligned} x(\xi) &= \frac{1}{2}(1-\xi)x_j + \frac{1}{2}(1+\xi)x_{j+1} \\ y(\xi) &= \frac{1}{2}(1-\xi)y_j + \frac{1}{2}(1+\xi)y_{j+1} \end{aligned} \ ,$$

where

$$-1 \leq \xi \leq +1 \ .$$

Since a linear element is defined iso-parametrically, the same considerations hold for the variation of the boundary quantity, leading to a general equation

$$f(\xi) = \psi_1(\xi) f_1 + \psi_2(\xi) f_2 \ , \tag{3.9}$$

where $f_1$and f_2 are the values of the function $f(x)$ at the nodes 1 (or j) and 2 (or $j+1$), and $f(\xi)$ represents any of the functions $x(\xi)$, $y(\xi)$, $u(\xi)$ or $u_n(\xi)$. The remaining terms are referred to as linear shape functions

$$\begin{aligned} \psi_1(\xi) &= \frac{1}{2}(1-\xi) \ , \\ \psi_2(\xi) &= \frac{1}{2}(1+\xi) \ . \end{aligned} \tag{3.10}$$

Using the linear approximation (3.9) for the boundary quantities, the line integrals appearing in (3.2) become

$$\int_{\Gamma_j} v\partial_{\mathbf{n}} u ds = \int_{-1}^{+1} v\left[\psi_1(\xi)\partial_{\mathbf{n}} u^1 + \psi_2(\xi)\partial_{\mathbf{n}} u^2\right]\frac{l_j}{2}d\xi = g_1^{ij}\partial_{\mathbf{n}} u^1 + g_2^{ij}\partial_{\mathbf{n}} u^2 \ , \quad (3.11)$$

$$\int_{\Gamma_j} u\partial_{\mathbf{n}} v ds = \int_{-1}^{+1} \partial_{\mathbf{n}} v\left[\psi_1(\xi)u^1 + \psi_2(\xi)u^2\right]\frac{l_j}{2}d\xi = h_1^{ij}u^1 + h_2^{ij}u^2 \ , \quad (3.12)$$

where the coefficients are

$$g_{1/2}^{ij} = \frac{l_j}{2}\int_{-1}^{+1} v\psi_{1/2}(\xi)d\xi \ , \quad (3.13)$$

$$h_{1/2}^{ij} = \frac{l_j}{2}\int_{-1}^{+1} \partial_{\mathbf{n}} v\psi_{1/2}(\xi)d\xi \ , \quad (3.14)$$

and the fundamental solution

$$v = \frac{1}{2\pi}\ln(r) \ ,$$
$$\frac{\partial v}{\partial \mathbf{n}} = \frac{1}{2\pi}\frac{\cos\phi}{r} \ ,$$

considering the radius $r = \sqrt{[x(\xi) - x_i]^2 + [y(\xi) - y_i]^2}$ as the distance between the source point and the boundary integration point.

Substituting (3.11) and (3.12) back into (3.2), the latter yields

$$-\epsilon^i u^i + \sum_{j=1}^{J}\hat{H}_{ij}u^j = \sum_{j=1}^{J} G_{ij}\partial_{\mathbf{n}} u^j \ , \quad (3.15)$$

where

$$\hat{H}_{ij} = \begin{cases} h_1^{i1} + h_2^{iJ} & \text{for} \quad j = 1 \\ h_1^{ij} + h_2^{ij-1} & \text{for} \quad j = 2, 3, \ldots, J \end{cases} \ ,$$

$$G_{ij} = \begin{cases} g_1^{i1} + g_2^{iJ} & \text{for} \quad j = 1 \\ g_1^{ij} + g_2^{ij-1} & \text{for} \quad j = 2, 3, \ldots, J \end{cases} \ .$$

Equation (3.15) may be written in matrix form as

$$[H]\{u\} = [G]\{\partial_{\mathbf{n}} u\} \ , \quad (3.16)$$

defined

$$[H] = -[\epsilon] + \left[\hat{H}\right] \ ,$$

where $[\epsilon]$ is a diagonal matrix with elements the coefficients $\epsilon^i = \alpha_i/2\pi$ (α_i is the angle between the elements i and $i-1$).

3.1.3 Quadratic BEM

Constant and linear elements cannot approximate with sufficient accuracy the geometry of curvilinear boundaries. For this reason, it is recommended to use curvilinear elements, for which the polynomials are of degree higher than one.

For quadratic elements, the geometry is approximated by a parabolic arc, connecting the two end points with the mid one. Thus, each element has three nodes placed at the extreme and mid points, while the boundary quantity is assumed to vary quadratically between the nodal values. Since the geometry and the boundary quantity are approximated over the element by polynomials of the same degree, the former is said to be depicted iso-parametrically.

When a quadratic variation is assumed, the boundary quantities are expressed by a polynomial of the form

$$f(s) = \alpha_0 + \alpha_1 s + \alpha_2 s^2 \ . \tag{3.17}$$

The coordinates of the point (x, y) lying on the boundary Γ are also functions of s, i.e. $x = x(s)$ and $y = y(s)$. Consequently $v = v(s)$ and $\partial_{\mathbf{n}} v = \partial_{\mathbf{n}} v(s)$ too.

In order to perform line integrations, the interval is normalized with respect to the intrinsic coordinate ξ, leading to the transformation

$$I = \int_{\Gamma_j} w(s) ds \quad \Rightarrow \quad I = \int_{-1}^{+1} w^*(\xi) |J(\xi)| d\xi \ , \tag{3.18}$$

where $|J(\xi)|$ is the Jacobian of the transformation, which maps the parabolic arc Γ_j of the xy-plane onto the straight line segment with $\eta = 0$ and $-1 \leq \xi \leq +1$ of the $\eta\xi$-plane

$$ds = \sqrt{dx^2 + dy^2} = \sqrt{[x'(\xi)]^2 + [y'(\xi)]^2}\ d\xi \ ,$$

the expression of the jacobian is

$$|J(\xi)| = \sqrt{[x'(\xi)]^2 + [y'(\xi)]^2} \ . \tag{3.19}$$

Fig. 3.2 shows graphically the normalization and the mapping of the quadratic element.

The boundary quantity is approximated directly in the interval $[-1, +1]$ by a second order polynomial in ξ, according to (3.17)

$$f(\xi) = \alpha_0 + \alpha_1 \xi + \alpha_2 \xi^2 \ . \tag{3.20}$$

The coefficients α_0, α_1 and α_2 are determined from the requirement that the function takes the nodal values f_1, f_2 and f_3 at points $\xi = -1, 0, +1$, respectively. Results

$$\begin{cases} f(-1) = & f_1 = \alpha_0 - \alpha_1 + \alpha_2 \\ f(0) = & f_2 = \alpha_0 \\ f(+1) = & f_3 = \alpha_0 + \alpha_1 + \alpha_2 \end{cases} \quad \Rightarrow \quad \begin{cases} \alpha_0 = & f_2 \\ \alpha_1 = & \dfrac{f_3 - f_1}{2} \\ \alpha_2 = & \dfrac{f_1 - 2f_2 + f_3}{2} \end{cases} \ .$$

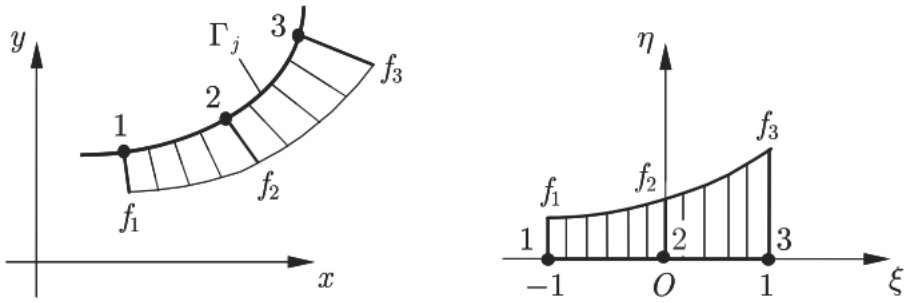

Figure 3.2: Quadratic element in global and local coordinate system.

Introducing the resulting coefficients in (3.20), the expression of the boundary quantity in terms of the three nodal values becomes

$$f(\xi) = f_2 + \frac{f_3 - f_1}{2}\xi + \frac{f_1 - 2f_2 + f_3}{2}\xi^2 = \psi_1(\xi)f_1 + \psi_2(\xi)f_2 + \psi_3(\xi)f_3 \ ,$$

where the shape functions for the quadratic element are

$$\begin{aligned}
\psi_1(\xi) &= -\frac{1}{2}\xi(1-\xi) \ , \\
\psi_2(\xi) &= (1-\xi)(1+\xi) \ , \\
\psi_3(\xi) &= +\frac{1}{2}\xi(1+\xi) \ .
\end{aligned}$$

Since a quadratic element is depicted iso-parametrically, the same considerations hold also for the geometry, which leads to

$$\begin{aligned}
x(\xi) &= \psi_1(\xi)x_1 + \psi_2(\xi)x_2 + \psi_3(\xi)x_3 \ , \\
y(\xi) &= \psi_1(\xi)y_1 + \psi_2(\xi)y_2 + \psi_3(\xi)y_3 \ .
\end{aligned}$$

Finally, the Jacobian can be expressed as

$$|J(\xi)| = \sqrt{[x'(\xi)]^2 + [y'(\xi)]^2} = \sqrt{(b_1 + 2b_2\xi)^2 + (c_1 + 2c_2\xi)^2} \ , \tag{3.21}$$

where

$$\begin{aligned}
b_1 &= \frac{x_3 - x_1}{2}, \quad b_2 = \frac{x_1 - 2x_2 + x_3}{2} \\
c_1 &= \frac{y_3 - y_1}{2}, \quad c_2 = \frac{y_1 - 2y_2 + y_3}{2}
\end{aligned} \quad .$$

Taking into account the quadratic variation of the boundary quantities on the elements, the line integrals of (3.2) yields

$$\begin{aligned}
\int_{\Gamma_j} v\partial_{\mathbf{n}} u ds &= \int_{-1}^{+1} v\left[\psi_1(\xi)\partial_{\mathbf{n}}u^1 + \psi_2(\xi)\partial_{\mathbf{n}}u^2 + \psi_3(\xi)\partial_{\mathbf{n}}u^3\right]\frac{l_j}{2}d\xi \\
&= g_1^{ij}\partial_{\mathbf{n}}u^1 + g_2^{ij}\partial_{\mathbf{n}}u^2 + g_3^{ij}\partial_{\mathbf{n}}u^3 \ ,
\end{aligned} \tag{3.22}$$

$$\begin{aligned}\int_{\Gamma_j} u\partial_{\mathbf{n}} v ds &= \int_{-1}^{+1} v_n \left[\psi_1(\xi)u^1 + \psi_2(\xi)u^2 + \psi_3(\xi)u^3\right] \frac{l_j}{2} d\xi \\ &= h_1^{ij}u^1 + h_2^{ij}u^2 + h_3^{ij}u^3 \ ,\end{aligned} \tag{3.23}$$

where, for $\alpha = 1, 2, 3$

$$\begin{aligned}g_\alpha^{ij} &= \int_{\Gamma_j} v\psi_\alpha ds \ , \\ h_\alpha^{ij} &= \int_{\Gamma_j} \psi_\alpha \partial_{\mathbf{n}} v ds \ .\end{aligned}$$

In order to evaluate the above integrals, their integrands are expressed in terms of the variable ξ

$$\begin{aligned}g_\alpha^{ij} &= \int_{-1}^{+1} \psi_\alpha(\xi) \frac{\ln r(\xi)}{2\pi} |J(\xi)| d\xi \ , \\ h_\alpha^{ij} &= \int_{-1}^{+1} \psi_\alpha(\xi) \frac{\cos\phi(\xi)}{2\pi r(\xi)} |J(\xi)| d\xi \ .\end{aligned}$$

It has to be highlighted that, in this formulation, the angle ϕ appearing in the kernel depends on ξ both for the radius r and the normal vector $\mathbf{n}$, due to the fact that the latter is a function of the position over the element for geometries with order higher than 1.

The boundary integral equation, for quadratic elements, is discretized as

$$\epsilon^i u^i + \sum_{j=1}^{J} \sum_{\alpha=1}^{3} h_\alpha^{ij} u_\alpha^j = \sum_{j=1}^{J} \sum_{\alpha=1}^{3} g_\alpha^{ij} \partial_{\mathbf{n}} u_\alpha^j \ , \tag{3.24}$$

where J is the total number of elements, the index i refers to the source point while the index j here refers to the boundary element. Since for the quadratic elements the number of nodes per element is three, the closed boundary is characterized by $I = 2J$ nodes [8].

Keeping in mind the last statement, important considerations follow. The index j, which until now has been associated to the j-th element, must be considered instead as the index that refers to the node q where the boundary condition is prescribed. In this way, even for quadratic elements, i and j are the row and column counters, respectively, while $I \times J$ is the size of square matrices. Results the general system

$$[H]\{u\} = [G]\{\partial_{\mathbf{n}} u\} \ , \tag{3.25}$$

where, applying previous considerations

$$\hat{H}_{ij} = \begin{cases} h_1^{i1} + h_3^{iJ} & \text{for } j = 1 \\ h_2^{ij} & \text{for j even } (j = 2, 4, \ldots, J) \\ h_1^{ij} + h_3^{ij-1} & \text{for j odd } (j = 3, 5, \ldots, J-1) \end{cases} , \tag{3.26}$$

$$G_{ij} = \begin{cases} g_1^{i1} + g_3^{iJ} & \text{for } j = 1 \\ g_2^{ij} & \text{for j even } (j = 2, 4, \ldots, J) \\ g_1^{ij} + g_3^{ij-1} & \text{for j odd } (j = 3, 5, \ldots, J-1) \end{cases} . \tag{3.27}$$

As a result, for quadratic elements the coefficients at the element end points have two terms, related to the forward and backward incidence, while those at element center points have only one term. As already mentioned, these influence coefficients relate node p_i, where the fundamental solution is applied, to the node p_j, where the boundary condition is prescribed.

3.1.4 Rearrangement of matrices

Since only one of the two boundary quantities is supposed to be known at each node, the resulting system of equations in the form (3.25) has to be rearranged on the basis of the boundary conditions. If the value of $\{u\}$ is unknown at a node, then the respective column of $[H]$ remains at the left hand side of (3.25), otherwise this column is multiplied by the known value of $\{u\}$, its sign is switched and is shifted to the right hand side of the equation. Similarly, if the value of $\{\partial_{\mathbf{n}} u\}$ is unknown, then the respective column of $[G]$ is shifted with opposite sign to the left hand side of the equation. The unknowns are rearranged by examining all the nodes of the boundary. After completing this process, the right hand side of the equation contains only known quantities and, thus, the matrix multiplication results in a single vector

$$[A]\{z\} = \{b\} . \tag{3.28}$$

The system (3.28) is solved for z, which is the vector of unknown boundary values.

3.1.5 Evaluation of line integrals

The matrices $[G]$ and $[H]$ appearing in the boundary integral equation require the computation of line integrals, whose integrands are products of the fundamental solution or its normal derivative. Two cases are dictated by the behavior of this solution: outside and inside integration.

In the former case, the line integrals are evaluated numerically using a standard Gaussian quadrature

$$\int_{-1}^{+1} f(\xi) d\xi = \sum_{k=1}^{K} \omega_k f(\xi_k) ,$$

where K is the number of integration/Gauss points, whereas ξ_k and ω_k are the abscissas and weights of the Gaussian quadrature of order k. This is the most suitable method for the numerical evaluation of BEM integrals, since it approximates the integral with great accuracy. The accuracy depends not only on the number of integration points, but also on how the integrand varies within the integration interval (a smooth variation of the integrand gives more accurate results).

In the latter case, the source lies on the element over which the integration is performed. As the integration point runs along the whole element, it will coincide inevitably with the source point. There, the distance r vanishes and the integrands exhibit a singular behavior, because the factors $\ln r$ and $\cos\phi/r$ become infinite for $r = 0$. These integrals are known as singular integrals, their value exists and is determined by special integration techniques. They are distinguished in integrals with logarithmic singularity and those with Cauchy singularity.

Constant BEM

- Outside integration ($i \neq j$)

  In this case the point p_i lies outside the j-th element, which means that the distance $r = |q_j - p_i|$ does not vanish and, consequently, the integral is regular.

  The numerical evaluation, after the transformation that maps the global coordinates onto the integration interval $[-1, +1]$, is carried out in the following way

  $$G_{ij} = \int_{-1}^{+1} \frac{1}{2\pi} \ln r(\xi) \frac{l_j}{2} d\xi = \frac{l_j}{4\pi} \sum_{k=1}^{K} \ln r(\xi_k) \omega_k \ . \tag{3.29}$$

  The first integral in (3.29) can also be evaluated analytically. Referring to the Fig. 3.3 and noticed that

  $$ds \cos\phi = r d\alpha \ ,$$

  which can be used to derive

  $$\hat{H}_{ij} = \int_{\Gamma_j} \frac{1}{2\pi} \frac{\cos\phi}{r} ds = \int_{\Gamma_j} \frac{1}{2\pi} d\alpha = \frac{\alpha_{j+1} - \alpha_j}{2\pi} \ , \tag{3.30}$$

  where the angles are computed as

  $$\tan\alpha_{j+1} = \frac{y_{j+1} - y_i}{x_{j+1} - x_i} \ ,$$
  $$\tan\alpha_j = \frac{y_j - y_i}{x_j - x_i} \ .$$

- Inside integration ($i = j$)

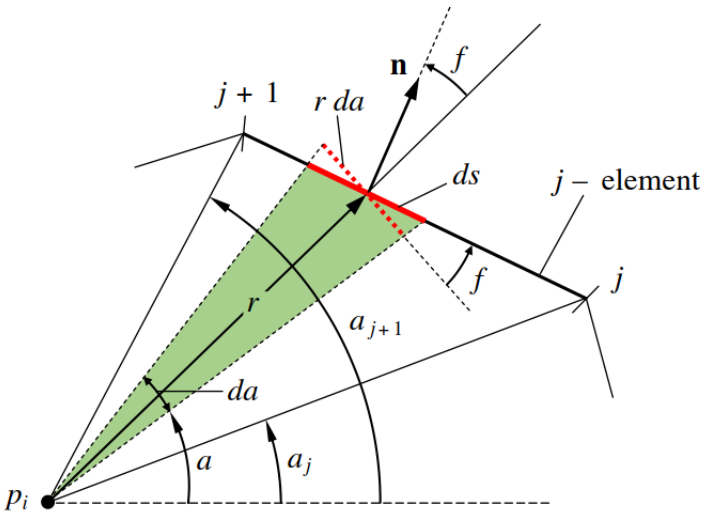

Figure 3.3: Definition of angles involved in the numerical integration over constant elements.

In this case node p_i coincides with node p_j, and $\mathbf{r}$ lies on the element. Consequently, it is $\phi = \pi/2$ or $\phi = 3\pi/2$, which yields to $\cos\phi = 0$ in both cases. Follow

$$x_{pj} = \frac{x_{j+1} + x_j}{2} \ ,$$
$$y_{pj} = \frac{y_{j+1} + y_j}{2} \ ,$$

and the distance r

$$r(\xi) = \sqrt{[x(\xi) - x_{pj}]^2 + [y(\xi) - y_{pj}]^2} = \frac{l_j}{2}|\xi| \ .$$

Hence the influence coefficient can be computed as

$$\begin{aligned} G_{jj} &= \int_{\Gamma_j} \frac{1}{2\pi} \ln r ds = 2 \int_0^{l_j/2} \frac{1}{2\pi} \ln r dr = \frac{1}{\pi} \left[r \ln r - r \right]_0^{l_j/2} \\ &= \frac{1}{\pi} \frac{l_j}{2} \left[\ln \left(\frac{l_j}{2} \right) - 1 \right] \ , \end{aligned} \tag{3.31}$$

$$\begin{aligned} \hat{H}_{jj} &= \frac{1}{2\pi} \int_{\Gamma_j} \frac{\cos\phi}{r} ds = \frac{1}{2\pi} \int_{-1}^{+1} \frac{\cos\phi}{|\xi|} d\xi = \frac{2}{2\pi} \left[\cos\phi \ln |\xi| \right]_0^1 \\ &= 0 \ . \end{aligned} \tag{3.32}$$

It has to be highlighted that, for higher order elements, analytical integration is not applicable for the case of Cauchy singularity and, for this reason, other integration techniques are employed.

Linear and Quadratic BEM The case of linear and quadratic BEM must be treated carefully, since over each single element more than one node is defined. Consequently, in these cases, the inside integration has to be differentiated in two sub-cases, i.e. when p and q are in the same element but $p \neq q$ or when p and q are in the same element and $p = q$ [8].

In the first case, the kernels are singular, i.e. they tend to infinity as point q is approached, but the shape function $\psi_\alpha(\xi)$ in the vicinity of p is of the order $r(p, q)$ and tends to zero. Therefore, the integrals of the product of the kernels and the shape function tend to a finite value instead of being singular and the evaluation can be carried out using the standard Gaussian quadrature.

In the second case the kernels still tend to infinity whereas the shape function tends to unity. This leads to an infinite, or singular, integral of the product .

- Cauchy singularity

  The matrices $[G]$ and $[H]$ are affected only by the boundary geometry, its discretization and the employed type of element. Hence, these matrices do not depend on the boundary conditions. The indirect evaluation of the diagonal influence coefficients H_{ii} for linear and quadratic BEM is based on this property. Considering a closed domain Ω, the diagonal element in the i-th row of matrix $[H]$ is equal to the negative sum of the remaining elements in this row

  $$H_{ii} = -\sum_{\substack{j=1 \\ j \neq i}}^{J} H_{ij} \ .$$

  Therefore, this method avoids the evaluation of any singular integral for the coefficients of matrix $[H]$.

- Logarithmic singularity for linear BEM

  This kind of singularity, for the linear BEM, can be threated analytically by solving the integrals by parts in the local coordinate system, yielding the following analytical expression for the influence coefficients

  $$G_{jj} = g_1^{jj} + g_2^{jj-1} \ ,$$

  and the two terms are calculated as [5]

  $$g_1^{jj} = \frac{l_j}{4\pi} \left[\ln(l_j) - 1.5\right] \ ,$$
  $$g_2^{jj-1} = \frac{l_j}{4\pi} \left[\ln(l_{j-1}) - 1.5\right] \ ,$$

  where

  $$l_j = \sqrt{(x_{j+1} - x_j)^2 + (y_{j+1} - y_j)^2} \ .$$

- Logarithmic singularity for quadratic BEM

  This kind of integrals, for quadratic BEM, can be computed thanks to the subtraction and series expansion method [9]: it deals with the singularity by subtracting it out, using a function that is found from an appropriate series expansion and which has the same singular properties. This yields to the sum

$$\int_{-1}^{+1} F(\xi)d\xi = \int_{-1}^{+1} F(\xi)^* + \int_{-1}^{+1} \{F(\xi) - F(\xi)^*\}d\xi \ , \tag{3.33}$$

  where $F(\xi)^*$ has a singularity of the same type as $F(\xi)$, so that the remainder $F(\xi) - F(\xi)^*$ is not singular and its integral can be evaluated using ordinary numerical quadrature methods such as Standard Gaussian quadrature.

  Concerning the construction of the function $F(\xi)^*$, a general procedure is provided by considering the series expansion of $F(\xi)$. As is known, only the integrands appearing in (3.33) with the form

$$\psi_\alpha(\xi) \ \ln|p(\xi) - p_\alpha| \ |J(\xi)| \ , \tag{3.34}$$

  need a special treatment. Each of the three terms of (3.34) can be expanded separately as a Taylor series about the point p_α, where $\alpha = 1, 2$ or 3.

  The latter procedure allows to identify and isolate the singular part of integrand $F(\xi)$, and thus $F(\xi)^*$ can be defined. At this point, the resulting integrals can be evaluated in a similar way to the linear elements case.

3.1.6 Solution at internal points of the domain

The solution of (3.2) yield the unknown boundary quantities u and $\partial_{\mathbf{n}}u$. Therefore, knowing all the boundary values on Γ, the solution u can be computed at any point $P(x, y)$ in the domain Ω still by virtue of (3.2) for $\epsilon(P) = 1$

$$u(P) = \sum_{j=1}^{J} H_{ij}u^j - \sum_{j=1}^{J} G_{ij}\partial_{\mathbf{n}}u^j \ , \tag{3.35}$$

where the influence coefficients are computed again from integrals, but in this case p_i is replaced in the expression by the internal point P, avoiding any singular integrals.

3.2 Galerkin method

For the Galerkin method [6], one can write (2.34) as

$$Au = f \quad \text{on } \Gamma \ , \tag{3.36}$$

where A is the boundary integral operator and f is the harmonic function, or its derivative, defined along the boundary Γ. We look for the approximated solution

$$u(x) = \sum_{j=1}^{J} \gamma_j \mu_j(x) \ , \tag{3.37}$$

with basis functions $\{\mu_j | j = 1, ..., J\}$ and unknown coefficients $\{\gamma_j | j = 1, ..., J\}$. Since u is an approximation of the real solution, substituting it in the initial equation (3.36) will result in an error

$$Au - f = e \ . \tag{3.38}$$

We assume the weighted average error of the approximation to be zero over Γ. Hence, results the system of equations

$$\sum_{j=1}^{J} (\mu_k, A\mu_j)\, \gamma_j = (\mu_k, f) \quad \text{for} \quad k = 1, ..., J \ , \tag{3.39}$$

where the brackets $(\cdot, \cdot)$ denote the $L^2(\Gamma)$ inner product

$$(f, g) = \int_\Gamma \overline{f(x)} g(x) do(x) \tag{3.40}$$

3.2.1 HILBERT library

The MATLAB® BEM library HILBERT [10] allows the numerical solution of the 2D Laplace equation, on some bounded domain with mixed boundary conditions, by means of the Galerkin Boundary Element Method.

3.2.2 Representation formula

Each solution of (2.16) can explicitly be written in the form

$$u(P) = \tilde{V}\phi(P) - \tilde{K}g(P) \ , \tag{3.41}$$

where $\phi = \partial u / \partial \mathbf{n}|_\Gamma$ and $g = u|_\Gamma$. The involved integral operators read

$$\tilde{V}\phi(P) = -\frac{1}{2\pi} \int_\Gamma \log|P - q| \phi(q) d\Gamma(q) \ , \tag{3.42}$$

$$\tilde{K}g(P) = -\frac{1}{2\pi} \int_\Gamma \frac{(q - P) \cdot \mathbf{n}_q}{|P - q|^2} g(q) d\Gamma(q) \ , \tag{3.43}$$

where $\mathbf{n}_q$ denotes the outer unit vector of Ω at some point $q \in \Gamma$, whereas $\mathbf{r} = P - q$ is the distance between the evaluation point P in Ω and the integration point q on Γ.

3.2.3 Boundary discretization

The closed boundary Γ is partitioned into a finite number of open and disjoint boundary pieces, e.g. in a Dirichlet boundary Γ_D and a Neumann boundary Γ_N, that is, $\Gamma = \Gamma_D \cup \Gamma_N$ and $\Gamma_D \cap \Gamma_N = \emptyset$. Let $\varepsilon_l = \{E_1, ..., E_J\}$ be a finite set of line segments $E_i \in \varepsilon_l$ and $\kappa_l = \{z_1, ..., z_J\}$ be the associated set of nodes of the mesh ε_l. Here, element E_i is identified by its extreme points z_j and z_k. Elements and nodes are numbered anticlockwise.

For mixed boundary value problems, missing Neumann data are approximated by an ε_l-piecewise constant function $\Phi_l \approx \phi$ and missing Dirichlet data are approximated by an ε_l-piecewise and continuous function $G_l \approx g$. Throughout, HILBERT uses the canonical bases, i.e., characteristic functions χ_j associated with elements $E_j \in \varepsilon_l$ to represent discrete fluxes Φ_l and nodal hat functions ζ_k associated with nodes $z_k \in \kappa_l$ to represent discrete traces G_l.

3.2.4 Dirichlet problem: Symm's integral equation

The Laplace problem with Dirichlet boundary condition is equivalently recast in Symm's integral equation [10]

$$V\phi = \left(K + \frac{1}{2}\right) g \ , \tag{3.44}$$

with g being the known Dirichlet data and ϕ being the unknown Neumann data.

To discretize (3.44) we first replace the continuous Dirichlet data g by its nodal interpolant

$$G_l = \sum_{j=1}^{J} g(z_j)\zeta_j \ . \tag{3.45}$$

Then, we define the unknown vector $\{x\} \in \mathbb{R}^J$ and the vector $\{g\} \in \mathbb{R}^J$ from

$$\Phi_l = \sum_{j=1}^{J} x_j \chi_j \quad \text{and} \quad G_l = \sum_{j=1}^{J} g_j \zeta_j \ . \tag{3.46}$$

The Galerkin formulation is thus equivalent to the linear system

$$(Vx)_k = \sum_{j=1}^{J} x_j V_{kj} = \sum_{j=1}^{J} g_j \left(K_{kj} + \frac{1}{2} M_{kj}\right) = \left(Kg + \frac{1}{2} Mg\right)_k \ , \tag{3.47}$$

that is solved for $\{x\}$, with $k = 1, ..., J$.

3.2.5 Computation of matrices [V], [K] and [M]

The matrices $[V], [K], [M] \in \mathbb{R}^{J\times J}$ defined in (3.47) are implemented in the programming language C via the MATLAB®-MEX-Interface.

The simple-layer potential matrix $[V]$ is returned by call of "buildV.m". Its entries read

$$V_{kj} = -\frac{1}{2\pi}\int_{E_k}\int_{Ej} \log|p-q| d\Gamma(q) d\Gamma(p) \ . \tag{3.48}$$

The double-layer potential matrix $[K]$ is returned by call of "buildK.m". Its entries read

$$K_{kj} = -\frac{1}{2\pi}\int_{E_k}\int_{supp(\zeta_j)} \frac{(q-p)\cdot \mathbf{n}_q}{|p-q|^2}\zeta_j(q) d\Gamma(q) d\Gamma(p) \ . \tag{3.49}$$

The mass matrix $[M]$ is returned by call of "buildM.m". Its entries read

$$M_{kj} = \begin{cases} 0 & \text{if } z_j \notin \{z_m, z_n\} \ , \\ \text{length}(E_k)/2 & \text{if } z_j \in \{z_m, z_n\} \ , \end{cases} \tag{3.50}$$

where $E_k = [z_m, z_n] \in \varepsilon_l$.

3.2.6 Neumann problem: hypersingular integral equation

The Laplace problem with Neumann boundary condition is equivalently recast in the hypersingular integral equation [10]

$$Wg = \left(\frac{1}{2} - K'\right)\phi \tag{3.51}$$

with g being the unknown Dirichlet data and ϕ being the known Neumann data.

To discretize (3.51) we first replace the Neumann data ϕ by its L^2-projection

$$\Phi_l|_{E_j} = \frac{1}{\text{length}(E_j)}\int_{E_j} \phi d\Gamma = p_j \ , \tag{3.52}$$

such that it holds

$$\int_\Gamma \Phi_l d\Gamma = \sum_{E\in\varepsilon_l}\int_E \Phi_l d\Gamma = 0 \ . \tag{3.53}$$

and the Gauss Divergence Theorem is satisfied.

Then, we define the unknown vector $\{x\} \in \mathbb{R}^J$ and the vector $\{p\} \in \mathbb{R}^J$ from

$$G_l = \sum_{j=1}^{J} x_j \zeta_j \quad \text{and} \quad \Phi_l = \sum_{j=1}^{J} p_j \chi_j \ . \tag{3.54}$$

The Galerkin formulation is thus equivalent to the linear system

$$\begin{aligned}\left((W+S)\,x\right)_k &= \sum_{j=1}^{J} x_j \left(W_{kj}+S_{kj}\right) = \sum_{j=1}^{J} p_j \left(\frac{1}{2}M_{jk}-K_{jk}\right) \\ &= \left(\frac{1}{2}M^T p - K^T p\right)_k \ ,\end{aligned} \tag{3.55}$$

that is solved for $\{x\}$, with $k = 1, ..., N$.

3.2.7 Computation of matrices [W] and [S]

The matrices $[W], [S] \in \mathbb{R}^{J\times J}$ defined in (3.55) are implemented in the programming language C via the MATLAB®-MEX-Interface.

The hypersingular integral operator $[W]$ is returned by call of "buildW.m". Its entries are computed with the help of Nedelec's formula [10], which gives a direct link between the matrices $[W]$ and $[V]$, namely, each entry of $[W]$ is the weighted sum of four entries of $[V]$.

The stabilization term matrix $[S]$ is returned by call of "buildHypsingStabilization.m". It is assembled as $[S] = \{c\}\{c\}^T$, with

$$c_k = \int_\Gamma \zeta_k d\Gamma = \sum_{i=1}^{J} \int_{E_i} \zeta_k d\Gamma \ , \tag{3.56}$$

where

$$\int_{E_i} \zeta_k d\Gamma = \begin{cases} 0 & \text{if } z_k \notin E_i \ , \\ \text{length}(E_i)/2 & \text{else .} \end{cases} \tag{3.57}$$

3.2.8 Mixed problem

We consider the mixed boundary value problem

$$\begin{aligned} \nabla^2 u &= 0 \quad \text{in } \Omega \ , \\ u &= u_D \ \text{ on } \Gamma_D \ , \\ \frac{\partial u}{\partial \mathbf{n}} &= \phi_N \ \text{ on } \Gamma_N \ . \end{aligned} \tag{3.58}$$

The missing boundary data are the values of the unknown boundary conditions u_N and ϕ_D on the boundary portions Γ_N and Γ_D, respectively

$$u_N = u - u_D \quad \text{and} \quad \phi_D = \frac{\partial u}{\partial \mathbf{n}} - \phi_N \ . \tag{3.59}$$

The Galerkin discretization is performed for the two separate problems on Γ_D and Γ_N. We replace the continuous Dirichlet data by its nodal interpolant and the

Neumann data by its L^2-projection

$$U_{D,l} = \sum_{i=1}^{J} g_i \zeta_i \quad \text{and} \quad \Phi_{N,l} = \sum_{i=1}^{J} p_i \chi_i \ , \tag{3.60}$$

where the representation for $\Phi_{N,l}$ shrinks to a sum over all elements on Γ_N, whereas $U_{D,l}$ takes into account all nodes in order to satisfy the continuity of the problem.

The unknowns are defined as

$$U_{N,l} = \sum_{i=1}^{n} x_i \zeta_i \quad \text{and} \quad \Phi_{D,l} = \sum_{i=1}^{d} x_{n+i} \chi_i \ . \tag{3.61}$$

where n and d are the dimensions of the Neumann and Dirichlet boundary problem, respectively.

We write the linear system of equations as

$$[A]\{x\} = \{b\} \ , \tag{3.62}$$

where $[A] \in \mathbb{R}^{(n+d)\times(n+d)}$ and $\{b\} \in \mathbb{R}^{n+d}$ are computed accordingly to the data representation (3.60). Introducing $j = 1, ..., n$ and $k = 1, ..., d$, the right-hand side vector $\{b\}$ is assembled as

$$b_j = \left(\frac{1}{2} M^T p - K^T p - W^T g \right)_j \ ,$$
$$b_{n+k} = \left(\frac{1}{2} M g + K g - V p \right)_k \ ,$$

such that, results

$$\{b\} = \begin{pmatrix} \left(\frac{1}{2} p^T M - p^T K - g^T W \right)^T |_{\Gamma_N} \\ \left(\frac{1}{2} M g + K g - V p \right) |_{\Gamma_D} \end{pmatrix} \ . \tag{3.63}$$

Consequently, the Galerkin matrix $[A]$ is written as a combination of operators

$$[A] = \begin{bmatrix} [W]\,|_{\Gamma_N \times \Gamma_N} & [K]^T\,|_{\Gamma_N \times \Gamma_D} \\ [-K]\,|_{\Gamma_D \times \Gamma_N} & [V]\,|_{\Gamma_D \times \Gamma_D} \end{bmatrix} \ . \tag{3.64}$$

Finally, (3.62) is solved for $\{x\}$.

3.2.9 Solution at internal points of the domain

Once the vector of the unknowns $\{x\}$ is retrieved, one can compute the solution u at any internal point P of Ω. Evaluation of the simple-layer potential $\tilde{V}$ and the double-layer potential $\tilde{K}$ in (3.41) at arbitrary evaluation points in $\mathbb{R}^2$ is provided, as soon as g and ϕ are computed at any point q of Γ, by the MEX-functions "evaluateV.m" and "evaluateK.m".

3.3 Maximum error

The solution u in (3.35) and (3.41) is only an approximation of the real solution u' in $\overline{\Omega} = \Omega \cup \Gamma$. Since both of them are harmonic functions which satisfy the Laplace equation everywhere on Ω, consequently even the absolute error $e = |u - u'|$ is an harmonic function with the same properties in Ω. The maximum principle (2.17)

$$\max_{\overline{\Omega}} e(x, y) = \max_{\Gamma} e(x, y) \ , \tag{3.65}$$

states that the maximum error introduced when we approximate u' with u lies on the boundary Γ.

Chapter 4

Validation of the Numerical Implementation of Collocation BEM

In this chapter, the BEM is applied to the 2D case study of a infinite straight wire. This is useful to validate the MATLAB® BEM code, to identify and evaluate the features of the MVP and MSP formulation, and even to compare the linear and quadratic elements results. A boundary value problem defined over a rectangle is considered.

4.1 The Biot-Savart law

The Biot-Savart law is used for computing the magnetic flux density $\mathbf{B}$ generated by a steady state current I at a position identified by $\mathbf{r}$ in 3D space. The problem is fixed in a cylindrical coordinate system, where the current is pointing in the direction of the wire element $d\mathbf{l}$.

The differential form of the equation is expressed as

$$d\mathbf{B}(r) = \frac{\mu_0}{4\pi} I \frac{d\mathbf{l} \times \mathbf{r}}{|\mathbf{r}|^3} \ , \tag{4.1}$$

and is then integrated over the wire path C

$$\mathbf{B}(r) = \frac{\mu_0}{4\pi} \int_C \frac{I d\mathbf{l} \times \mathbf{r}}{|\mathbf{r}|^3} \ . \tag{4.2}$$

For the infinite straight wire case, the problem reduces to a 2D case since the field does not depend on the z coordinate, due to the symmetry of the problem. Results

$$\mathbf{B}(r) = \frac{\mu_0 I}{2\pi} \frac{\mathbf{l} \times \mathbf{r}}{|\mathbf{r}|} = \frac{\mu_0 I}{2\pi r} \boldsymbol{\alpha} \ , \tag{4.3}$$

where I is the intensity of the current flowing into the wire, r is the absolute value of the distance between the wire and the point at which $\mathbf{B}$ is computed, and finally $\boldsymbol{\alpha}$ is the direction of the field resulting from the cross product $d\mathbf{l} \times \mathbf{r}$.

At this point, starting from the analytical expression of the magnetic flux density in (4.3), it is possible to derive the expressions of the magnetic potential:

- Magnetic Vector Potential

  Given the relation (C.10) and knowing the expression of the curl in cylindrical coordinates

$$\begin{aligned}\frac{\mu_0 I}{2\pi r}\boldsymbol{\alpha} = &\left(\frac{1}{r}\frac{\partial A_z}{\partial \alpha} - \frac{\partial A_\alpha}{\partial z}\right)\mathbf{r} + \left(\frac{\partial A_r}{\partial z} - \frac{\partial A_z}{\partial r}\right)\boldsymbol{\alpha} \\ &+ \frac{1}{r}\left(\frac{\partial\left(rA_\alpha\right)}{\partial r} - \frac{\partial A_r}{\partial \alpha}\right)\mathbf{z}\ ,\end{aligned} \tag{4.4}$$

  leads to

$$A_z = -\frac{\mu_0 I}{2\pi}\ln r + d\ , \tag{4.5}$$

  where d is the integration constant and has to be set in order to get the appropriate reference value.

- Magnetic Scalar Potential

  Given the relation (C.2) and knowing the expression of the gradient in cylindrical coordinates

$$\frac{\mu_0 I}{2\pi r}\boldsymbol{\alpha} = \frac{\partial \phi_m}{\partial r}\mathbf{r} + \frac{1}{r}\frac{\partial \phi_m}{\partial \alpha}\boldsymbol{\alpha} + \frac{\partial \phi_m}{\partial z}\mathbf{z}\ , \tag{4.6}$$

  leads to

$$\phi_m = \frac{\mu_0 I}{2\pi}\alpha + c\ , \tag{4.7}$$

  where the angle α is defined in the interval $[0, 2\pi)$ and the integration constant c establishes the reference for the computation of the potential.

4.2 The test problem

For the case study, a current I of 1000 A, with direction pointing out of the plane, is considered as the source of a magnetic flux density $\mathbf{B}$. Once the geometry of the boundary is established, one can compute analytically, using (4.5) and (4.7), the values of the vector and scalar potential at the nodes of the boundary value problem, in order to be able to use them as boundary conditions for the BEM implementation.

The geometry of the problem is represented in Fig. 4.1: the left side of the rectangular boundary $\{-200 \text{ mm} \leq x \leq +200 \text{ mm},\ -30 \text{ mm} \leq y \leq +30 \text{ mm}\}$ is placed at 100 mm from the source.

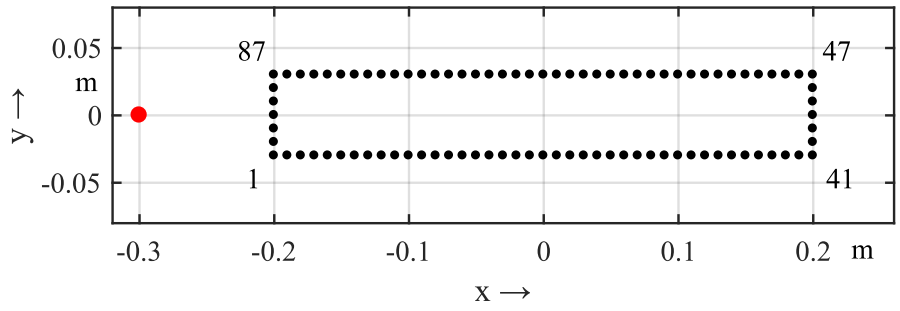

Figure 4.1: Geometry of the boundary value problem. K nodes are numbered anticlockwise, as shown for the corner points.

Fig. 4.2 shows the equipotential lines of the vector and scalar potentials in the xy-plane. As can be noticed, the equipotentials of the MVP are the streamlines of the vector field **B** , or better, the magnetic flux lines. The equipotentials of the MSP are those lines that cross perpendicularly the field streamlines.

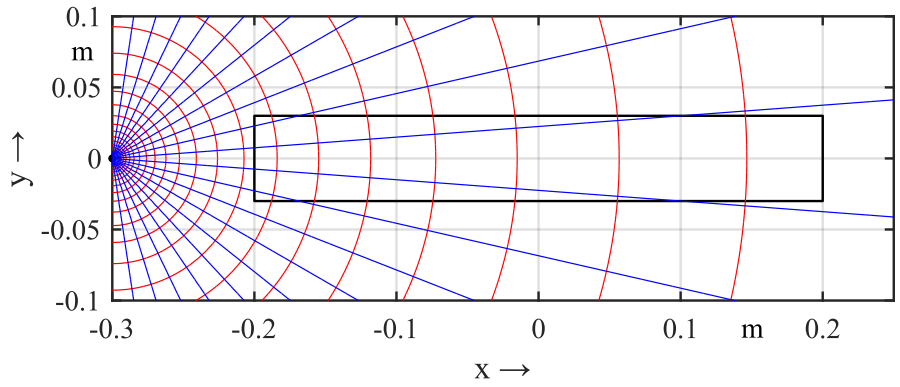

Figure 4.2: Equipotential lines in the two dimensional plane.

4.2.1 Dirichlet boundary conditions

The MVP and MSP values are computed at $K = 92$ equidistant points over the rectangular boundary, progressing in counter-clockwise sense starting from the corner $(-200\text{ mm}, -30\text{ mm})$ (see Fig. 4.1).

Fig. 4.3 and Fig. 4.4 show the trend of the two quantities over the rectangular boundary. The scalar potential ϕ_m is not a single-valued function of position. Looking at (4.7) with $c = 0$, we notice that only if any current I is enclosed by the computed path, then a single-potential function can be defined. In this case, the reference, or better the integration constant c of (4.7), is fixed such that the scalar

potential ϕ_m equals zero at the first corner of the boundary. Contrarily, for the magnetic potential A_z, the integration constant d of (4.5) is the value that has been set to zero.

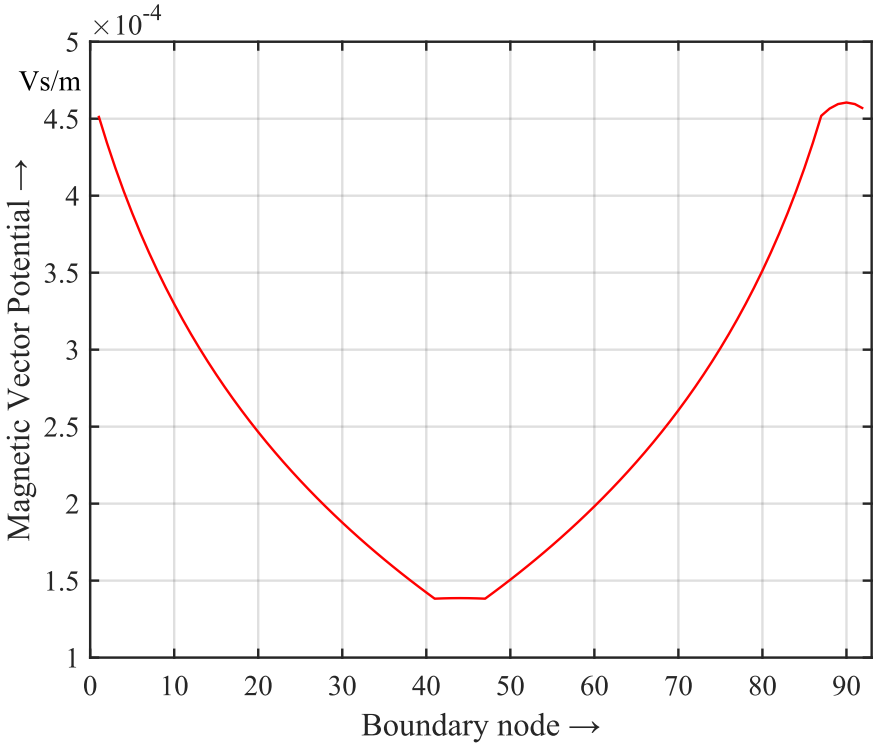

Figure 4.3: MVP trend along the boundary.

4.3 Dirichlet to Neumann map

As a first step, the BEM computes, at the nodes of the boundary, the unknown Neumann boundary conditions from the Dirichlet ones (Dirichlet to Neumann map). We know from Appendix C that the relations between the derivatives of the potentials and the field $\mathbf{B}$ in a two-dimensional space are

$$\mathbf{B} = \mathbf{i}\,\frac{\partial A_z}{\partial y} - \mathbf{j}\,\frac{\partial A_z}{\partial x}\,, \tag{4.8}$$

$$\mathbf{B} = \mathbf{i}\,\frac{\partial \phi_m}{\partial x} + \mathbf{j}\,\frac{\partial \phi_m}{\partial y}\,, \tag{4.9}$$

in particular we refer to normal and tangential derivatives with respect to the boundary. Clearly, for a rectangular boundary, one can easily relate the x and y Cartesian components of the field with the normal and tangential ones over each of the four

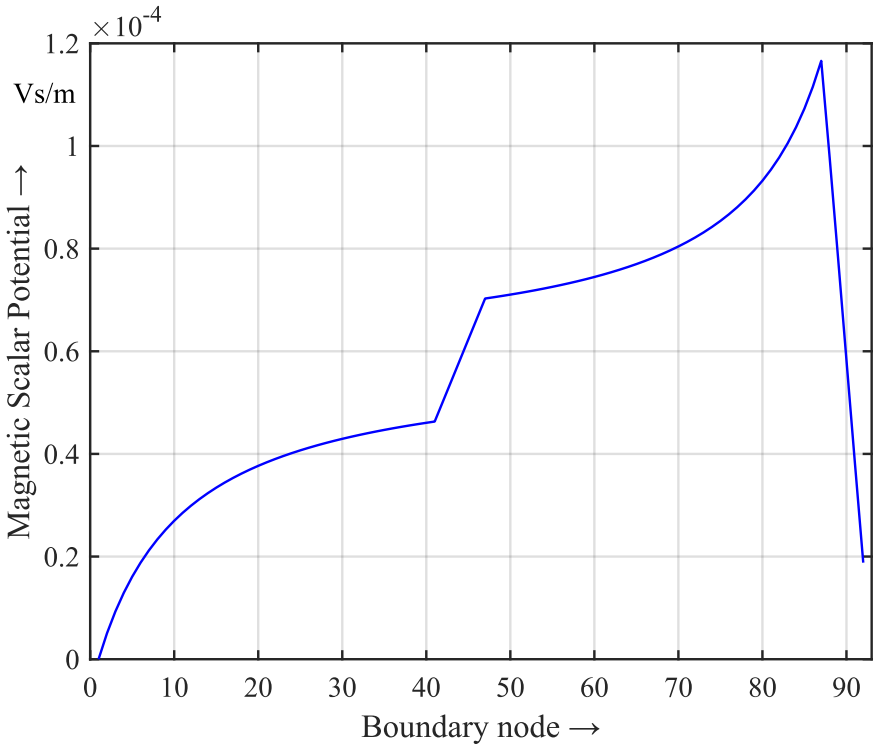

Figure 4.4: MSP trend along the boundary.

sides

$$B_t^{(1)} = +B_x^{(1)} = +\frac{\partial A_z}{\partial y}^{(1)} = -\frac{\partial A_z}{\partial \mathbf{n}}^{(1)} , \quad B_n^{(1)} = -B_y^{(1)} = -\frac{\partial \phi_m}{\partial y}^{(1)} = +\frac{\partial \phi_m}{\partial \mathbf{n}}^{(1)} ,$$
$$B_t^{(2)} = +B_y^{(2)} = -\frac{\partial A_z}{\partial x}^{(2)} = -\frac{\partial A_z}{\partial \mathbf{n}}^{(2)} , \quad B_n^{(2)} = +B_x^{(2)} = +\frac{\partial \phi_m}{\partial x}^{(2)} = +\frac{\partial \phi_m}{\partial \mathbf{n}}^{(2)} ,$$
$$B_t^{(3)} = -B_x^{(3)} = -\frac{\partial A_z}{\partial y}^{(3)} = -\frac{\partial A_z}{\partial \mathbf{n}}^{(3)} , \quad B_n^{(3)} = +B_y^{(3)} = +\frac{\partial \phi_m}{\partial y}^{(3)} = +\frac{\partial \phi_m}{\partial \mathbf{n}}^{(3)} ,$$
$$B_t^{(4)} = -B_y^{(4)} = +\frac{\partial A_z}{\partial x}^{(4)} = -\frac{\partial A_z}{\partial \mathbf{n}}^{(4)} , \quad B_n^{(4)} = -B_x^{(4)} = -\frac{\partial \phi_m}{\partial x}^{(4)} = +\frac{\partial \phi_m}{\partial \mathbf{n}}^{(4)} .$$

Sides are numbered anti-clockwise starting from the lower one. Finally, it results that over the whole boundary holds

$$B_t = -\frac{\partial A_z}{\partial \mathbf{n}} , \quad B_n = +\frac{\partial \phi_m}{\partial \mathbf{n}} , \tag{4.10}$$

from which is possible to deduce that the Neumann boundary conditions for the MVP and MSP formulations are reconstructions of the field tangential and normal components, respectively, at the nodes of the boundary. In order to prove that, a comparison is carried out in Fig. 4.5 - 4.6 between the values obtained from the

BEM, for both the formulations, and the field components computed by Biot-Savart at the same points.

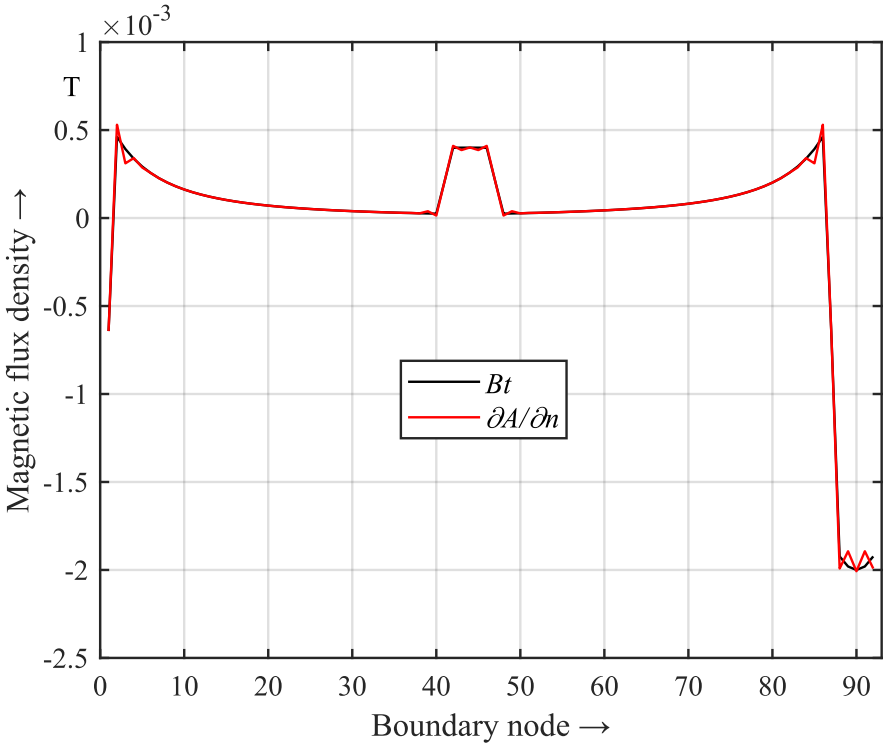

Figure 4.5: Comparison of the tangential field component computed and reconstructed by quadratic BEM at the nodes of the boundary.

As can be seen in Fig. 4.7 and Fig. 4.8 an higher error occurs on the right side of the contour and, from the comparison, the error is significantly bigger for the tangential component. This is due to the high variation of the field in this part of the boundary, as shown in Fig. 4.5 - 4.6. Furthermore, it can be noticed that the error at the corners, i.e. at the nodes number 1, 41, 47 and 87, is smaller. This is due to the fact that a tangential ,or normal, component can't be defined in these points, and for this reason the value is computed as the average between the components of the interested sides. This procedure is similar to the one carried out by BEM, and consequently the reconstructed and computed values tend to be close to each other.

A further proof of the correctness of the results can be derived from the computation of the Gauss' and Ampere's law over the closed boundary. Obviously, a discretized form is employed in this case, since the field is known at a finite number

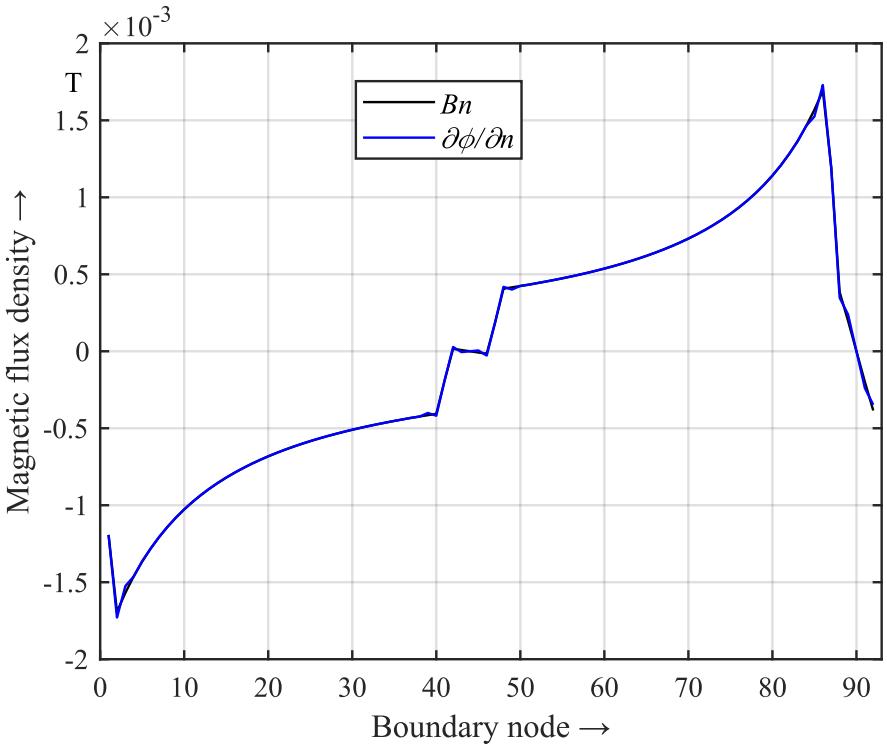

Figure 4.6: Comparison of the normal field component computed and reconstructed by quadratic BEM at the nodes of the boundary.

K of points, i.e. at the nodes of the boundary

$$\sum_{k=1}^{K} B_n^{(k)} \cdot S^{(k)} = 0 \ , \tag{4.11}$$

$$\sum_{k=1}^{K} \frac{B_t^{(k)}}{\mu_0} \cdot l^{(k)} = I_e \ , \tag{4.12}$$

where the current I_e enclosed in the domain should be zero since the field source, that is the filamentary current, is placed outside the bounded domain. Note that, since the nodes are placed at equidistant points, the length $l^{(k)}$ and consequently the unitary surface $S^{(k)} = l^{(k)} \cdot 1$ are equal for all the k-th points. The results are computed numerically as relative values

$$\frac{\sum_{k=1}^{K} B_n^{(k)} \cdot S^{(k)}}{B_n^{ref} \cdot S} = 1.5719e - 13 \ , \tag{4.13}$$

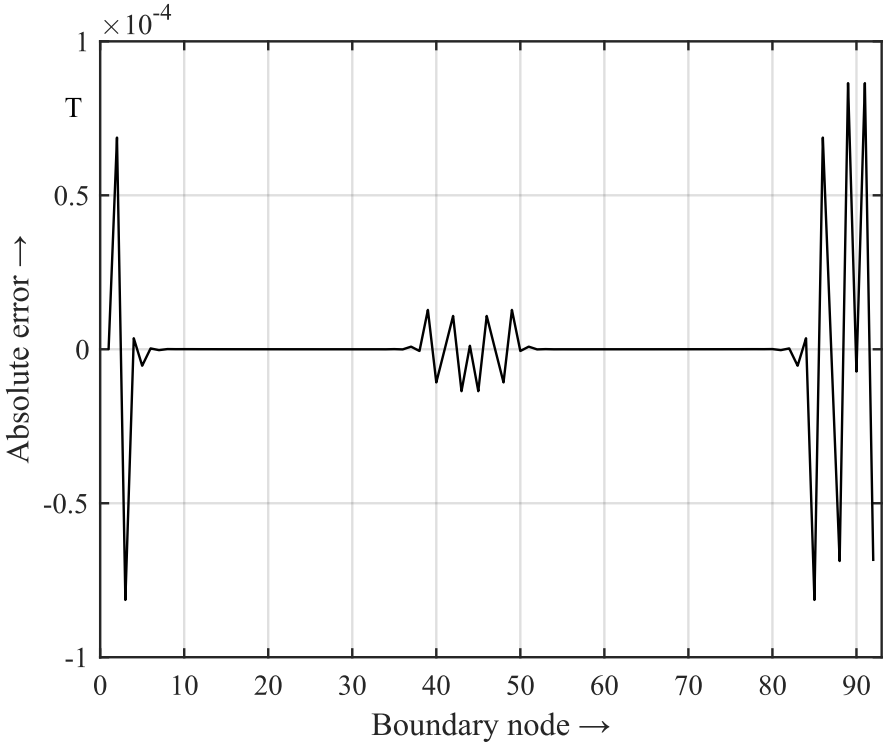

Figure 4.7: Absolute error associated to Fig. 4.5.

$$\frac{\sum_{k=1}^{K} \frac{B_t^{(k)}}{\mu_0} \cdot l^{(k)}}{\frac{B_t^{ref}}{\mu_0} \cdot l} = 0.0714 \ , \tag{4.14}$$

where the reference values B_n^{ref} and B_t^{ref} are the maximum values of the normal and tangential field components computed by Biot-Savart over the boundary. The results prove that an bigger error arises when the Ampere's law is computed. This can be explained looking at the approximations made in (4.11) and (4.12), since the field, computed point-wise, in these discretized forms is assumed to be constant over the element length l. This assumption works well with the normal component, because the error in this case is balanced by the horizontal sides variation, whereas the same is not true for the tangential component, which is highly varying quadratically on the right side only.

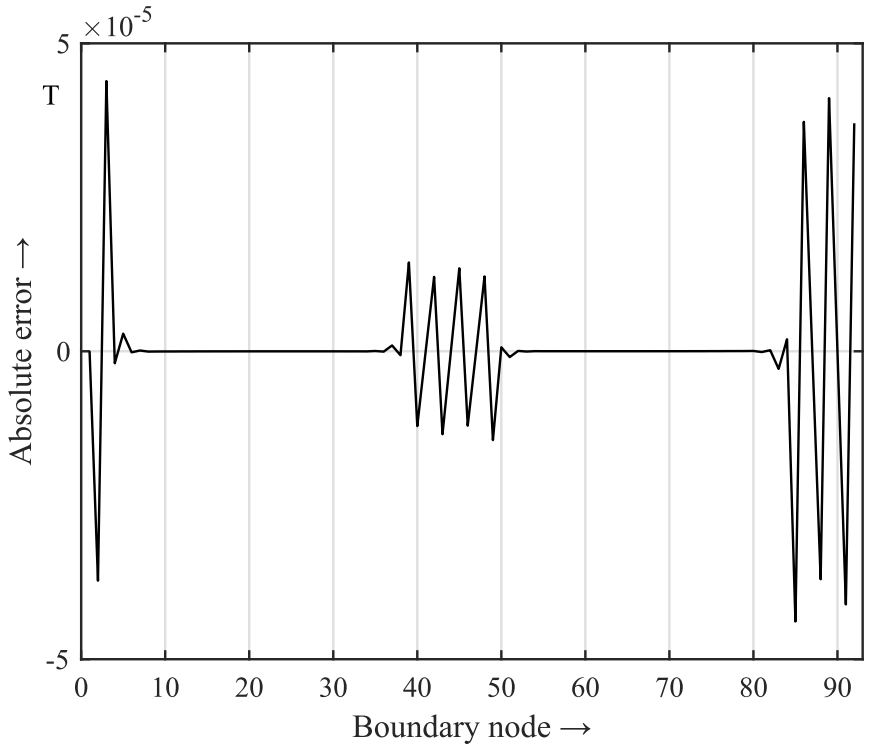

Figure 4.8: Absolute error associated to Fig. 4.6.

4.4 Solution at internal points of the domain

Since the main goal is to find the solution of the Laplace equation inside the bounded domain, the reference values of the MVP and of the MSP are computed with the Biot-Savart law over the mid-line $\{-180 \text{ mm} \leq x \leq +180 \text{ mm}, y = 0\}$. Fig. 4.9 - 4.10 show the trend of the MVP and MSP, respectively, over the mid-line. It is worth noting that, according to (4.5) and (4.7), the vector potential trend behaves as $-\ln r$, while the scalar potential remains constant for computations on $y = 0$ (α is constant).

At this point, the errors arising in BEM reconstruction can be evaluated comparing the Biot-Savart values to the ones computed by BEM at the same points of the domain. However, this evaluation does not allow to compare directly the two formulations. For this reason, it is necessary to refer to the magnetic flux density reconstruction. Fig. 4.7 show the trend of the magnetic flux density computed with the Biot-Savart law over the mid-line.

Since the source current I is placed at point $(-300 \text{ mm}, 0)$, that is, on the X axis, the field is entirely directed towards the y-direction. The y component of the

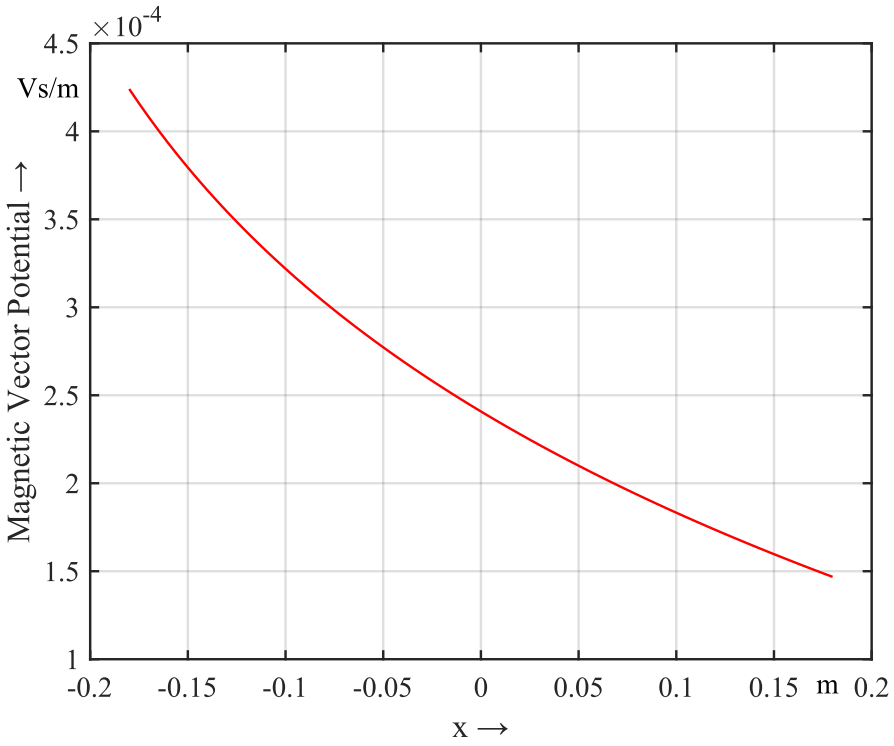

Figure 4.9: MVP trend over the mid-line y=0.

field **B** can be computed by differentiation as

$$B_y = -\frac{\partial A_z}{\partial x} \ , \quad B_y = +\frac{\partial \phi_m}{\partial y} \ . \tag{4.15}$$

Fig. 4.12 and Fig. 4.13 show the relative error ε_R arising in the magnetic flux density reconstruction over the line y=0, defined as

$$\varepsilon_R = 100 \left| \frac{B_y - B'_y}{B'_y} \right| \ , \tag{4.16}$$

where B_y is the field computed by differentiation (4.15) starting from the reconstructed potential, while B'_y is the one directly computed by the Biot-Savart law (4.3). The comparison is carried out between the MVP and MSP formulation using both the linear and quadratic elements. The following considerations can be noticed as a conclusion

- Field variation
  As can be seen both in Fig. 4.12 and Fig. 4.13, the error is not symmetric over the mid-line. These results derive from the fact that the field, as expressed in (4.3), is not varying linearly but like $1/r$. This means that an high variation

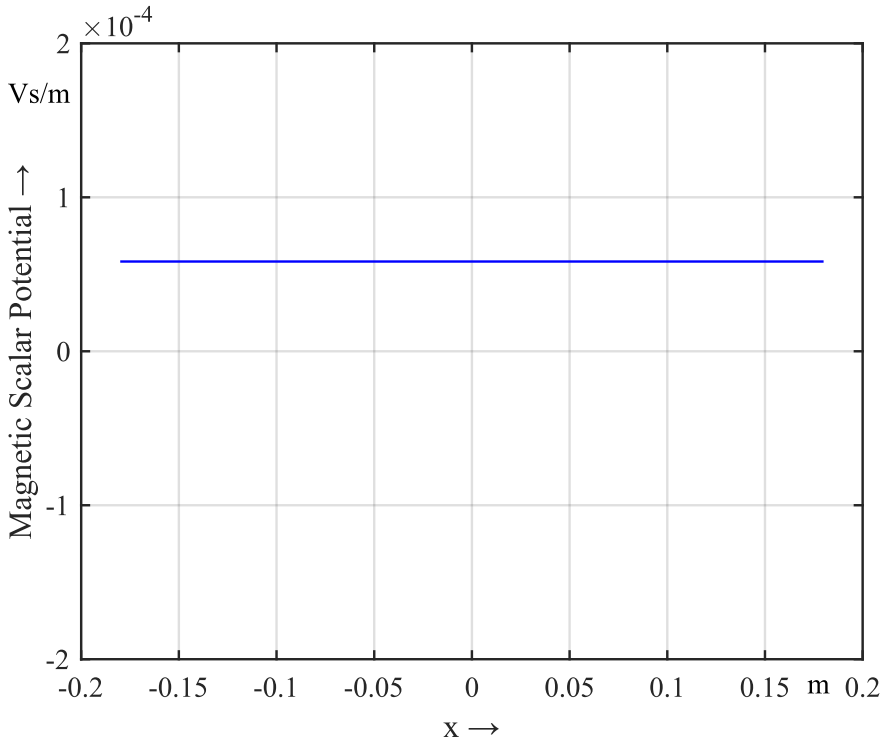

Figure 4.10: MSP trend over the mid-line y=0.

of the field occurs on the left side, whereas it decreases towards the right side. This behavior is verified even in the different variation of the potentials along the two vertical sides: along the left side the functions change much more than on the right one, as Fig. 4.9 - 4.10 show.

- Linear and quadratic elements
  The relative error defined in (4.16) is computed both for linear and quadratic elements, allowing the comparison between the two methods. As can be seen comparing Fig. 4.12 - 4.13, the error computed with the quadratic elements results the smaller one. This is mainly due to the fact that this method is able to approximate better the quadratic behavior of the potentials over the boundary

- MVP and MSP
  The reason of the different behavior of the error for the MVP and MSP formulations in the linear BEM results, shown in Fig. 4.12, has to be found in the trend of the potentials over the boundary. As Fig. 4.10 displays, the MSP is varying linearly over the vertical sides, allowing the linear BEM to approximate the function with an high precision. The latter is not true for the remaining

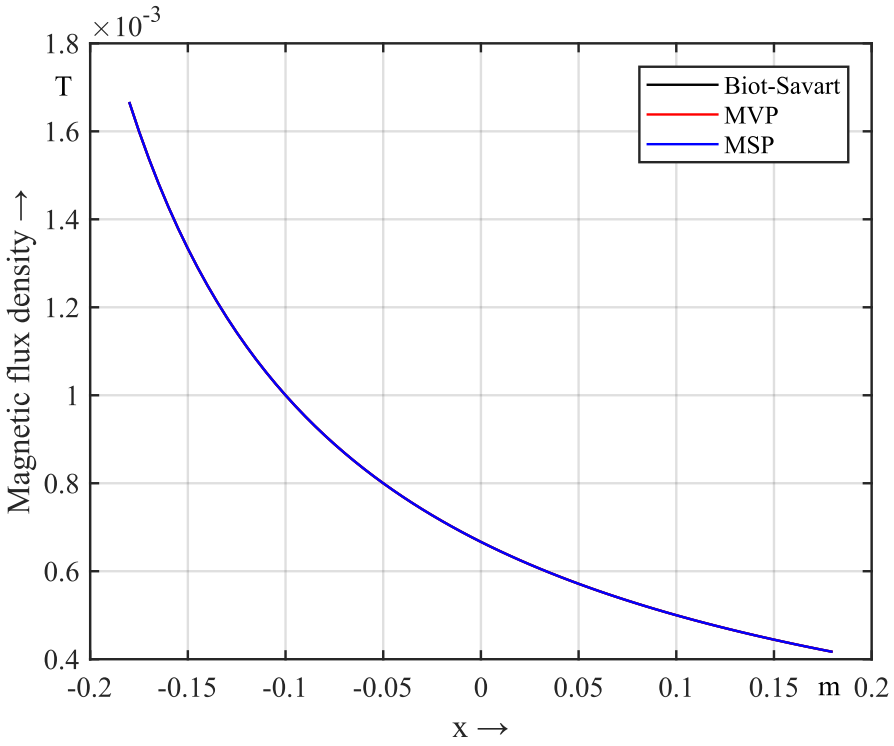

Figure 4.11: Magnetic flux density trend over the mid-line y=0.

horizontal sides and for the MVP, for which the quadratic function is not well approximated. This is why the error associated to the MSP reconstruction is overall slightly smaller.

Concerning Fig. 4.13, similar considerations can be done. The quadratic BEM is able to replace in a good way the variation of the potentials over the whole boundary. However, as it is shown, the error of the MSP reconstruction at the edges is lower. This arises from the fact that the linear variation of the MSP over the vertical sides is easier to approach then the quadratic one.

- BEM solution
  The variation of the error at the edge of the mid-line is due to the proximity to the sides of the boundary. In fact, is known that the BEM computation is highly affected when the distance between the boundary nodes and the inner points is close to zero.

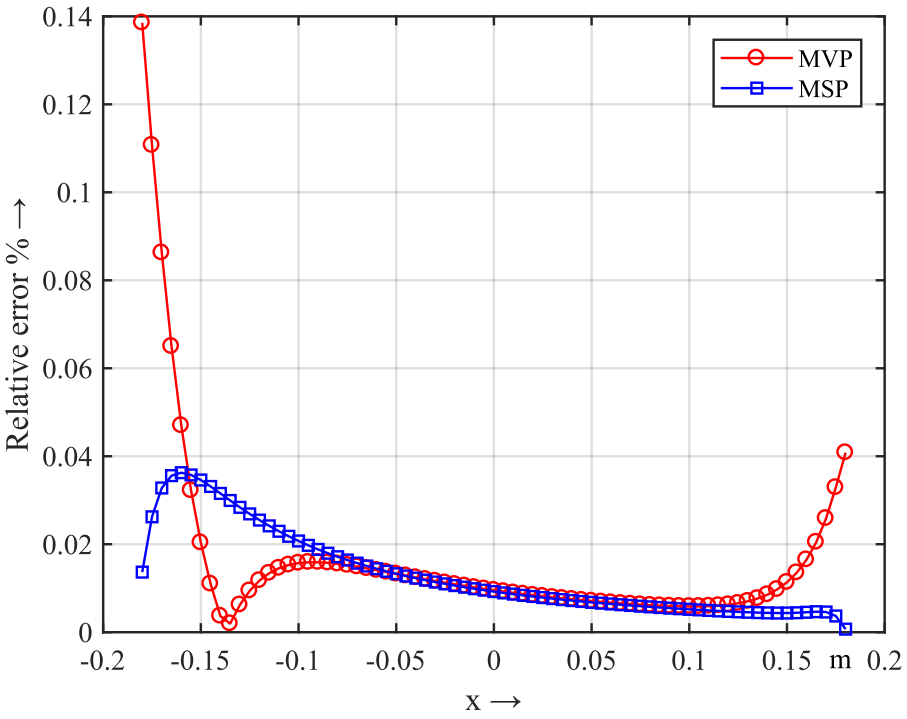

Figure 4.12: Relative error over y=0 (Linear elements).

4.5 Convergence analysis

In this section, a convergence analysis is carried out in order to investigate the behavior of the errors appearing in BEM reconstruction when the length of the boundary elements decreases, that is, when the number of nodes increases. Starting from the standard case of $K = 92$, the number of nodes is doubled at each step, such that other three cases, i.e. $K = 184, 368$ and 736, can be evaluated.

4.5.1 Field reconstruction along the boundary

The analysis is developed for the error in the reconstruction of tangential and normal field components, i.e. the computation of Neumann boundary conditions from the Dirichlet ones. The error norm is defined as

$$\|\varepsilon\|_{L^2} = \sqrt{\frac{\sum_{k=1}^{K} |B^{(k)} - B'^{(k)}|^2}{K}} \,, \tag{4.17}$$

where $B^{(k)}$ is the field component reconstructed by BEM, that is the retrieved Neumann boundary condition, while $B'^{(k)}$ is the field component computed by the Biot-Savart law, at node k. The sum is extended to all the nodes of the boundary and,

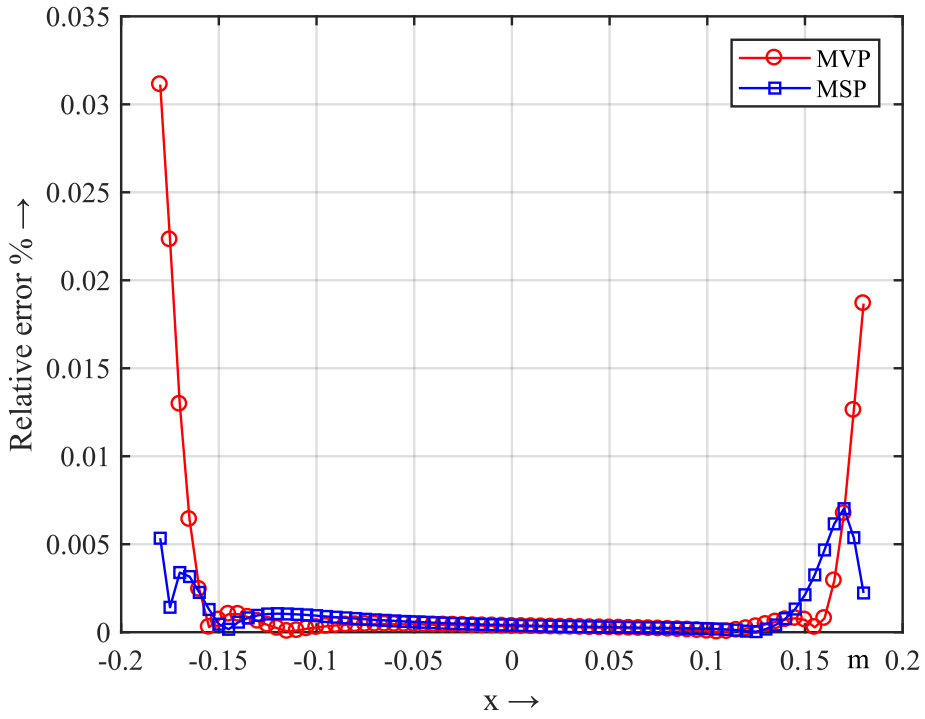

Figure 4.13: Relative error over y=0 (Quadratic elements).

clearly, it is divided by the number of nodes K in order to correctly compare the values. Result are shown in Fig. 4.14. According to previous results, the error is smaller for the computation of normal field components. The reason why the quadratic elements works better than the linear ones has to be investigated in Fig. 4.5 - 4.6, where the trend of the tangential and normal field components over the boundary is plotted.

4.5.2 Field reconstruction at internal points of the domain

The analysis is developed for the error in the reconstruction of the magnetic flux density **B**, calculated from its Cartesian components as

$$|\mathbf{B}| = \sqrt{B_x^2 + B_y^2}\,, \tag{4.18}$$

where B_x and B_y are computed from the derivatives of the BEM solution. In this way, we can correctly compare the results. The error is computed at $J = 121$ points inside the domain $\{-25\text{ mm} \leq x \leq +25\text{ mm}, -25\text{ mm} \leq y \leq +25\text{ mm}\}$ as

$$||\varepsilon||_{L^2} = \sqrt{\sum_{j=1}^{J} \left| \frac{B^{(j)} - B'^{(j)}}{B'^{(j)}} \right|^2}\,, \tag{4.19}$$

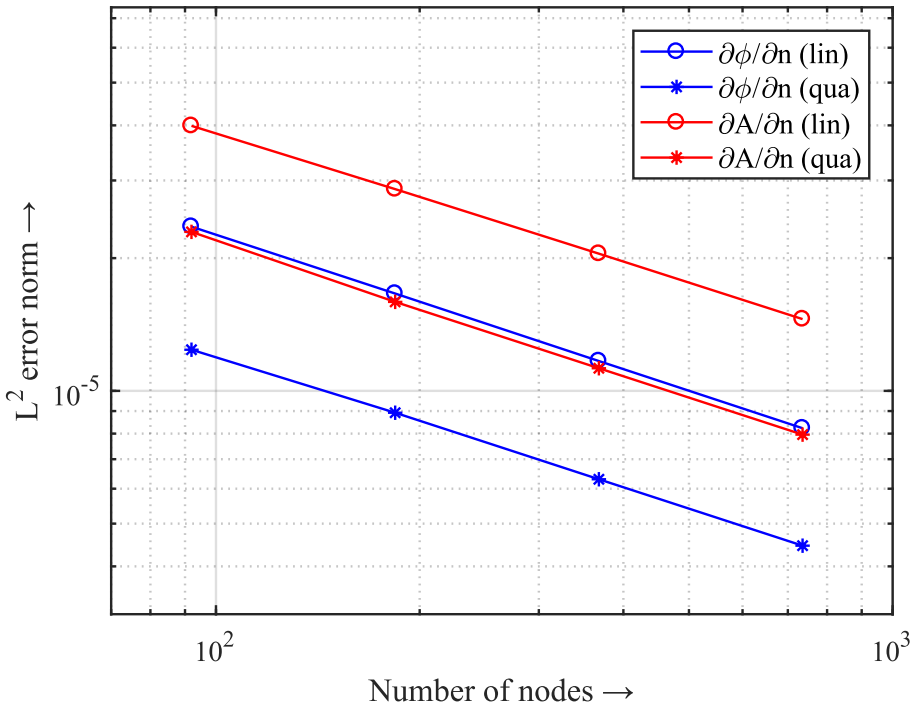

Figure 4.14: Convergence analysis for the error norm related to the BEM reconstruction of normal and tangential components over the boundary. The evaluation is performed for the MSP and MVP formulation, both with linear and quadratic elements.

where $B^{(j)}$ is the magnetic flux density derived from the BEM solution and $B'^{(j)}$ is the value computed by the Biot-Savart law, both at the j-th point of the grid.

4.6 Neumann boundary conditions

Until now, the boundary value problem has been solved starting from Dirichlet boundary conditions, that are A_z for the MVP formulation and ϕ_m for the MSP formulation. However, it is worth noting that, known the relations of (4.10), the problem can be solved even starting from Neumann boundary conditions, i.e. starting from the tangential, or normal, component of the field computed with the Biot-Savart law at the $K = 92$ nodes of the boundary. Clearly, since the Neumann boundary conditions refer to the normal derivatives of the potential, the solution is not unique, and for this reason at least one nodes has to be defined with a Dirichlet boundary condition. For the following case, the first node is chosen, which means that at the left-down corner of the rectangle we compute the potential instead of its normal derivative. The field is reconstructed by BEM over the line

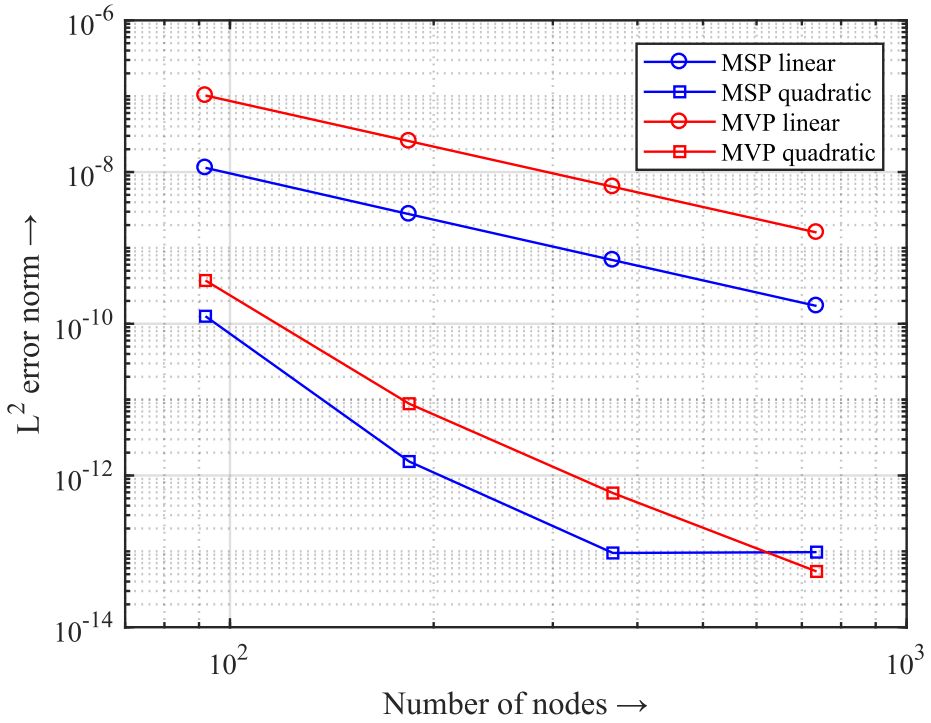

Figure 4.15: Convergence analysis for the error norm related to the BEM reconstruction of the field $\mathbf{B}$ at J points of the domain $\{-25 \text{ mm} \leq x \leq +25 \text{ mm}, -25 \text{ mm} \leq y \leq +25 \text{ mm}\}$.

$\{-180 \text{ mm} \leq x \leq +180 \text{ mm}, y = 0\}$ and subsequently compared with the field computed with Biot-Savart at the same points. Results are shown in Fig. 4.16.

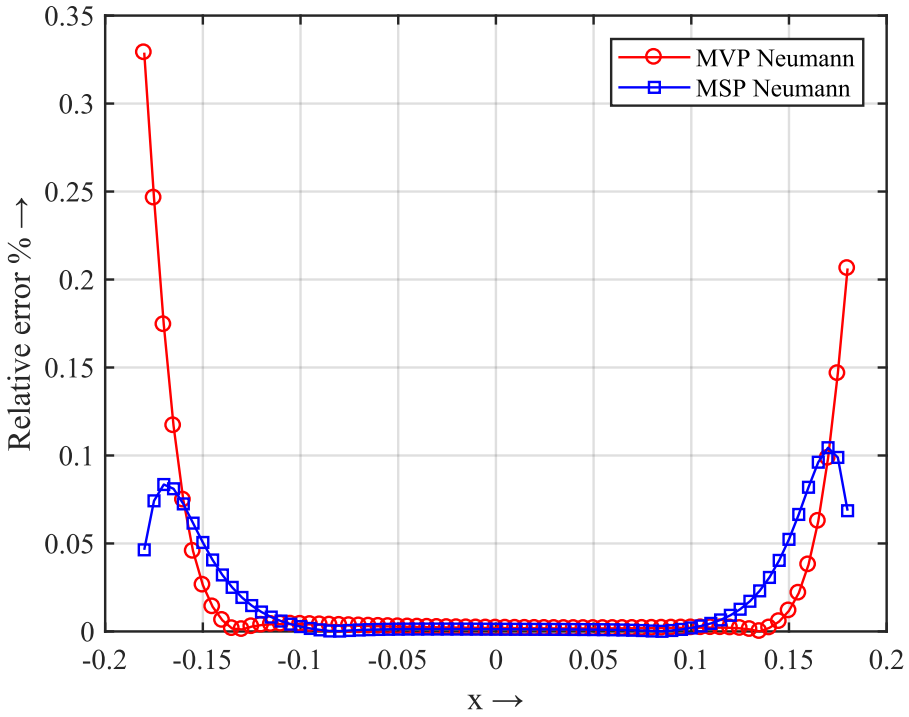

Figure 4.16: Relative error in field reconstruction with quadratic BEM over the mid line $\{-180 \text{ mm} \leq x \leq +180 \text{ mm}, y = 0\}$ starting from $K - 1$ Neumann boundary conditions.

Chapter 5

Processing Simulated Data

In order to validate the BEM implementation and estimate the expected accuracy in the field reconstruction, we first process data simulated by ROXIE for the two-dimensional numerical model of a C-shaped dipole magnet, shown in Fig. 5.1. The ROXIE (Routine for the Optimization of magnet X-sections, Inverse field calculation and coil End design) software program package is an important tool that has been developed for the design of the superconducting magnets for the LHC at CERN. The software is used as an approach towards the integrated design of superconducting magnets including feature-based coil geometry creation, conceptual design using genetic algorithms, optimization of the coil and iron cross-sections using a reduced vector-potential formulation, 3-D coil end geometry and field optimization using deterministic vector optimization techniques, tolerance analysis, production of drawings by means of a DXF interface, end-spacer design with interfaces to CAD-CAM for the CNC machining of these pieces, and the tracing of manufacturing errors using field quality measurements [11].

5.1 2D ROXIE computation

The 2D computations that are used neglect the field variation along the magnet axis $\{x,\ y,\ -1650 \text{ mm} \leq z \leq +1650 \text{ mm}\}$, avoiding the evaluation of fringe field effects at the magnet extremities, as shown in Fig. 5.2. The integral along the z-axis of the field simulated by Roxie in the 3D case is calculated with the trapezoidal rule at eleven points over the x-axis and compared with the trend of the field values simulated by 2D Roxie at the same points. Results are shown in Fig. 5.3.

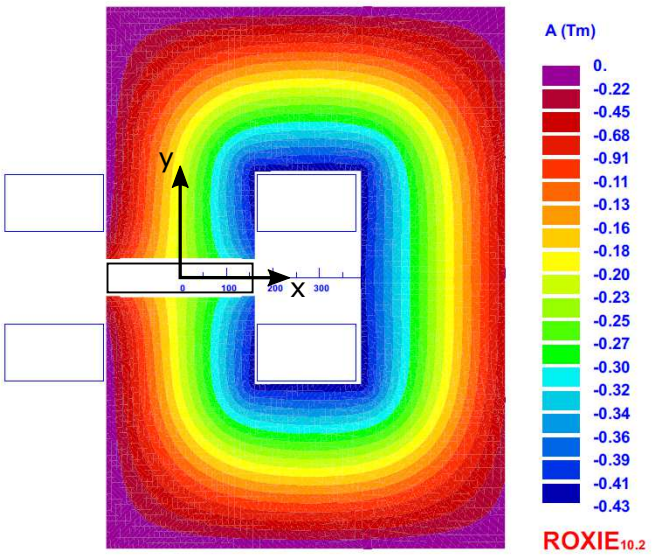

Figure 5.1: Cross section of the calibration dipole and magnetic flux density simulated by the BEM-FEM package ROXIE.

5.2 Implementation of collocation BEM

The MATLAB code developed for the collocation BEM and validated with the test problem is used to process two-dimensional ROXIE simulations.

5.2.1 Dirichlet to Neumann map

Magnetic vector potential values are simulated at equidistant points (5 mm) over the rectangular boundary $\{-160 \text{ mm} \leq x \leq +160 \text{ mm}, -30 \text{ mm} \leq y \leq +30 \text{ mm}\}$, and used as Dirichlet boundary conditions for the collocation BEM implementation. The solution of the boundary integral equation provides Neumann data from Dirichlet data; therefore the tangential components can be computed from the normal components to the boundary (i.e., the outward fluxes) and can be compared with the ROXIE simulations (Fig. 5.4). The absolute error plotted in Fig. 5.5 shows that the error in the BEM reconstruction increases when the field variation is high. However, it can be noticed that the error at the corners is smaller. This is due to the fact that a tangential component can't be defined in these points, and for this reason the value is computed with Roxie as the average between the components of the interested sides. This procedure is similar to the one carried out by BEM, and consequently the reconstructed and computed values tend to be close to each other.

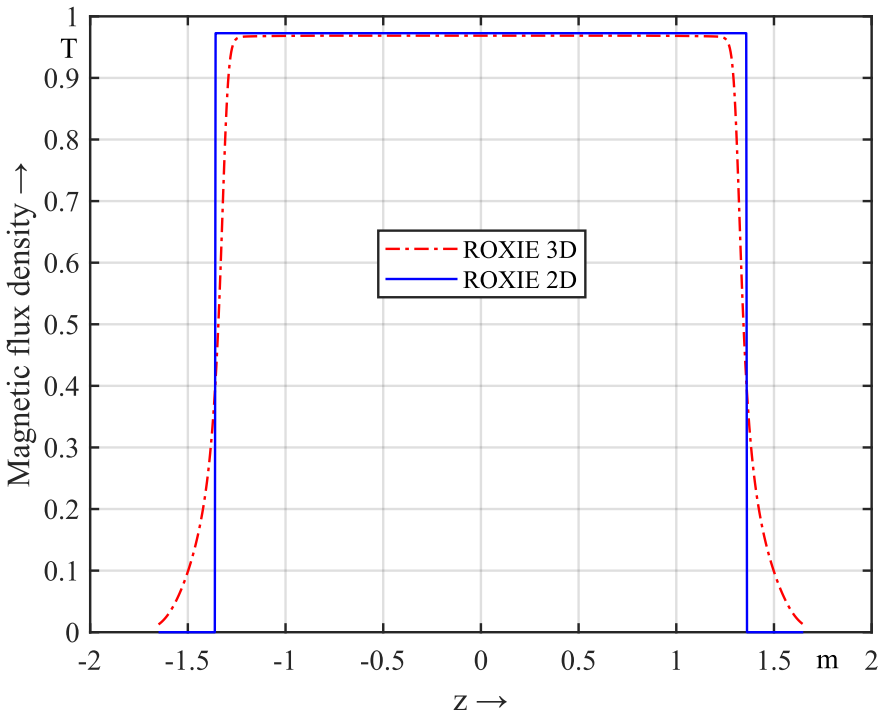

Figure 5.2: Magnetic flux density trend along the magnet axis $\{x = 0,\ y = 0\}$ for the 2D and 3D case. The magnetic length for 2D simulation (hard-edge model) is calculated such that the two integrals coincide.

A convergence analysis is shown in Fig. 5.6 for the relative error norm defined as

$$\varepsilon = \frac{\sqrt{\sum_{k=1}^{K} \left| B_t^{(k)} - B_t'^{(k)} \right|^2}}{\sqrt{\sum_{k=1}^{K} \left| B_t'^{(k)} \right|^2}} , \tag{5.1}$$

where $B_t^{(k)}$ and $B_t'^{(k)}$ are the tangential components reconstructed by BEM and computed by Roxie, respectively, at the k-th node of the boundary. K is the total number of boundary nodes.

5.2.2 Field reconstruction

The vertical component of the magnetic flux density is reconstructed, over the central line $\{-155 \text{ mm} \leq x \leq +155 \text{ mm}, y = 0\}$, from the boundary data and is subsequently compared with the direct solution from the ROXIE package. The resolution limit is investigated by different levels of discretization, that is, element nodes equidistantly positioned every 1, 2, 5, and 10 mm. Using quadratic shape functions,

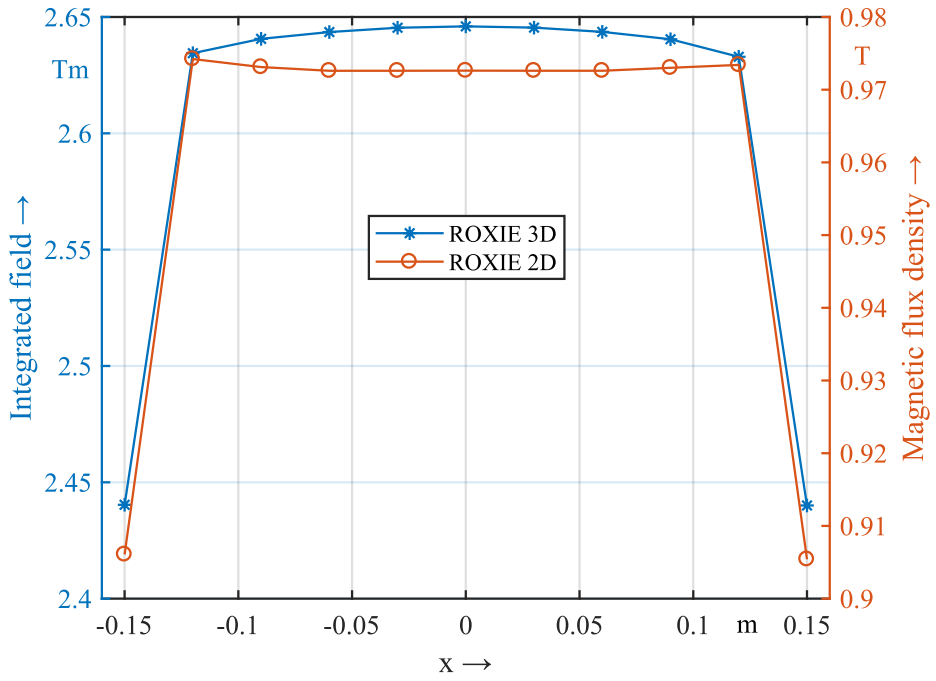

Figure 5.3: Roxie simulation, for the 2D and 3D cases, at eleven points over the central line $\{-150 \text{ mm} \leq x \leq +150 \text{ mm}, y = 0\}$.

a sufficient resolution (better than 0.3 units in 10000) is obtained for element sizes of 5 mm (Fig. 5.7).

In order to prove the stability of the method to random noise on the measured fluxes, a repeated run analysis (10^3 simulations) is carried out. Gaussian noise of zero mean is superimposed on the simulated magnetic flux density values at the BEM nodes. The standard deviation is considered to be $1.86 \cdot 10^{-5}$ T, a value motivated by the uncertainty in the measurements. Since the BEM reconstruction inside the domain is a linear combination of the magnetic flux density values on its boundary, the mean value of the error converges to zero. Fig. 5.8 shows the standard deviation of the relative error in the reconstruction of the main component of the magnetic flux density, defined as

$$e\left(x\right) = \frac{B\left(x\right) - B'\left(x\right)}{B'\left(x\right)} \ , \tag{5.2}$$

where B and B' are the field values reconstructed and simulated, respectively. It is about one order of magnitude lower than the standard deviation of the Gaussian noise added to the boundary data. This demonstrates the averaging effect of the BEM reconstruction on random noise on the boundary data.

Since the BEM allows to reconstruct the MVP values, and consequently the field, at any points inside the domain, a field vector plot is represented in Fig. 5.9. Mag-

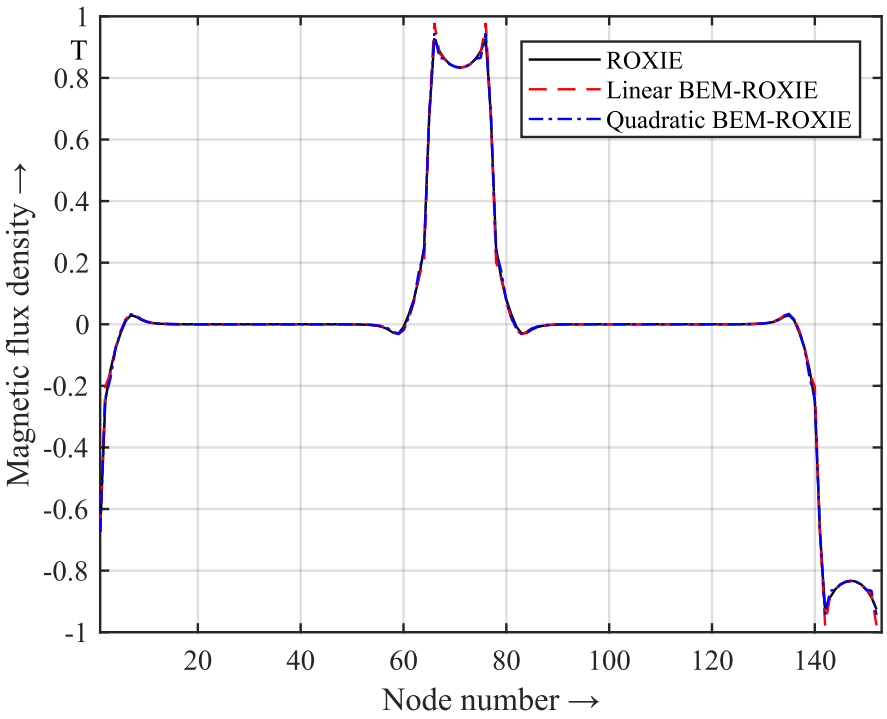

Figure 5.4: Tangential component of the magnetic flux density along the contour of the rectangle. Nodes are numbered counter-clockwise with the first node positioned in $x = -160$ mm, $y = -30$ mm., i.e., the lower left corner of the rectangle.

nitude and direction of the field are computed as combinations of the reconstructed field Cartesian components.

The field reconstruction can be evaluated in terms of field quality

$$Q(x,y) = \frac{\sqrt{[B_y(x,y) - B_{y0}]^2 + [B_x(x,y) - B_{x0}]^2}}{\sqrt{B_{y0}^2 + B_{x0}^2}} \,, \tag{5.3}$$

where B_y and B_x are the field components reconstructed by BEM at any point (x, y) inside the domain, while the subscript "0" denotes the ones reconstructed in the center of the magnet, that is at point $x = 0$, $y = 0$. As shown in Fig. 5.9, the field is not varying significantly with respect to the reference value defined at the center of the aperture. Furthermore, it tends to be quite higher in the central region and, clearly, smaller when the vertical sides are approached. The two "holes" identify the border between these two regions.

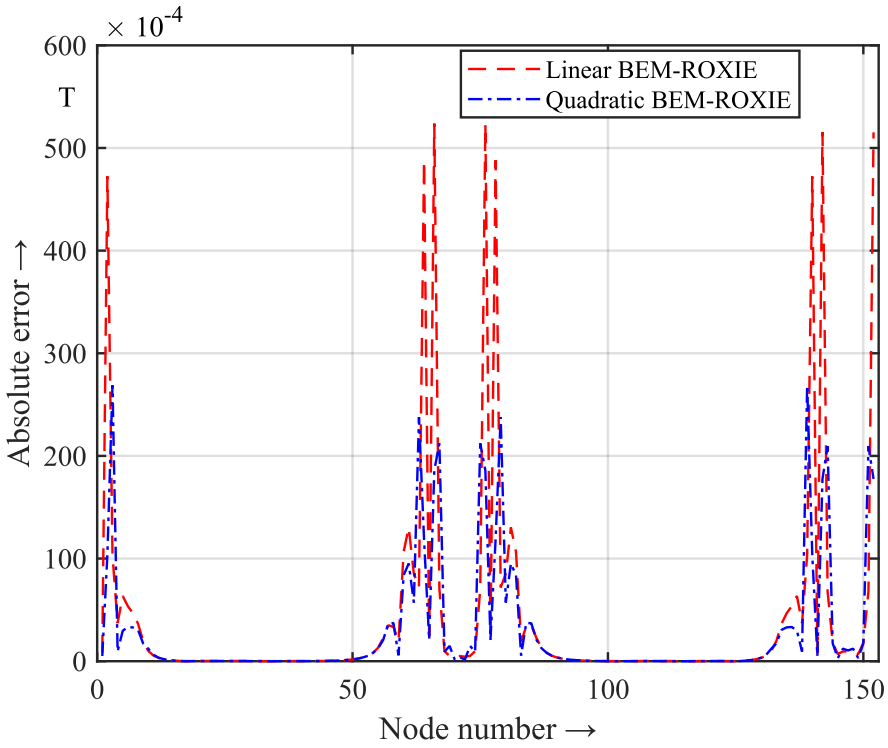

Figure 5.5: Absolute error associated to Fig. 5.4. Values are plotted in 10^{-4} Tesla. Boundary corners are located at nodes number 1, 65, 77 and 141.

5.2.3 Field harmonics computation

The theory explained in Appendix A is now applied to the simulated data. We consider a circle with reference radius $r_0 = 22$ mm, centered firstly in $x = 0$, $y = 0$ and then shifted to $x = 100$ mm , $y = 0$. Values of relative normal multipole coefficients b_n are computed directly by Roxie, until the 20-th order, for the two different positions. At the same time, the Cartesian components of the field **B** are reconstructed by BEM (quadratic elements, 5 mm) at $N = 120$ points over the same circles. The radial field component B_r is then calculated as

$$B_r(r_0, \varphi) = B_x(r_0, \varphi)\cos(\varphi) + B_y(r_0, \varphi)\sin(\varphi) \ , \tag{5.4}$$

and then expanded until the 20-th harmonic in order to retrieve the interested multipole coefficients. A comparison of the results for the two different positions is shown in Fig. 5.10 and Fig. 5.11.

Different levels of BEM discretization are investigated in this case too, that is, element nodes equidistantly positioned every 1, 2 and 10 mm, as well as the "standard" evaluation at 5 mm. The analysis is carried out in Fig. 5.12 for the circle centered in $x = 100$ mm , $y = 0$.

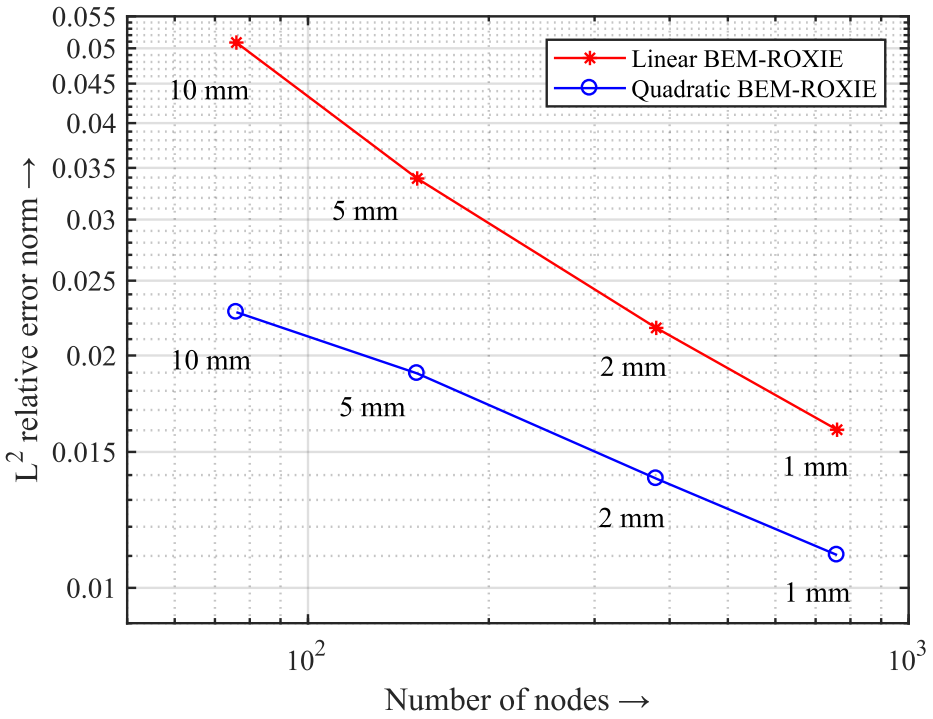

Figure 5.6: Convergence analysis in the L^2 relative error norm. Different levels of discretization are employed, i.e. nodes equidistantly positioned every 10, 5, 2 and 1 mm, i.e. for an increasing number of boundary nodes.

5.3 Implementation of Galerkin BEM

Until now only collocation BEM has been considered. We compare at this point the results obtained with linear elements with the ones obtained by means of the Galerkin method.

Fig. 5.13 compares the vertical component of the magnetic flux density simulated by ROXIE along the line $\{-150 \text{ mm} \leq x \leq +150 \text{ mm}, y = 0\}$ with the one reconstructed by collocation and Galerkin BEM at the same points of the internal domain. Results can be analyzed from Fig. 5.14, where the relative error of the BEM reconstruction, with respect to the simulated values, are displayed for the two methods. As we can see, collocation BEM is most accurate method in this evaluation.

Coherent results are obtained in Fig. 5.15, where the convergence analysis of the relative error is performed for different levels of boundary discretization.

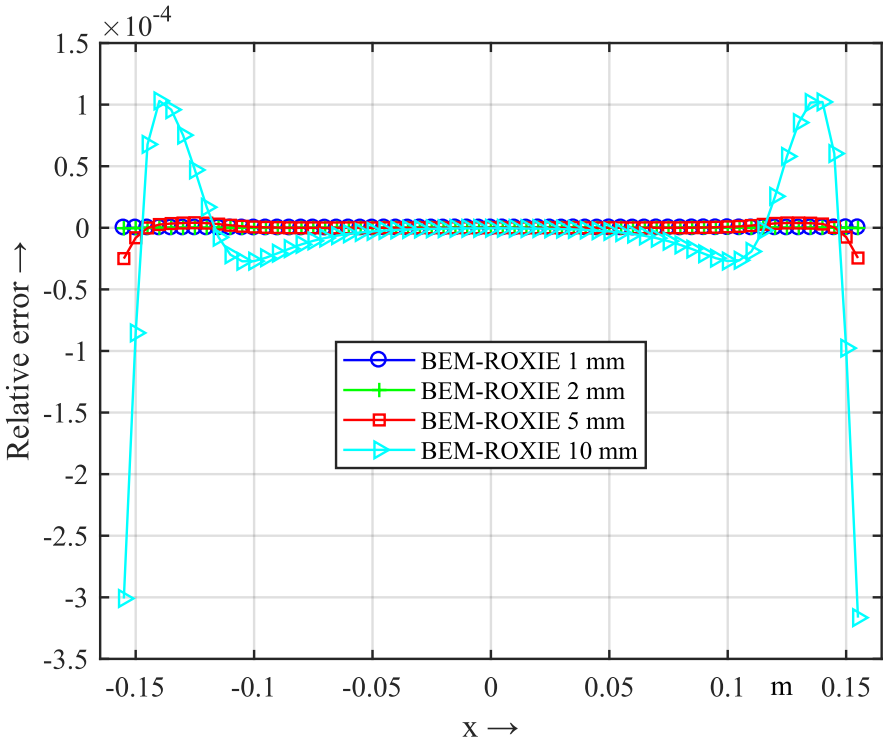

Figure 5.7: Relative error in the BEM (quadratic elements) reconstruction of the vertical component of the magnetic flux density along the central line $\{-155 \text{ mm} \leq x \leq +155 \text{ mm}, y = 0\}$, given as a function of the mesh size.

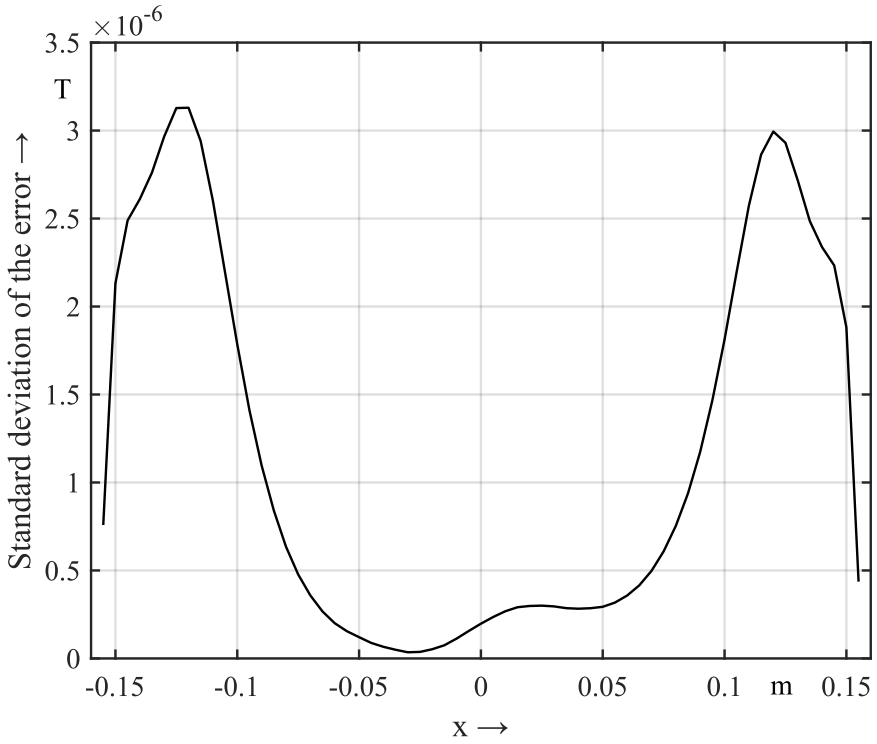

Figure 5.8: Standard deviation of the relative error in the reconstruction of the main component of the magnetic flux density over the central line $\{-155 \text{ mm} \leq x \leq +155 \text{ mm}, y = 0\}$.

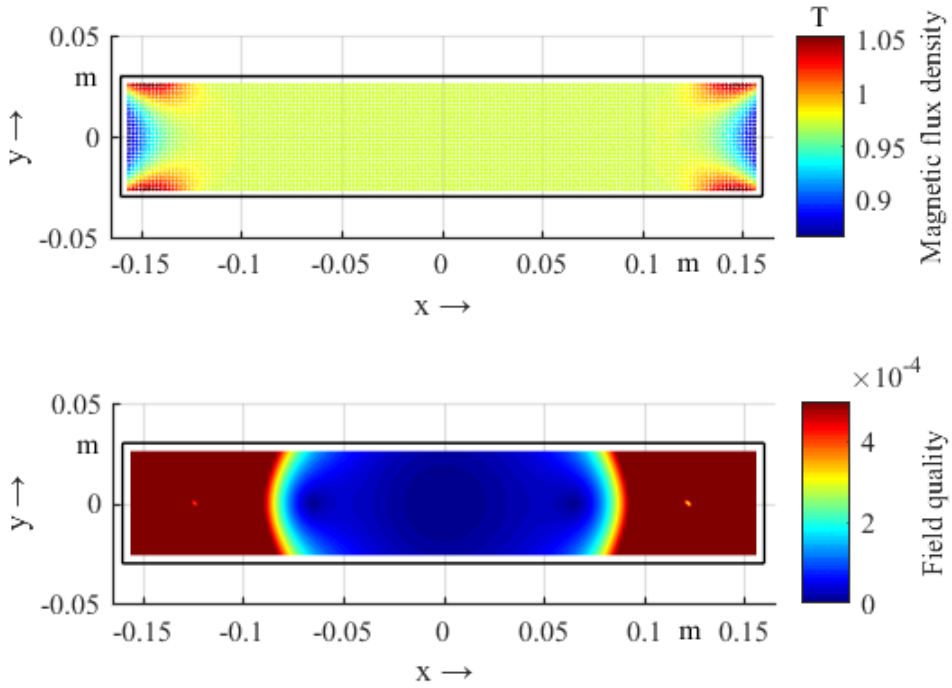

Figure 5.9: Top: Vector representation of the magnetic flux density inside the domain $\{-160 \text{ mm} \leq x \leq +160 \text{ mm}, -30 \text{ mm} \leq y \leq +30 \text{ mm}\}$. Bottom: Field quality representation in the same domain. Values are limited at $5 \cdot 10^{-4}$ units.

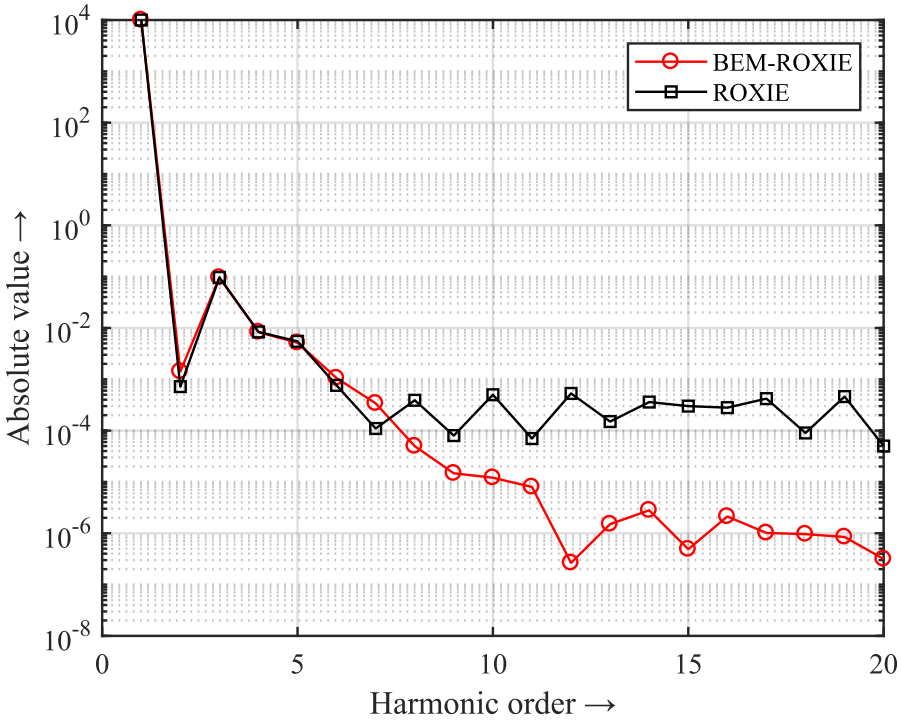

Figure 5.10: Comparison of relative normal multipole coefficients b_n, computed over a circle with radius $r_0 = 22$ mm centered in $x = 0$, $y = 0$. Values are normalized with respect to the main field component at the center of the circle and plotted as units in 10^{+4}.

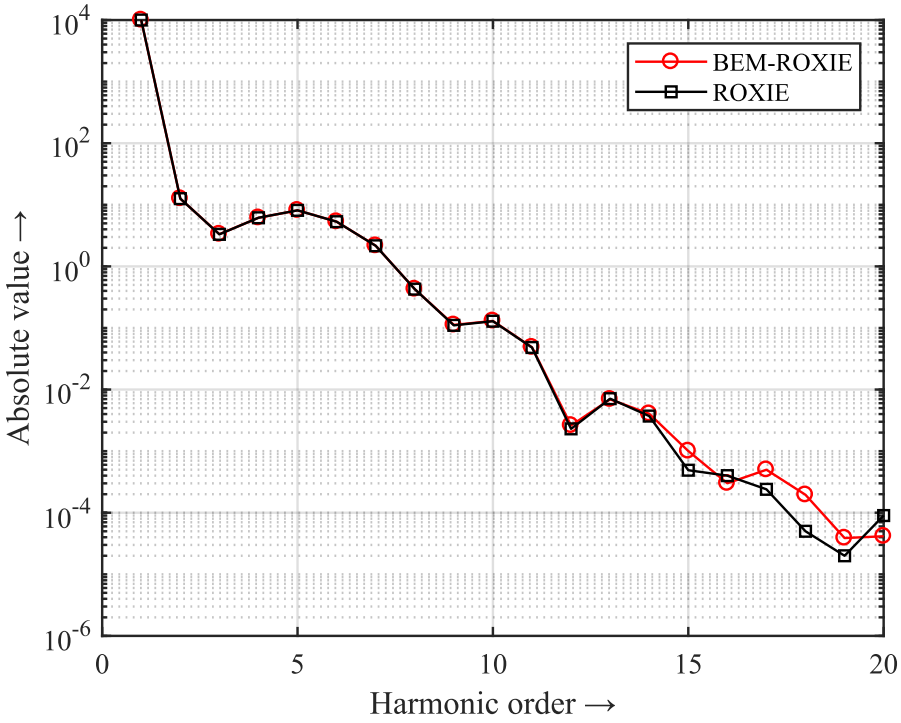

Figure 5.11: Comparison of relative normal multipole coefficients b_n, computed over a circle with radius $r_0 = 22$ mm centered in $x = 100$ mm , $y = 0$. Values are normalized with respect to the main field component at the center of the circle and plotted as units in 10^{+4}.

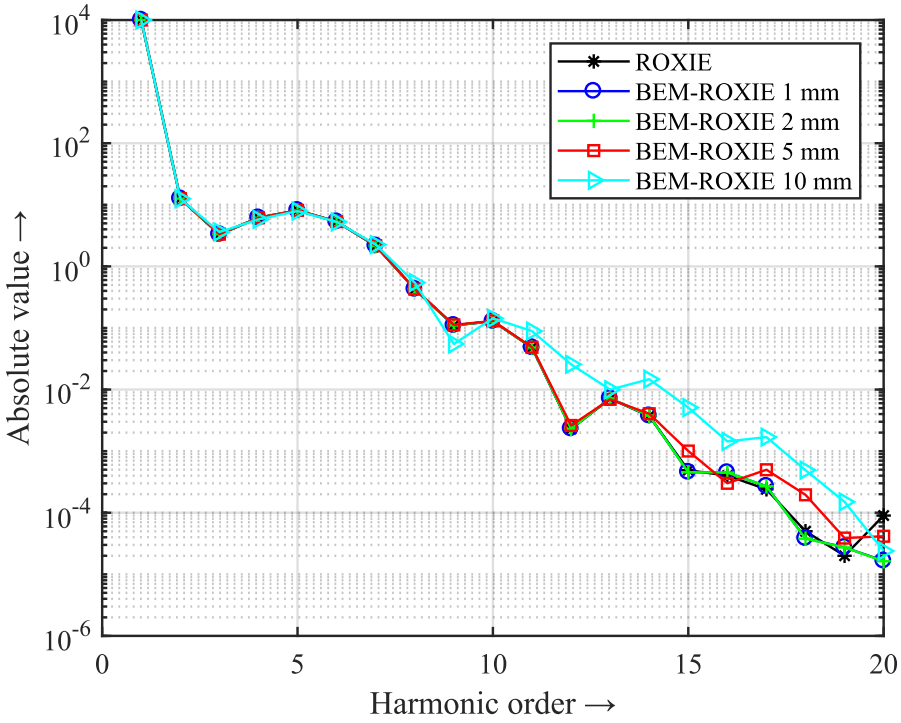

Figure 5.12: Convergence analysis in the reconstruction of relative normal multipole coefficients b_n, computed over a circle with radius $r_0 = 22$ mm. Values are normalized with respect to the main field component at the center of the circle and plotted as units in 10^{+4}.

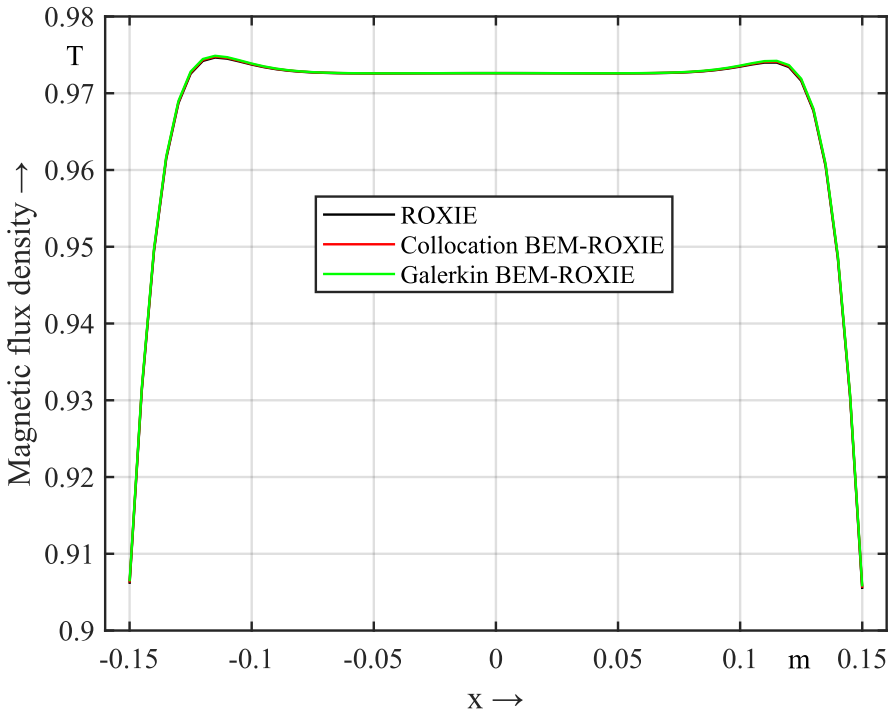

Figure 5.13: Magnetic flux density reconstructed by two different BEM methods along the mid-line $\{-150 \text{ mm} \leq x \leq +150 \text{ mm}, y = 0\}$. Comparison with ROXIE simulated data.

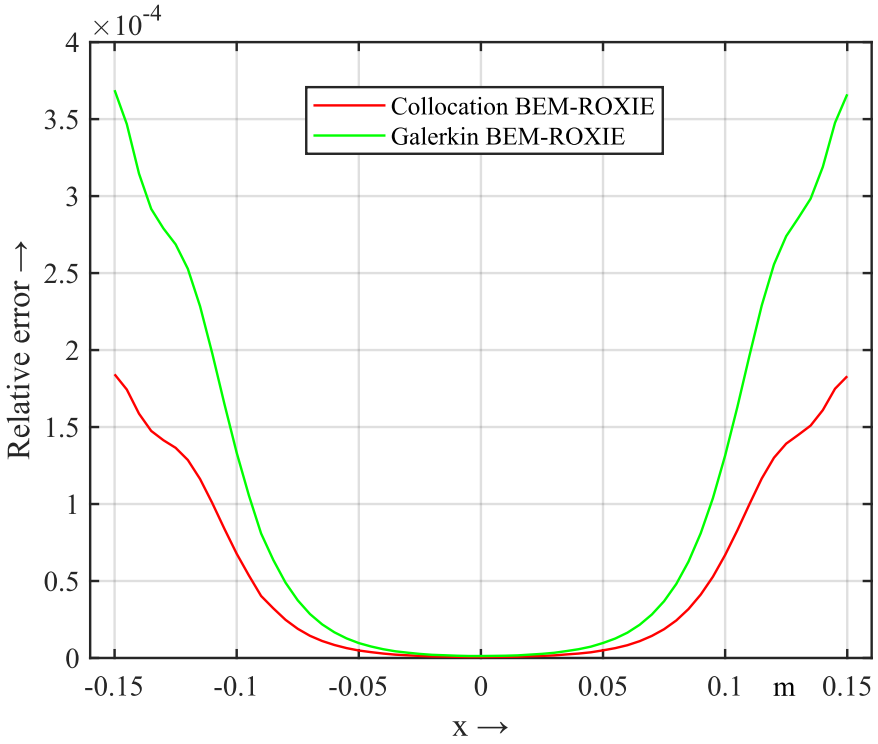

Figure 5.14: Relative error associated to Fig. 5.13.

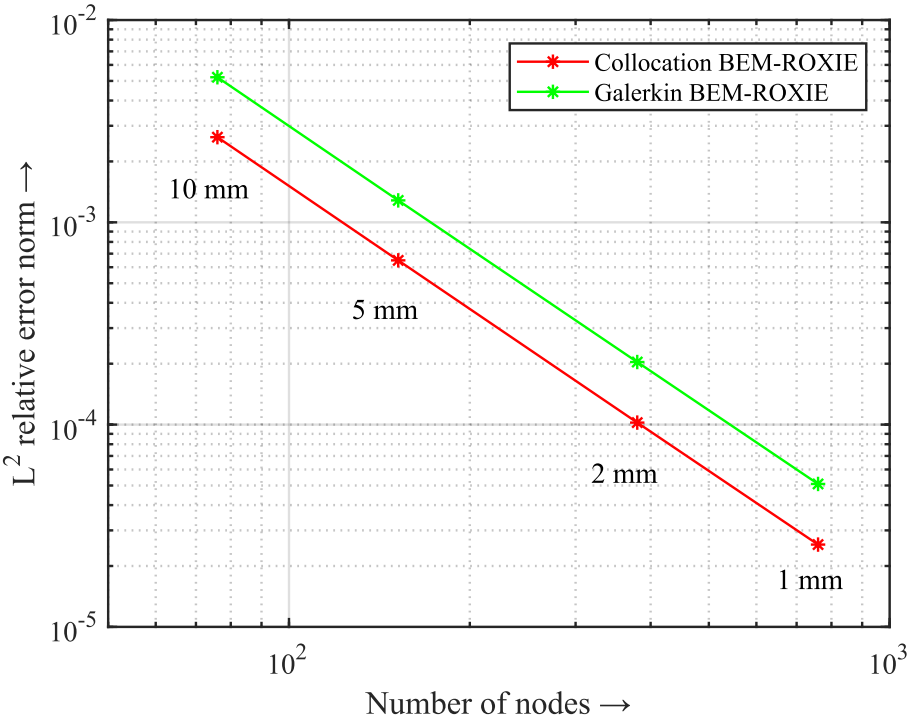

Figure 5.15: Convergence analysis in the L^2 relative error norm for the BEM reconstruction over the line $\{-150 \text{ mm} \leq x \leq +150 \text{ mm}, y = 0\}$. Different levels of discretization are employed, that is, nodes equidistantly positioned every 10, 5, 2 and 1 mm.

Chapter 6

Processing Measured Data

In the previous chapters the proposed BEM processing technique has been validated by means of a test problem and ROXIE simulated data. We finally process measured data in order to prove the correctness and the usefulness of the method. For this purpose, a stretched-wire system is employed for the measurements inside the aperture of the MCB22 dipole magnet (Fig. 6.1). This kind of magnets, available in the Magnetic Measurement section's lab, are mainly used as reference magnets for the calibration of magnetic field transducers.

Figure 6.1: Single-stretched-wire system, in translating mode, mounted on the MCB22 reference dipole magnet.

6.1 The single-stretched-wire system

The stretched-wire based system can be considered as reference equipment to measure main field strength and direction in static field dipole and quadrupole with high accuracy [12]. This method is based on a single, Copper-Beryllium (Cu-Be), conducting wire of 0.125 mm in diameter, guided by two precision displacement stages at which the two end-points of the wire are fixed by ceramic ball bearings and kept electrically on a floating potential. The wire is displaced within the magnet aperture and pulled taut by means of a servo motor (Fig. 6.2). The relative position of the wire is known with an accuracy of 1 µm. Finally, the return wire is routed through a field free region.

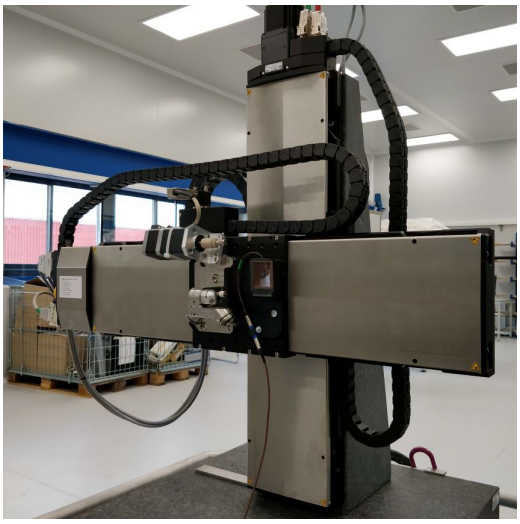

Figure 6.2: Precision displacement stage and wire-tension motor for the stretched-wire system.

The voltage drop across the connection terminals, when the wire is moving inside the magnetic field, is measured and directly integrated by a fast digital integrator (FDI) in order to get the flux linked with the surface that is traced out by the wire displacement. The advantage of this technique concerns mainly the possibility to take measurements on magnets with small apertures and large aspect ratio. In fact, this is a limit for another standard device used for measuring integrated magnetic fields, namely, the rotating coil magnetometer. In this system, the coil intercepts the magnetic flux at a radius given by the dimensions of the measurement shaft, that comprises a set of induction coils. For magnets of a rectangular aperture with aspect ratio larger than 3:1, the cylindrical domain will cover only a portion of the magnet aperture [13]. We therefore investigate on an alternative sampling technique which is able to extend the covered domain and which is not bound to specific trajectories.

6.1.1 Theoretical aspects

The voltage at the terminals of a moving conductive loop can be calculated with the Faraday law in global form

$$U = -\frac{d\Phi}{dt} \ , \tag{6.1}$$

where Φ is the magnetic flux through a surface S and U is the voltage induced along its boundary ∂S. The global Faraday law is related to the Maxwell equation by

$$\mathbf{E} = -\nabla\phi - \frac{\partial \mathbf{A}}{\partial t} \ , \tag{6.2}$$

via

$$\Phi = \iint_S \mathbf{B} \cdot d\mathbf{S} = \oint_{\partial S} \mathbf{A} \cdot d\mathbf{r} \ . \tag{6.3}$$

This can be proved as follows: the Lorentz force on a moving particle with charge Q in a static magnetic field is given by

$$\mathbf{F} = Q(\mathbf{E} + \mathbf{v} \times \mathbf{B}) \ , \tag{6.4}$$

where the integral of $\mathbf{v} \times \mathbf{B}$ along the wire is called electromotive force (EMF) and can be written as

$$\int_{\partial S} (\mathbf{v} \times \mathbf{B}) \cdot d\mathbf{r} = -\int_{\partial S} \mathbf{B} \cdot (\mathbf{v} \times d\mathbf{r}) \ , \tag{6.5}$$

where $(\mathbf{v} \times d\mathbf{r})dt = d\mathbf{S}$ is the surface traced by the line element $d\mathbf{r}$ over the time interval dt, as shown in Fig 6.3. Therefore results

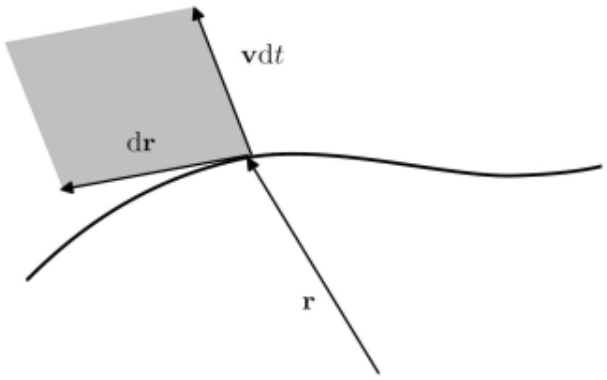

Figure 6.3: Surface traced by the moving line element over dt.

$$\oint_{\partial S} (\mathbf{v} \times \mathbf{B}) \cdot d\mathbf{r} = -\iint_S \frac{d}{dt}(\mathbf{B} \cdot d\mathbf{S}) = -\frac{d\Phi}{dt} \ , \tag{6.6}$$

that is, the motional EMF given by the line integral of the electric flux density is the time rate of change of linked flux in the loop. However, closed loops are not required for the application of (6.5).

6.1.2 Integrated field in dipole magnets

Provided that the loop resistance is sufficiently small compared to the voltmeter input resistance (and therefore the current in the wire can be neglected) the terminal voltage is U. The integrated voltage in (6.6) is proportional to the surface swept $d\mathbf{S}$, which, by moving the straight line segment of the stretched-wire in the x-direction, yields

$$\int_{t1}^{t2} U dt = \int_{t1}^{t2} \int_{0}^{l} (\mathbf{v} \times \mathbf{B}) dz dt = \int_{x1}^{x2} \int_{0}^{l} B_y dz dx = [x_2 - x_1] I(B_y) \ , \qquad (6.7)$$

where l is the magnetic length of the magnet. Given the start and final wire positions x_1 and x_2, we can deduce the field integral $I(B_y)$. For a perfect dipole, the integration of the measured voltage signal provides the field integrated over l as an average over x, where $x_1 \leq x \leq x_2$.

6.1.3 Uncertainty analysis

The integrated field values are measured with an accuracy of 5 units in 10^{-4} at nominal field. At each boundary node (x_k, y_k), three measurement repetitions are acquired ($m_k^{(1)}$,$m_k^{(2)}$,$m_k^{(3)}$); we computed the field value and its uncertainty as the average $\bar{m}_k$ and the standard deviation σ_k of these values. Since we know from previous experiences that the standard deviation is $4.9 \cdot 10^{-5}$ Tm, σ_k values can be used to roughly verify the correctness of each set of measurements.

An interesting evaluation concerns the statistical distribution of the standard deviations at the nodes of the horizontal and vertical sides of the boundary. Since on the vertical sides the processed values are integrated fields $\bar{B}_x$ in fringe field regions, we deal with low signal-to-noise ratio. This is why higher values of uncertainty are expected with respect to the horizontal side evaluation, as shown in Fig 6.4 - 6.5.

6.1.4 Limitations

The wire in the magnet aperture and the cabling to the integrator creates a loop sensitive to electromagnetic interferences. In some particular conditions, like small magnet apertures, the displacement range of the wire is limited, and thus the signal-to-noise ratio (SNR) of the induced voltage is low. This procure a high uncertainty on the magnetic center measurement position and on the field harmonics [12]. However, collecting data closed to the magnet poles is an advantage, since here the measured signal is high and consequently the SNR is maximized.

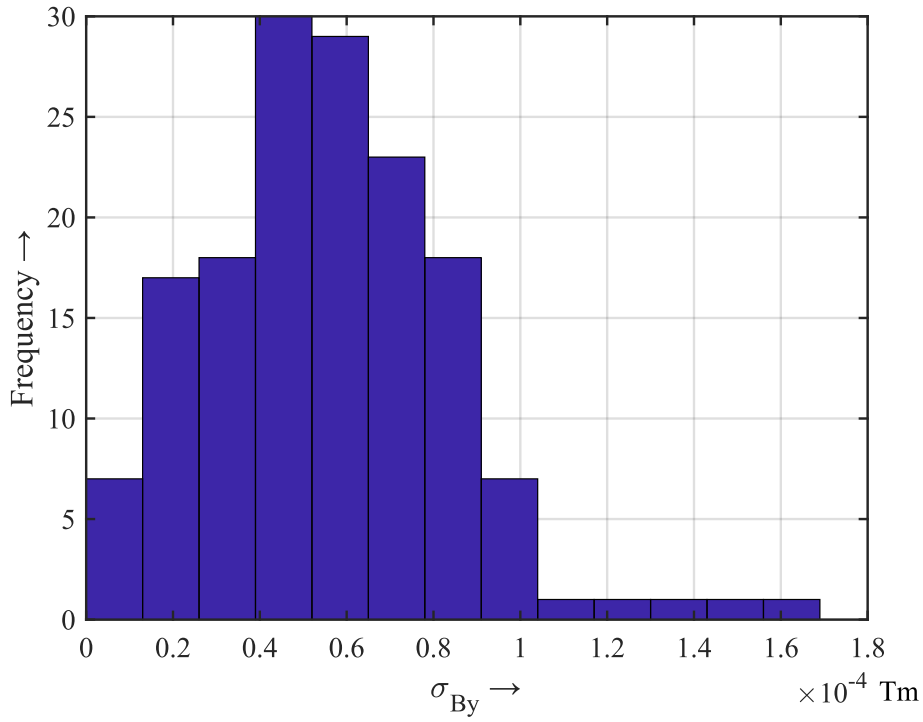

Figure 6.4: Distribution of the standard deviation for $\bar{B}_y$ measurements at the nodes of the horizontal sides of the boundary. Mean value is $5.5 \cdot 10^{-5}$ Tm.

Moreover, the measurements that belongs to the x and y displacements cannot be combined together, since they are carried out in different conditions: During the acquisition process, both wire sag, fringe fields due to magnetic equipments and the presence of the earth magnetic field have different effects on the horizontal and vertical flux linkages. The latter is mainly affected by these effects.

6.1.5 Acquisition of boundary data

The measurements are collected at equidistant points over the boundary (5 mm). At point (x_k, y_k) the stage is moved in the sequences $\{x_k, x_k + 5\,\text{mm}, x_k - 5\,\text{mm}, x_k + 5\,\text{mm}, x_k\}$ and $\{y_k, y_k + 5\,\text{mm}, y_k - 5\,\text{mm}, y_k + 5\,\text{mm}, y_k\}$ in order to measure the flux linked to the surface traced in the horizontal and vertical direction, respectively. The two long strokes (10 mm) are used for measuring the flux through the corresponding elements adjacent to the central point. Two strokes are necessary for correcting the integrator drift. The choice of a swept surface area $10\,\text{mm} \times 2.65\,\text{m}$ is dictated by maximizing the SNR during the acquisition process. As a consequence, a superposition of the integrated field measurements arises when they are collected

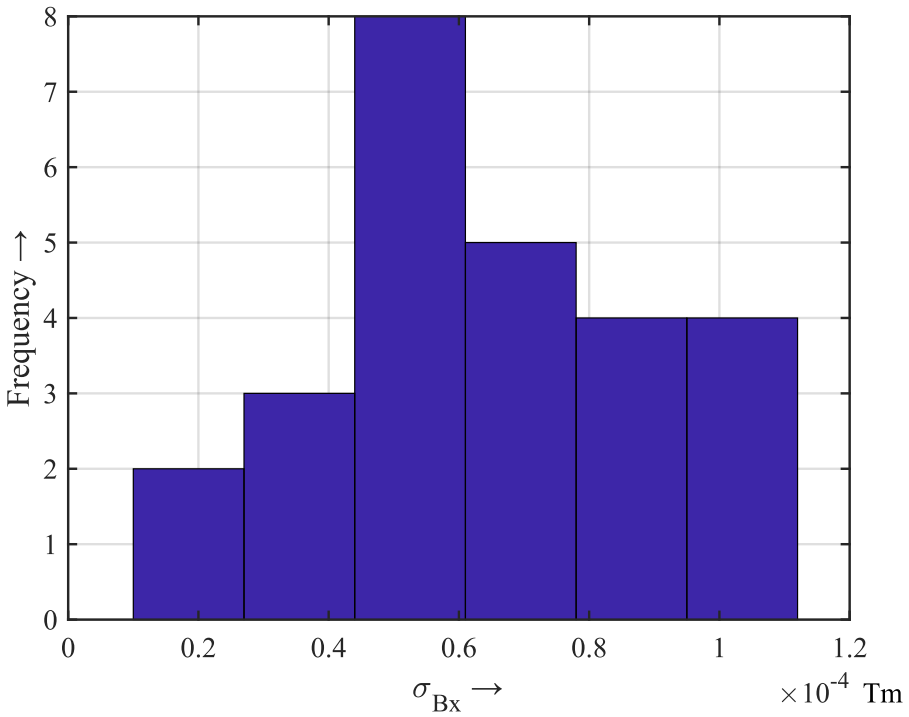

Figure 6.5: Distribution of the standard deviation for $\bar{B}_x$ measurements at the nodes of the vertical sides of the boundary. Mean value is $6.5 \cdot 10^{-5}$ Tm.

along the boundary. This fact is an advantage, since it is possible to retrieve the flux crossing the surfaces traced between each couple of nodes as differences between adjacent values.

Notice that, dividing the flux linkage by the traced surface and collocating this to the point (x_k, y_k) yields an intrinsic error, because the field distribution cannot be considered neither constant nor linear. For this reason the implementation is performed directly by means of the available flux measurements.

The procedure is developed starting from the central measurement m_0, since at this point the flux symmetry condition can be applied correctly

$$\Phi_{+1} = \Phi_{-1} = \frac{m_0 \cdot w}{2} = \frac{M_0}{2} \ , \tag{6.8}$$

where w is the wire shift, that is 10 mm. Since $[m_0]$=Tm or Wb/m, it is clear that M_0 is a flux, defined in units of weber. Fig. 6.6 shows the application of the symmetry condition at the central point. The central measurement M_0 is split into two equal parts. Once the values of the flux $\Phi_{\pm 1}$ at the center of one side are known,

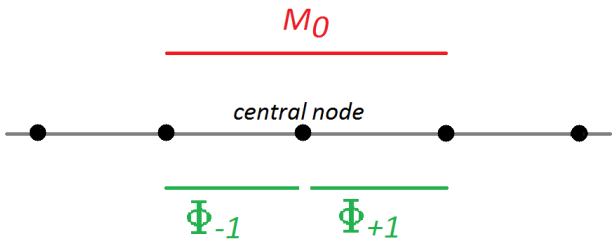

Figure 6.6: Symmetry of the flux at the central node. This assumption is effective over each side of the rectangle.

it is possible to retrieve step by step the other values of the flux over that side

$$\Phi_{\pm i} = M_{\pm(i-1)} - \Phi_{\pm(i-1)} \ . \tag{6.9}$$

This procedure has the further advantage to avoid the use of the measurements taken

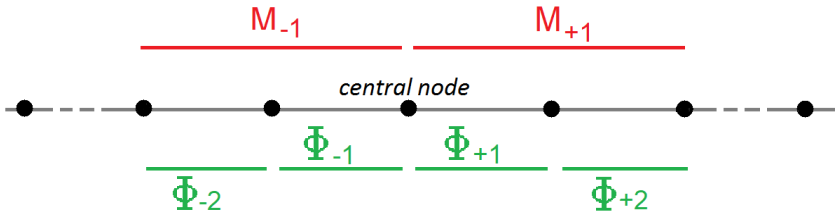

Figure 6.7: Step by step computation of fluxes from measurements.

at the edges of each segment, that is, at the corners of the rectangular boundary. Once all the fluxes Φ are retrieved, it is possible to compute the integrated magnetic vector potential defined as

$$\bar{A}_z\,(x,y) = \int_{-z_0}^{+z_0} A_z\,(x,y,z)\,dz \ , \tag{6.10}$$

where $[\bar{A}_z]$=Wb.

Indicating with P_k, $k = 1,\ldots,K$, the BEM nodes over the boundary of the rectangle (with $P_{K+1} = P_0$), when moving from point P_k to point P_{k+1} (Fig. 6.8) the stretched-wire intercepts the flux Φ_k through the surfaces S_k. Employing Stokes' theorem, this flux is given by (6.3)

$$\Phi_k = \int_{S_k} \mathbf{B}\cdot \mathrm{d}\mathbf{a} = \int_{P_{k+1}}^{Q_{k+1}} A_z \mathrm{d}z - \int_{P_k}^{Q_k} A_z \mathrm{d}z \ , \tag{6.11}$$

under the assumption that the wire stages are located in the field-free region, that is, $\int_{P_k}^{P_{k+1}} A_x\,\mathrm{d}x = \int_{Q_k}^{Q_{k+1}} A_x\,\mathrm{d}x = 0$. The set of integrals (6.11) constitutes the following

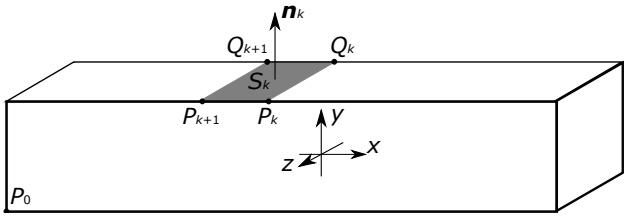

Figure 6.8: Parallelepiped traced by the stretched-wire. Actually, the dimension in z is much larger than in the transverse plane xy.

linear system of equations

$$\bar{A}_z\left(P_{k+1}\right) - \bar{A}_z\left(P_k\right) = \Phi_k \ , \quad k = 1, \ldots, K \ , \tag{6.12}$$

which can be solved to obtain the values of $\bar{A}_z$ at the boundary nodes. In order to assure the uniqueness of the solution of (6.12), the value of $\bar{A}_z\left(P_0\right)$ is set to zero. The same procedure applies for all the four sides of the rectangle, where the reference value at the first node is the last one retrieved over the previous side. The boundary nodes are oriented in the counterclockwise sense: This means that the measured values have to be arranged consequently, such that they represent fluxes pointing out of the boundary. Usually, when the magnetic length l is well known, the magnetic vector potential A_z is introduced as the average of its integrated value $\bar{A}_z$ over l, where $A_z = \bar{A}_z / l$.

6.2 Implementation of collocation BEM

Measurements are collected at $P = 176$ equally spaced points, that is every 5 mm, along the rectangular boundary $\{-190 \text{ mm} \leq x \leq +190 \text{ mm}, -30 \text{ mm} \leq y \leq +30 \text{ mm}\}$. The size of the magnet aperture is $\{-160 \text{ mm} \leq x \leq +160 \text{ mm}, -30 \text{ mm} \leq y \leq +30 \text{ mm}\}$, thus fringe field regions will be evaluated too (Fig. 6.9).

Once the procedure shown in Section 6.1.5 is carried out for the measurements, magnetic vector potential values A_z, where $[A_z]$=Wb/m, are available at the boundary nodes for the implementation as Dirichlet boundary conditions (Fig. 6.10).

6.3 Measurements validation based on Ampere's and Gauss' laws

The discretized forms of Ampere's and Gauss' law are evaluated numerically for the set of measurements gathered along the closed boundary of Fig. 6.9. At each p-th node, the stretched-wire intercepts the flux linked to the surface $w \cdot l$, where w is the wire shift (0.01 m) and l is the magnetic length (2.65 m), tracing movements parallel

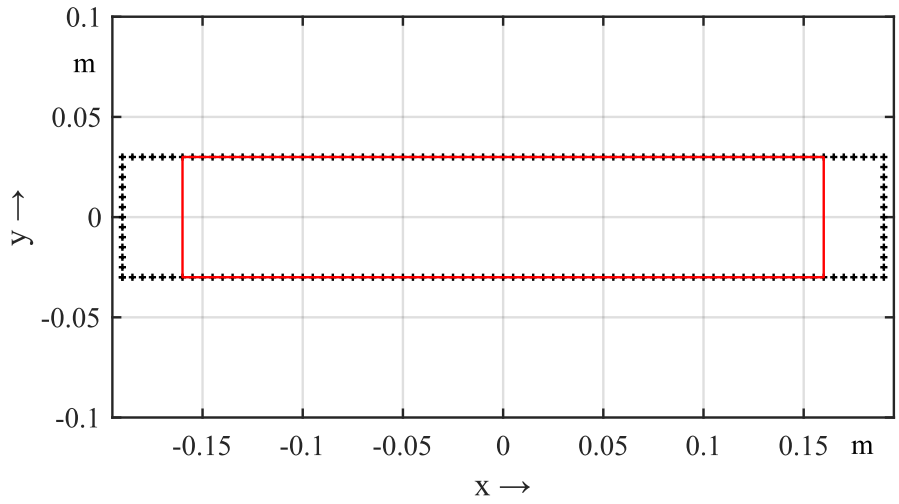

Figure 6.9: Position of stretched-wire measurements (p black crosses), collected on a rectangular boundary, with respect to the actual magnet aperture (red line).

to the X and Y axis. Hence, we can retrieve the normal and tangential components of field **B** at the nodes of the boundary, assuming a constant field distribution over the swept surface.

- Ampere's circuital law

  The point-wise value of the field B_t at node p is obtained from the measured integrated field m as an average value over the length l

  $$B_t^{(p)} = \frac{m_p}{l} \ . \tag{6.13}$$

  At this point we compute

  $$\sum_{p=1}^{P} \frac{B_t^{(p)}}{\mu_0} \cdot \frac{w}{2} = 13.04 \text{ A} \ , \tag{6.14}$$

  where $w/2$ is the length of one element of the boundary. The result shows that, since the magnet aperture is free of any sources, an error is arising from this computation. In particular, this error is comparable to a fictitious filamentary current of 13 A placed at the center of the domain and directed along the z direction.

  In terms of relative values, with respect to the reference tangential field measured at the center of the right vertical side, results

  $$\frac{\sum_{p=1}^{P} B_t^{(p)}}{B_t^{ref}} = 6.2 \cdot 10^{-3} \ . \tag{6.15}$$

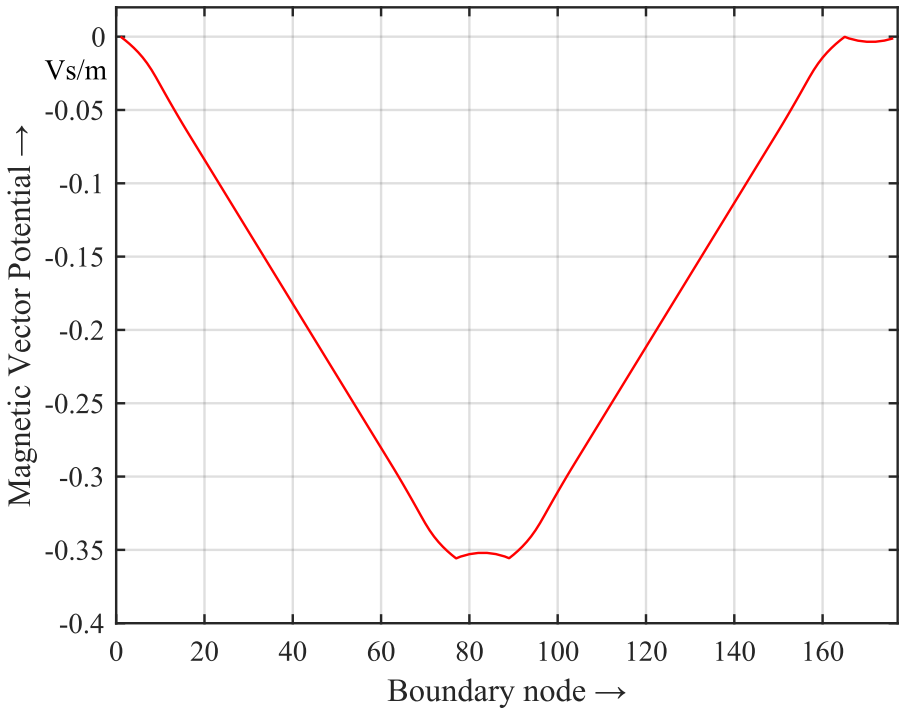

Figure 6.10: Trend of the magnetic vector potential A_z along the rectangular boundary. Nodes are numbered anti-clockwise starting from the point (-190 mm, -30 mm).

- Gauss' flux theorem

  For this evaluation, we use directly the measured integrated value of the field component normal to the boundary as

  $$\sum_{p=1}^{P} \bar{B}_n^{(p)} \cdot \frac{w}{2} = -9.62 \cdot 10^{-7} \text{ Wb} \, . \tag{6.16}$$

  Clearly, the net total flux crossing a closed surface should be zero for solenoidal fields. This means that the error arising in (6.16) is comparable to a loss of magnetic flux inside the magnet aperture.

  In terms of relative values, with respect to the field at the center of the upper horizontal side, results

  $$\frac{\sum_{p=1}^{P} \bar{B}_n^{(p)}}{\bar{B}_n^{ref}} = -7.39 \cdot 10^{-5} \, . \tag{6.17}$$

The errors in (6.15) and (6.17) arise mainly due to the assumption of a constant distribution of the field over the traced surface. As can be seen, this approximation

affects mostly the computation of the tangential component, since at the vertical sides of the boundary the field distribution deals with high variations, whereas is almost constant in the center of the aperture 6.11. With the same principle, we

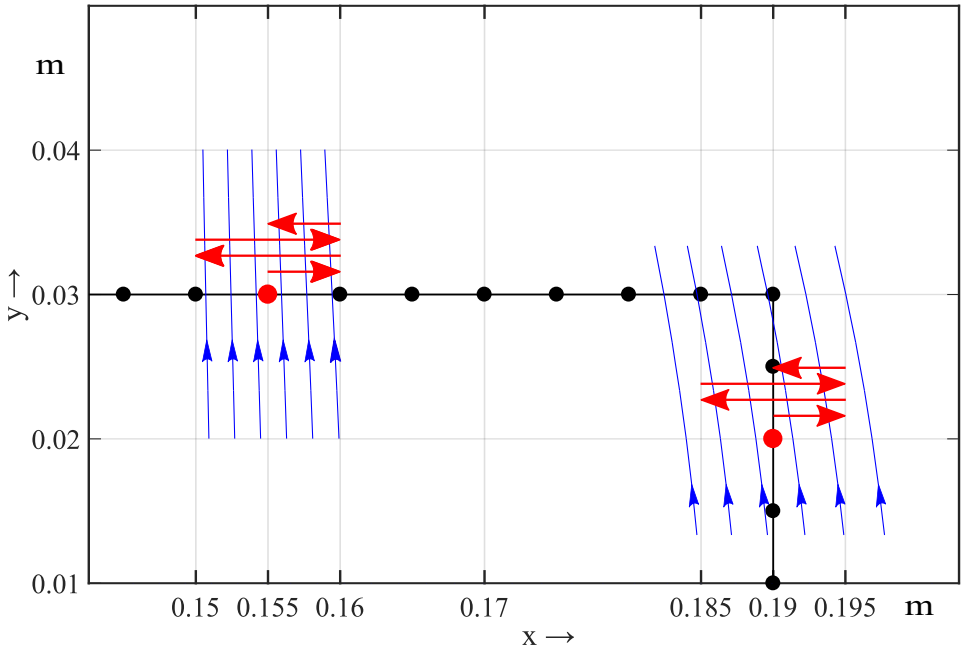

Figure 6.11: Measurement of fluxes and collocation of the field values (red points). The red arrows indicate the displacement sequence of the stretched wire system. The computation of the tangential component from the flux measurements orthogonal to the boundary is highly inaccurate.

can compute the Gauss' flux theorem for the flux values obtained from the procedure shown in Section 6.1.5, which are actually used for the computation of BEM boundary data

$$\sum_{p=1}^{P} \Phi^{(p)} = 6.8 \cdot 10^{-7} \text{ Wb} \ . \tag{6.18}$$

In terms of relative values, with respect to the flux measured at the center of the upper horizontal side, results

$$\frac{\sum_{p=1}^{P} \Phi^{(p)}}{\Phi^{ref}} = 5.2 \cdot 10^{-5} \ . \tag{6.19}$$

These values are acceptable, hence the set of measurements can be considered suitable for the implementation.

6.4 Dirichlet to Neumann map

The values of the magnetic vector potential A_z, calculated at each node and plotted in Fig. 6.10, are used as Dirichlet boundary conditions for the collocation BEM implementation. Since the solution of the boundary integral equation provides Neumann data starting form the Dirichlet ones, we can retrieve the tangential component of the field at the same positions along the contour. A comparison is shown in Fig. 6.12. The values of the field B_t measured by the stretched-wire system (SSW) are compared to the Neumann data $\partial A_z/\partial \mathbf{n}$, with the opposite sign, reconstructed by BEM (BEM-SSW). Both linear and quadratic elements are used, so that we can evaluate which of the two methods fits better the case under study. As Fig. 6.12

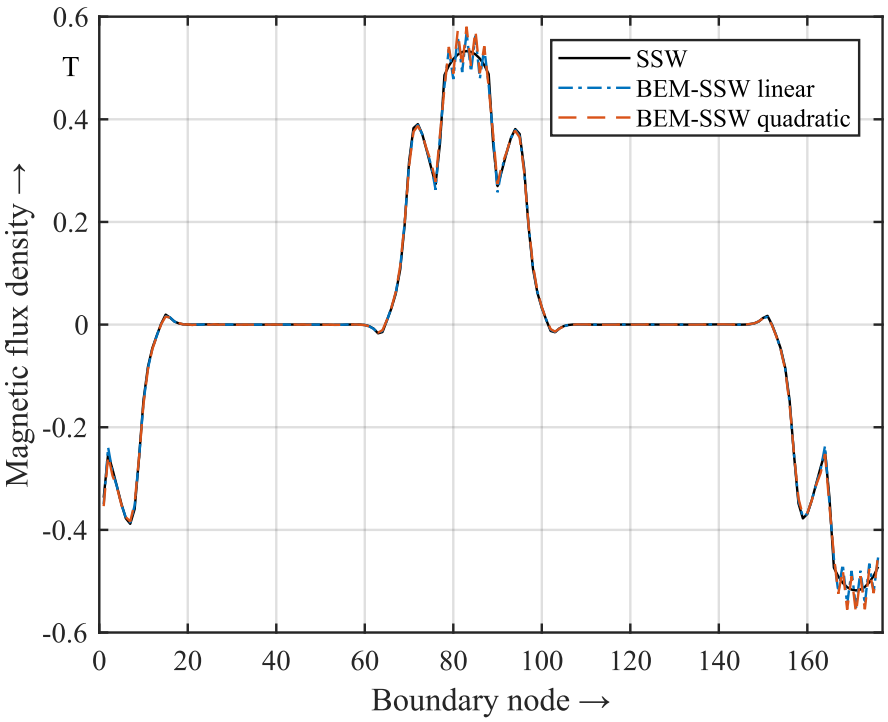

Figure 6.12: Comparison between field tangential values measured and reconstructed by BEM at the p nodes of the boundary.

and Fig. 6.13 show, linear BEM is the best solution for our case, and for this reason it will be the only one employed from now on. Furthermore, the absolute error is particularly higher when the vertical sides are approached: this fact arises because of the high variation of the field at the extremities of the aperture.

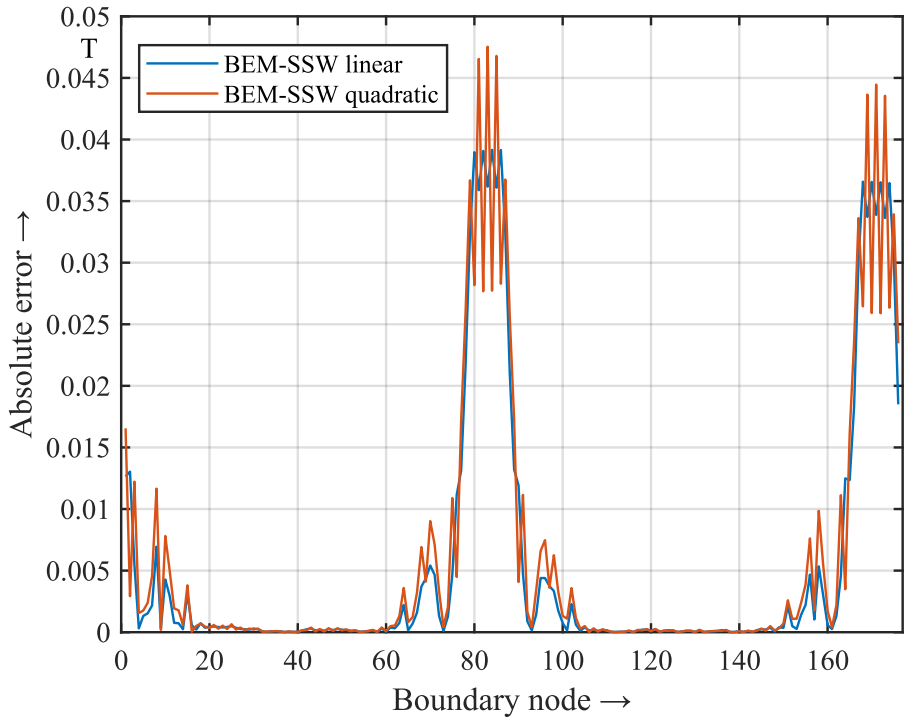

Figure 6.13: Absolute error related to Fig. 6.12. Boundary corners are located at node number 1, 77, 89 and 165.

6.5 Reconstruction at internal points of the domain

Since the magnetic vector potential obeys the Laplace equation in the rectangle, it is possible to reconstruct A_z values at any point of the domain starting from boundary data.

6.5.1 Reconstruction along the central line

The magnetic flux measured through y-oriented surfaces at the mid line $\{-180\text{ mm} \leq x \leq +180\text{ mm}, y = 0\}$ is compared with the one reconstructed by BEM starting from boundary data. Since the boundary conditions are potential values $[A_z]$=Wb/m, the reconstructed fluxes, calculated as A_z differences, are defined as per unit (magnetic) length (p.u.l.) values. This means that the available measured data have been processed accordingly, that is, they describe the flux crossing y-oriented surfaces with area 10 mm x 1 m. Results of Fig. 6.14 show a good agreement. From the zoomed view of Fig. 6.15 it can be observed that the BEM reconstruction filters random noise from the measurements; this is done by averaging over a large number of elements and attenuating high-frequency signals through the weighting by the

Green's kernel. The same comparison is carried out for the magnetic flux through

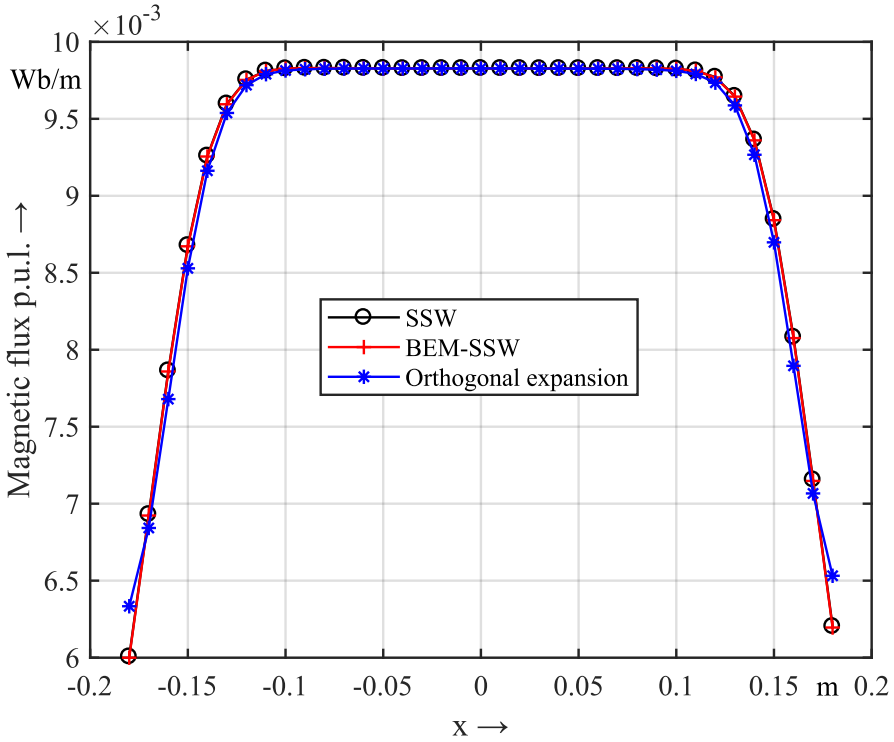

Figure 6.14: Magnetic flux (p.u.l.) crossing y-oriented surfaces at the central line $\{-180 \text{ mm} \leq x \leq +180 \text{ mm}, y = 0\}$. The A_z values are reconstructed at the extremities of elements with length 10 mm and fluxes are assumed to be positioned at the center of each element. Asymmetry is due to the manufacture features of the magnet.

x-oriented surfaces. We refer here to the x-component of the magnetic field $\mathbf{B}$, where [$\mathbf{B}$]=T, such that the reconstructed values are computed as differentiation of the magnetic vector potential. Results are shown in Fig. 6.16. The fact that this field component is not zero at the magnet center can be explained by a misalignment of the magnet plane with the horizontal axis of the wire system. The roll-angle of misalignment can be computed from BEM reconstruction as

$$\phi = \arcsin\left(\frac{B_x}{B_y}\right) = -0.027 \text{ mrad} \ , \tag{6.20}$$

where B_x and B_y are the field components reconstructed at the center of the magnet, that is, at point (0,0).

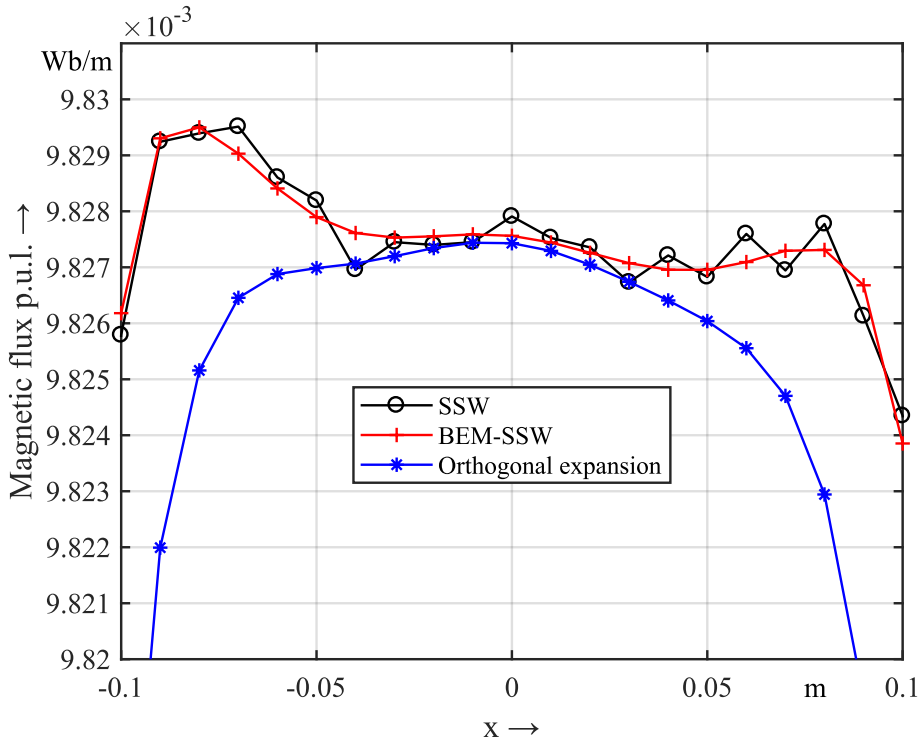

Figure 6.15: Zoomed view of Fig. 6.14.

6.5.2 Field quality representation

A useful representation of the magnetic field measured, or reconstructed, inside the rectangular domain, is the field quality Q, defined as

$$Q(x,y) = \left| \frac{B(x,y) - B_0}{B_0} \right| \ , \tag{6.21}$$

where B is one of the two Cartesian components of the magnetic field and B_0 is the reference value, at the center of the magnet, for that component.

Note that, for the single-stretched-wire system, due to the earth magnetic field, fringe field from the magnetic equipment, non-orthogonality of the wire stages, and calibration errors that have a different effects on the measured horizontal and vertical flux measurements, the x and y components of the field cannot be combined together. This is why, in Fig. 6.17 and Fig. 6.18, the field quality is computed for the y and x component separately. Field quality results shows some asymmetries that can be consequence of layer jumps in the excitation coils and high current interconnections. Anyway, the BEM reconstruction can be considered good for both the components.

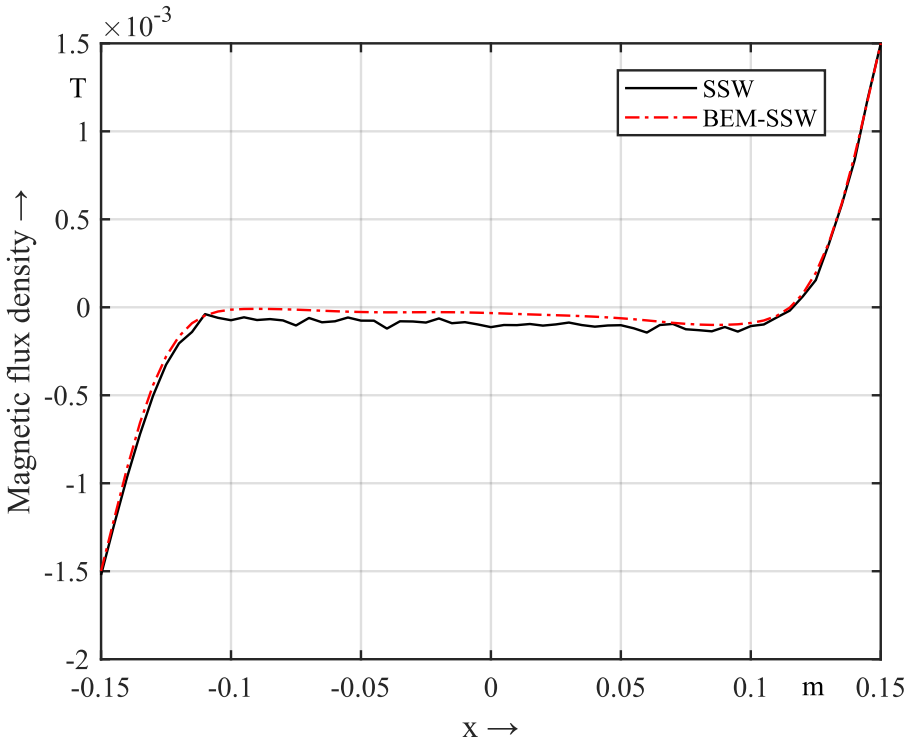

Figure 6.16: x-component of the field **B** over the central line $\{-150 \text{ mm} \leq x \leq +150 \text{ mm}, y = 0\}$. Comparison between measured and reconstructed values.

6.6 Reconstruction from Neumann boundary conditions

The fact that the single-stretched-wire system measures fluxes is the reason why, until now, the BEM has been implemented with Dirichlet boundary conditions, that are the values of the magnetic vector potential. In this way, any sort of approximation is introduced on the starting data and there is no systematic error on the total flux through adjacent nodes. However, if the field distribution is assumed to be constant over the surface traced by the wire, we can determine the x and y component of **B** at the nodes of the boundary, that are, clearly, rough estimates due to the nonlinear field distribution over the sampled area. This approach allows the implementation of the BEM with Neumann boundary conditions, which can be the set of field normal or tangential component if we refer to MSP or MVP formulation, respectively.

In the following, integrated field values derived from flux measurements are used as boundary conditions on the boundary and as reference values for the comparison on the mid line $\{-100 \text{ mm} \leq x \leq +100 \text{ mm}, y = 0\}$. The results in Fig. 6.19 and Fig. 6.20 confirm the outcome of Section 6.3. The approximation of a constant

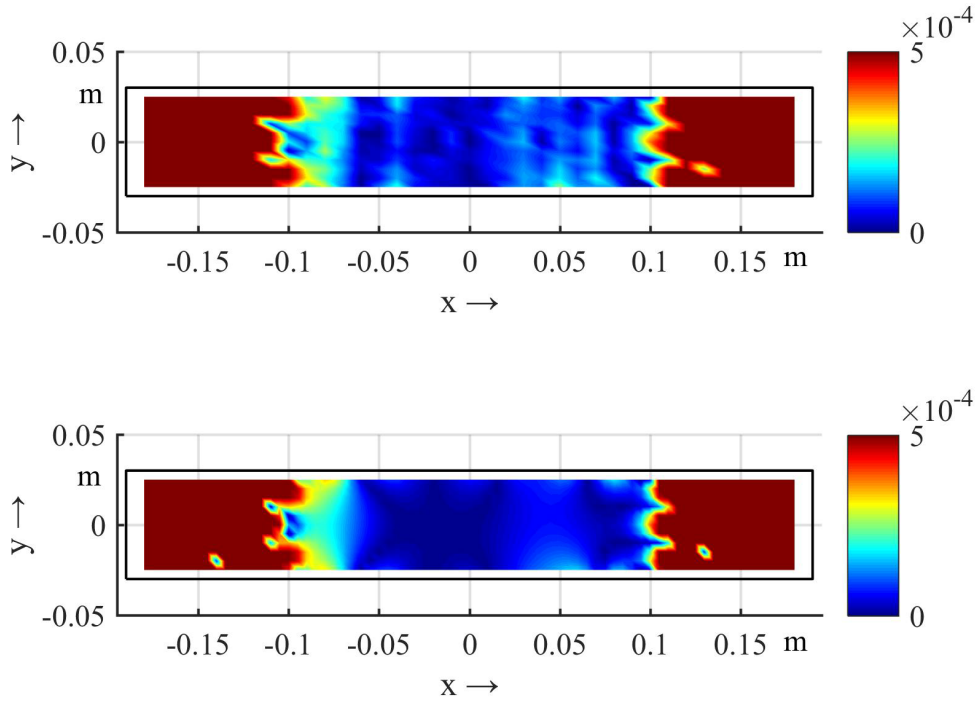

Figure 6.17: Field quality representation for the field y component. Comparison between measured values (top) and reconstructed values from boundary data (bottom), over an internal grid. Values are limited at 5 units in 10^{-4}.

field distribution can be considered acceptable only for the normal component of the field. The reason is displayed in Fig. 6.11.

6.7 The "Dog-Bone" domain

The Boundary element method reconstruction is not limited to rectangular domains. In order to prove the applicability to more complex domains, measurements have been collected along the contour shown in Fig. 6.21. Results of the implementation of Linear elements collocation BEM are represented inside the domain as field map and field lines (Fig. 6.22).

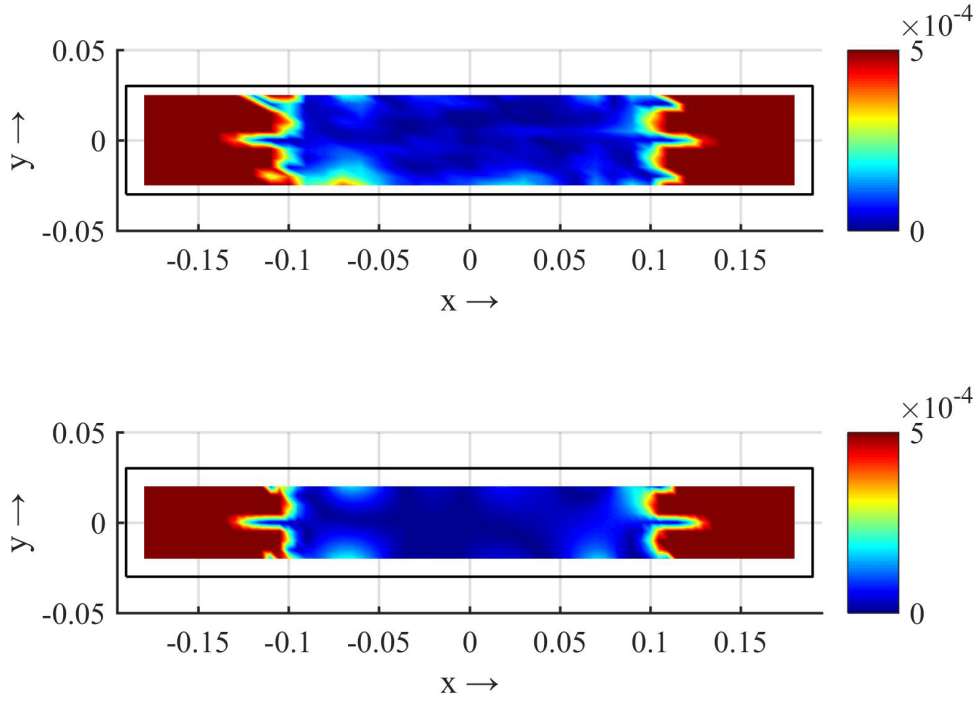

Figure 6.18: Field quality representation for the field x component. Comparison between measured values (top) and reconstructed values from boundary data (bottom), over an internal grid. Values are limited at 5 units in 10^{-4}.

6.8 Field harmonics computation

The theory developed in Section 6.1.5 is now introduced for the set of measurements acquired with the stretched-wire system. Flux measurements are collected at N equally spaced points along circles with reference radius r_0=30 mm and centered at 5 different positions on the X axis (y=0). At each point (x_k, y_k) over the circle, the stages are moved in the sequence $\{x_k,\ x_k+2.5\text{ mm},\ x_k-2.5\text{ mm},\ x_k+2.5\text{ mm},\ x_k\}$ and $\{y_k,\ y_k+2.5\text{ mm},\ y_k-2.5\text{ mm},\ y_k+2.5\text{ mm},\ y_k\}$ in order to acquire values proportional to the field Cartesian components B_y and B_x, respectively. Clearly, the field values are retrieved by the flux measurements assuming a constant field distribution over the swept surface with area equal to 5 mm x 2.65 m. Once the field Cartesian components are retrieved at point (x_k, y_k), the radial component can be calculated as

$$B_r(r_0, \varphi_k) = B_x(r_0, \varphi_k)\cos(\varphi_k) + B_y(r_0, \varphi_k)\sin(\varphi_k)\ . \tag{6.22}$$

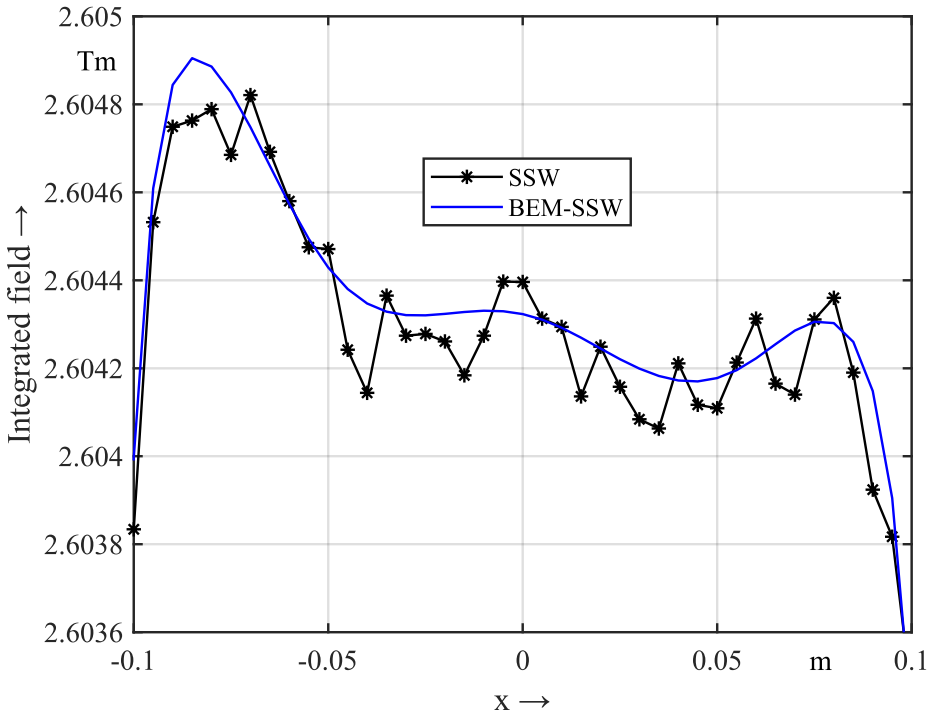

Figure 6.19: Comparison of integrated field values measured and reconstructed by BEM starting from Neumann boundary data. MSP formulation.

However, as explained before, the combination of the x and y components leads to an intrinsic error due to the different nature of the measurements.

The fields B_x, B_y and B_r are then expanded and the associated multipole coefficients are retrieve from Table A.1. At the same time, the magnetic potential A_z is reconstructed by BEM at each k-th point of the circle. This allows the computation of multipole coefficients even from the A_z expansion. The computed multipole coefficients are compared in Fig. 6.23, Fig. 6.24, Fig. 6.25 and Fig. 6.26 for different number of samples N and for different positions of the circle. The comparison between the four figures shows that the higher is the number of samples acquired on the circle, the more the multipole values coincide between each other. For this reason, from now on we will use only N=64. Moreover, the smaller are the values of the coefficients, the more difficult is their correct computation; as a consequence, it is difficult to calculate high order values, and in particular the ones of the Skew multipole coefficient.

In Fig. 6.27 and Fig. 6.28 we investigate the behavior of A_n and B_n as a function of the position. N=64 measurements are acquired at five different circles centered in points $(-120\text{ mm},\ 0)$, $(-60\text{ mm},\ 0)$, $(0,\ 0)$, $(+60\text{mm},\ 0)$ and $(-120\text{ mm},\ 0)$. Note

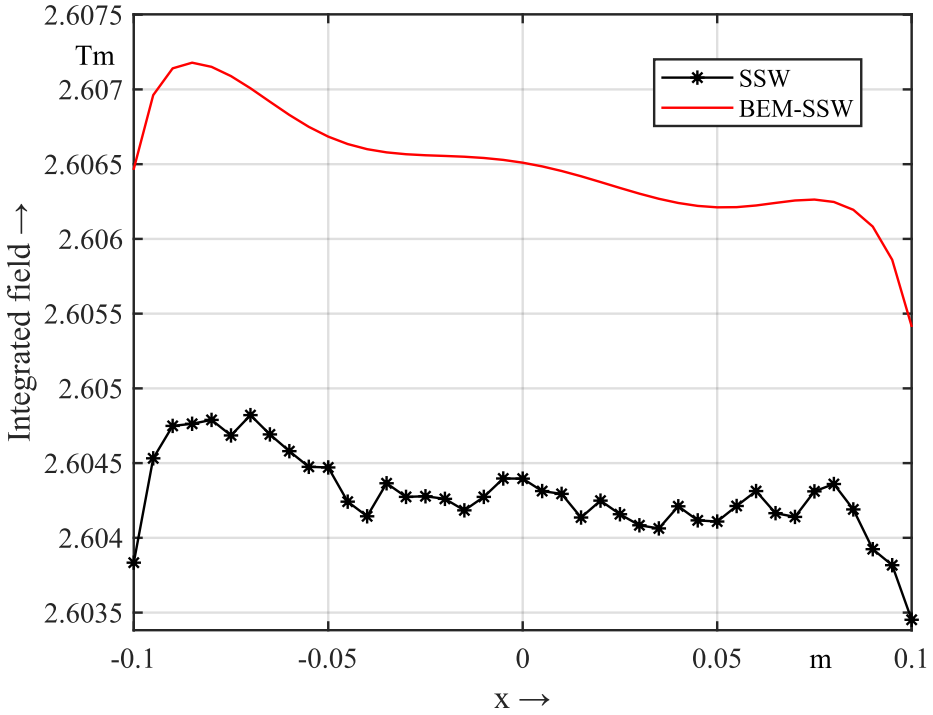

Figure 6.20: Comparison of integrated field values measured and reconstructed by BEM starting from Neumann boundary data. MVP formulation.

that the two set of multipole coefficient A_n and B_n are obtained by the expansion of the component B_x and B_y, respectively. The values of the multipole coefficients are related to the field asymmetries existing in the associated circular domain. For this reason, their evaluation can give an estimate of the quality of the field at different positions inside the magnet aperture. In particular the Normal (B_n) and Skew (A_n) multipole coefficients are linked with left/right and up/down asymmetries, respectively.

Fig. 6.26 displays the trend of the B_n coefficient for a circle centered in (0,0). For an ideal dipole, only B_1 should show up in the harmonic analysis, with a value equal to the field measured at the center of the magnet. Clearly, in the real case, higher order coefficients appear, even if with significantly smaller values. As Fig. 6.27 and Fig. 6.28 show, the field asymmetries increase the more we move out of the center. The coefficients computed in Fig. 6.27 and Fig. 6.28 can be employed for the reconstruction of the field inside the respective circular domains (see (A.17)). The field quality defined in (6.21) is computed for the x and y components inside five distinct domains, covering a large part of the magnet aperture. The comparison of these representations with the ones obtained in Fig. 6.17 and Fig. 6.18 shows a good

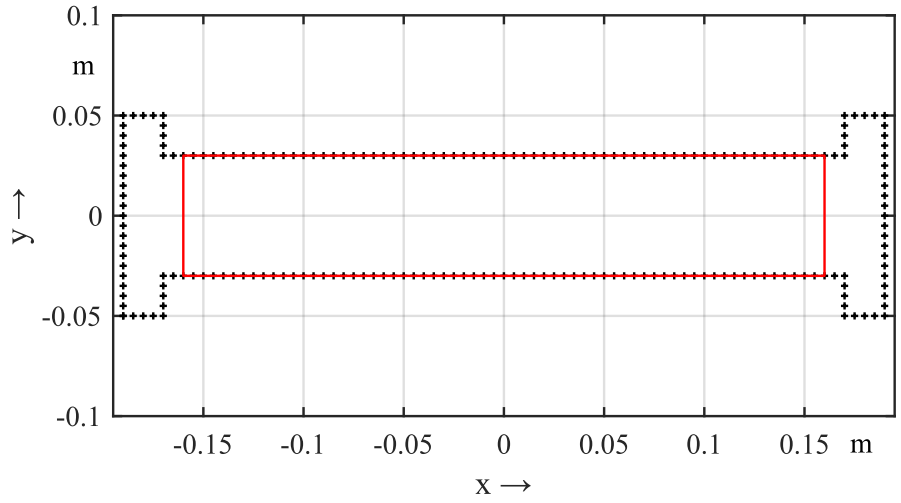

Figure 6.21: Position of measured boundary data (black crosses) with respect to the magnet aperture (red line). The "dog-bone" domain allows to evaluate fringe field regions.

agreement between the results.

The magnetic vector potential can be reconstructed inside the circular domains as well. For this reason, we can represent the equipotential lines, which coincide with the field lines. Fig. 6.31 shows the field and potential reconstruction related to the first four harmonic orders, separately. In this way, the contribution of the n-th multipole coefficient is displayed individually, for a circle centered at $(-120\text{ mm},\ 0)$. The phase angle of the $2n$-pole term is computed with the A_n and B_n retrieved from the A_z expansion, as shown in Table 6.1. As we can see, results coincide with Fig. 6.31, where the field of the 6-pole term is rotated by approximately π radiants.

n	B_n	A_n	ψ_n
1	0.97569	-0.00016399	-0.00016807
2	0.027813	0.0005639	0.020272
3	-0.043832	-0.00071705	-3.1252
4	0.034081	0.00030532	0.0089584

Table 6.1: Computation of the phase angle ψ for the lower harmonic orders.

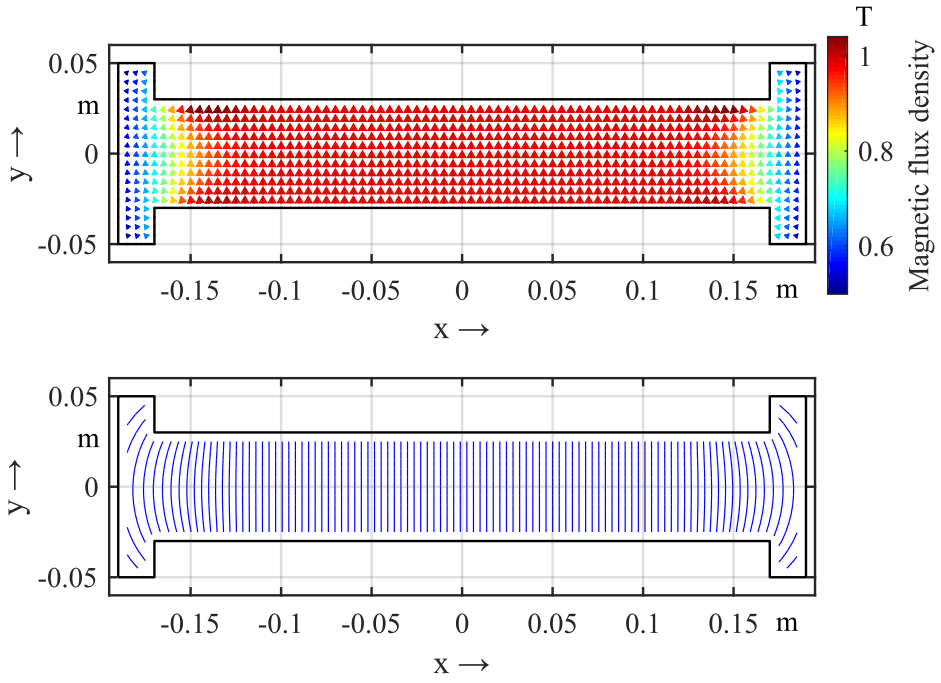

Figure 6.22: Top: Magnetic field map from the BEM reconstruction. Absolute value and direction of the field are obtained as combination of the two Cartesian components reconstructed individually. Bottom: Field lines obtained as equipotentials of A_z.

6.9 Comparison with orthogonal expansion

For a rectangular geometry also an analytic solution based on the separation of variables method is available (see Appendix B). This solution requires the Fourier series expansion of the Dirichlet data over the four sides of the rectangle, where, from the Fourier coefficients, the coefficients of the expansion in eigenfunctions are retrieved. The solution of the Laplace equation inside the bounded domain, for the magnetic vector potential A_z, is written as the sum of four terms obtained from the Fourier series expansion of the boundary data over each single side of the rectangle

$$A_z(x,y) = \sum_{k=1}^{4} A_z^{(k)}(x,y) \ . \tag{6.23}$$

For example, the term corresponding to the side $x_1 \leq x \leq x_2$ and $y = y_1$, where $x_1 = -190$ mm, $x_2 = 190$ mm and $y_1 = -30$ mm reads as

$$A_z^{(1)}(x,y) = \sum_{n=1}^{+\infty} \mathcal{M}_n^{(1)} \sinh\left(n\pi \frac{y_2 - y}{x_2 - x_1}\right) \sin\left(n\pi \frac{x - x_1}{x_2 - x_1}\right) \ , \tag{6.24}$$

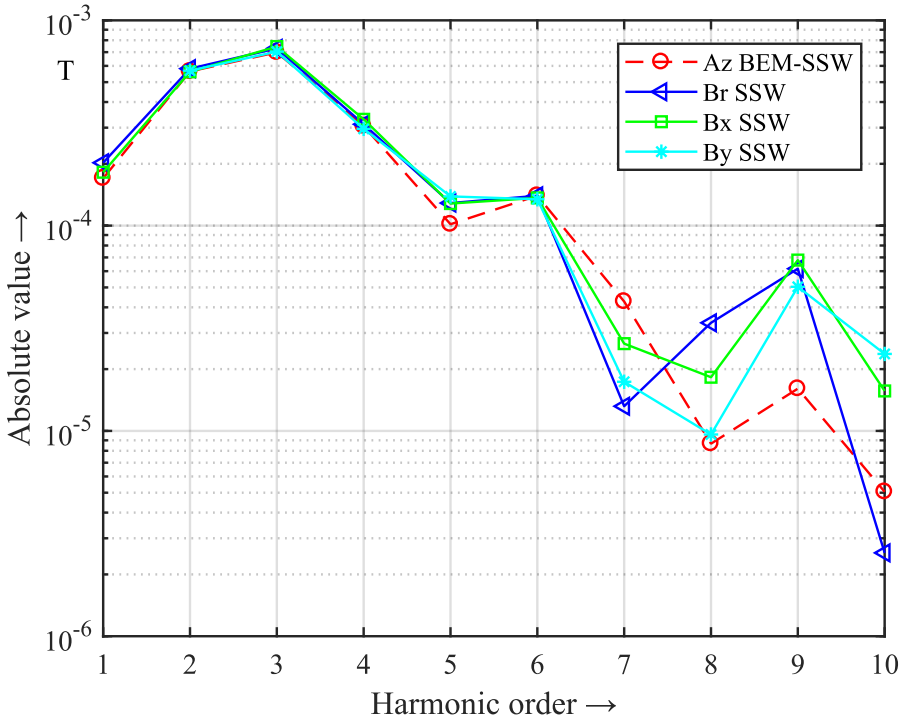

Figure 6.23: Comparison between Skew multipole coefficients A_n as function of the harmonic order n. A number of samples $N = 32$ have been acquired over a circumference with radius $r_0 = 30$ mm centered in $(-120\text{ mm},\ 0)$. Absolute values are computed until the 10-th harmonic order.

where $y_2 = 30$ mm and $\mathcal{M}_n^{(1)}$ is the n-th Fourier sine coefficient defined as

$$\mathcal{M}_n^{(1)} = \frac{\mathcal{A}_n^{(1)}}{\sinh\left(n\pi\dfrac{y_2 - y_1}{x_2 - x_1}\right)}\ , \tag{6.25}$$

with

$$\mathcal{A}_n^{(1)} = \frac{2}{x_2 - x_1}\int_{x_1}^{x_2} A_z^{(1)}(x, y_1)\sin\left(n\pi\frac{x - x_1}{x_2 - x_1}\right)dx\ . \tag{6.26}$$

The numerical computation of $\mathcal{A}_n^{(1)}$ is performed by the Discrete Fourier Transform applied to the N equally spaced samples of the function $A_z^{(1)}(x, y_1)$ in $x_1 \le x \le x_2$. In order to satisfy the sampling theorem, the maximum harmonic order that can be employed is $(N - 1)$. Since a different number of samples is available for horizontal and vertical sides, that is N=77 and N=13 respectively, the associated expansion are limited to different harmonic orders. We investigate the correctness of the sampling theorem considering different limits for the magnetic vector poten-

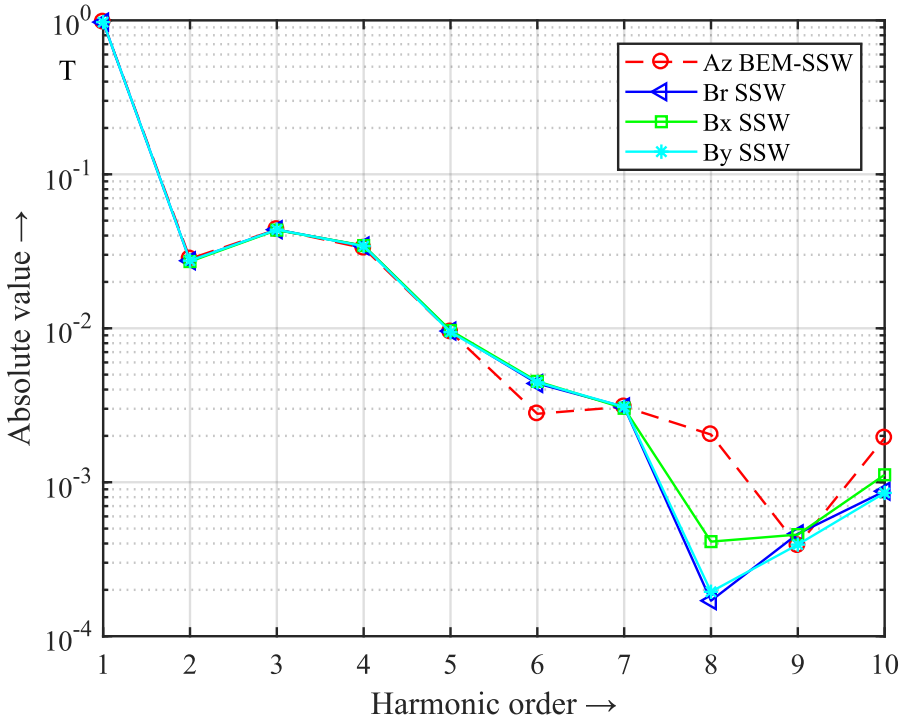

Figure 6.24: Comparison between Normal multipole coefficients B_n as function of the harmonic order n. A number of samples $N = 32$ have been acquired over a circumference with radius $r_0 = 30$ mm centered in $(-120 \text{ mm}, 0)$. Absolute values are computed until the 10-th harmonic order.

tial expansion along the entire boundary. The parameter h is introduced for the calculation of the employed maximum harmonic order $\bar{n}$ as

$$\bar{n}_i = h \cdot \frac{N_i - 1}{4} \ , \tag{6.27}$$

where i=1 for the horizontal sides and i=2 for the vertical ones. Table 6.2 shows the relations for h=1, 2, 4 and 6. Fig. 6.32 compares the MVP, defined over the rectangular boundary, with its orthogonal expansions for different levels characterized by h.

We define the L^2 error norm as

$$\|e\|_{L^2} = \sqrt{\sum_{p=1}^{P} \left| A_z^{(k)} - A_z'^{(k)} \right|^2} \ , \tag{6.28}$$

where A_z is the expansion of the boundary data A_z' over the contour; it is computed in order to evaluate the convergence of the error and, consequently, verify the

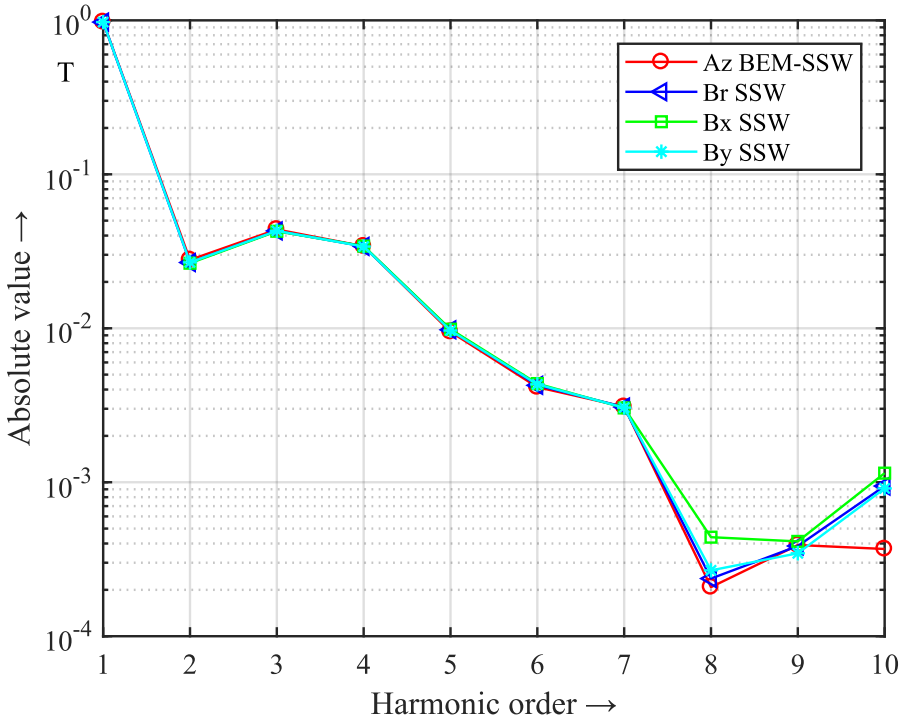

Figure 6.25: Comparison between Normal multipole coefficients B_n as function of the harmonic order n. A number of samples $N = 64$ have been acquired over a circumference with radius $r_0 = 30$ mm centered in $(-120$ mm, $0)$. Absolute values are computed until the 10-th harmonic order.

correctness of the sampling theorem. The results shown in Fig. 6.33 confirm that the best solution is obtained when $N - 1$ Fourier coefficients are employed. For this reason, the following evaluation is performed for the expansion represented in Fig. 6.34.

The solution $A_z(x, y)$ is now computed inside the interested domain. In Fig. 6.14 the magnetic fluxes, crossing y-oriented surfaces with area equal to 10 mm x 1m, are computed as differences of A_z. The MVP values have been retrieved at the extremities of elements with length 10 mm lying on the central line $\{-180$ mm $\leq x \leq +180$ mm$, y = 0\}$. The comparison shows that BEM can be still considered the best exploitable solution. The field quality representation in Fig. 6.35 confirms that the domain reconstruction is affected by a sort of wave propagation that derives from the expansion of the function on the four sides.

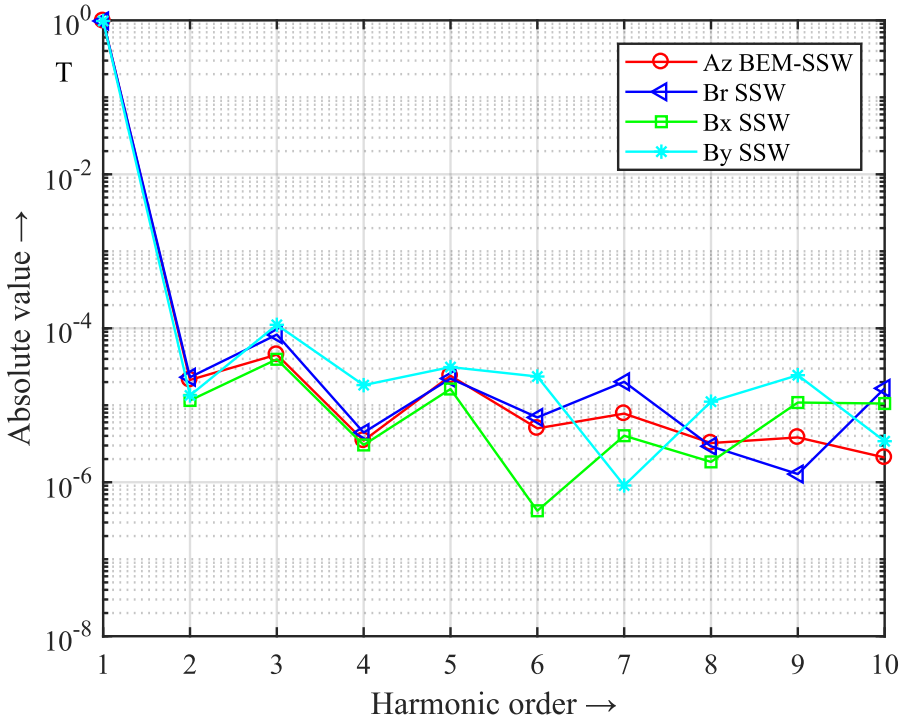

Figure 6.26: Comparison between Normal multipole coefficients B_n as function of the harmonic order n. A number of samples $N = 64$ have been acquired over a circumference with radius $r_0 = 30$ mm centered in $(0,\ 0)$. Absolute values are computed until the 10-th harmonic order.

6.10 Implementation of Galerkin BEM

Collocation BEM results, for linear elements, are now compared with the alternative method presented in Chapter 3, namely, the Galerkin BEM. Fig. 6.36 compares the tangential component of the integrated field measured and reconstructed by BEM, as Neumann data, at the P nodes of the boundary. Galerkin BEM results much more regular than collocation BEM on the vertical sides, but at the same time it shows a displacement of the values at the nodes. Fig. 6.37 shows a good agreement of both BEM method compared to measured data.

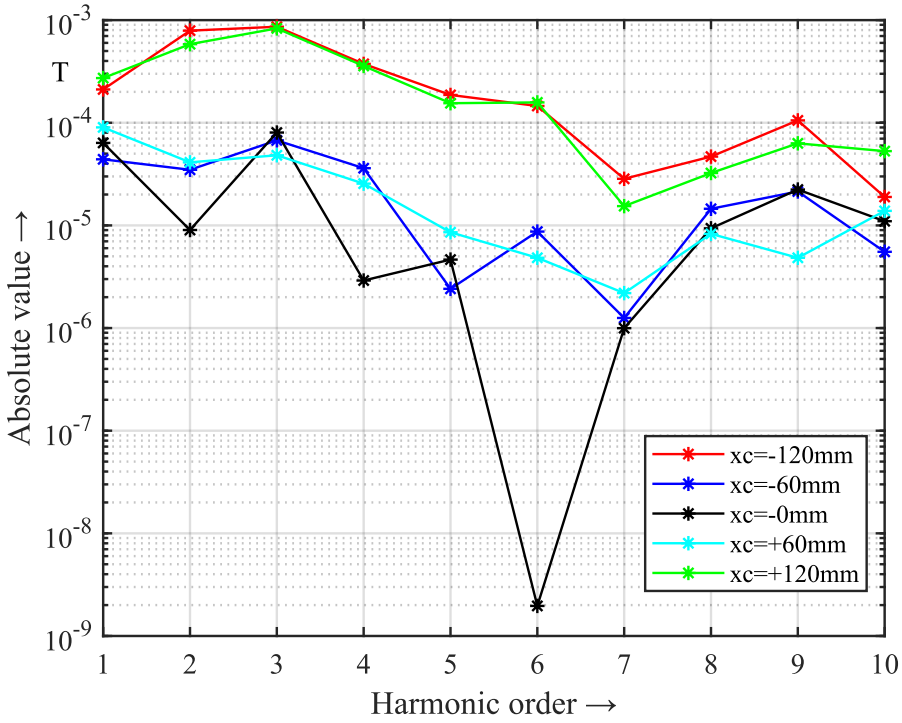

Figure 6.27: Comparison between Skew multipole coefficients A_n as function of the harmonic order n. A number of samples $N = 64$ have been acquired over a circumference with radius $r_0 = 30$ mm centered in five different positions $(x_c,\ 0)$. Absolute values are computed from the expansion of the field component B_x, until the 10-th harmonic order.

h	1	2	4	6
$\bar{n}_1$	19	38	76	114
$\bar{n}_2$	3	6	12	18

Table 6.2: Relation between the parameter h and the value of the employed maximum harmonic orders $\bar{n}_1$ and $\bar{n}_2$.

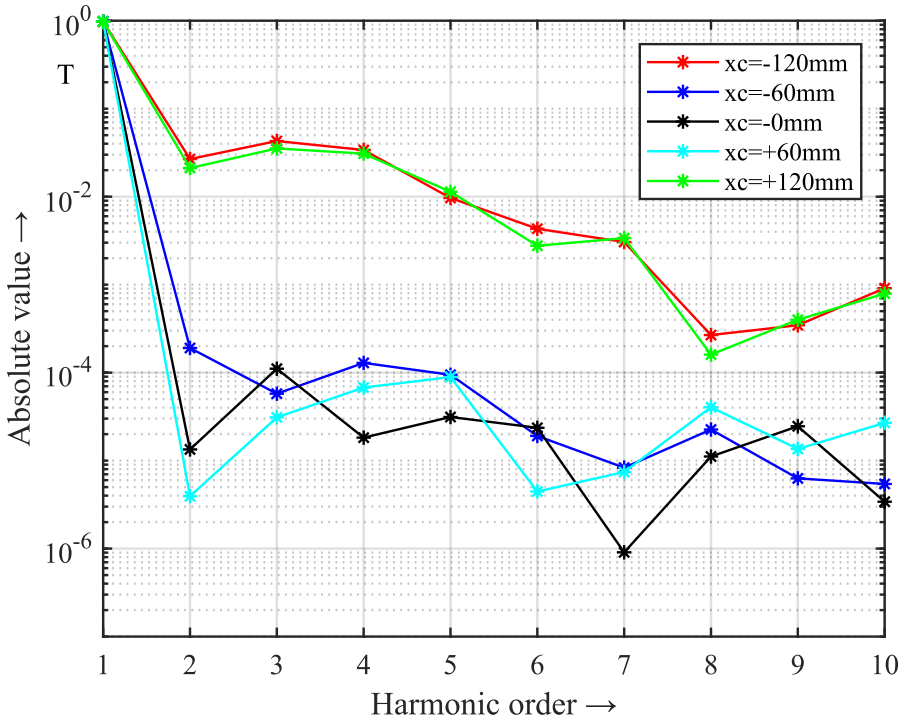

Figure 6.28: Comparison between Normal multipole coefficients B_n as function of the harmonic order n. A number of samples $N = 64$ have been acquired over a circumference with radius $r_0 = 30$ mm centered in five different positions $(x_c,\ 0)$. Absolute values are computed from the expansion of the field component B_y, until the 10-th harmonic order.

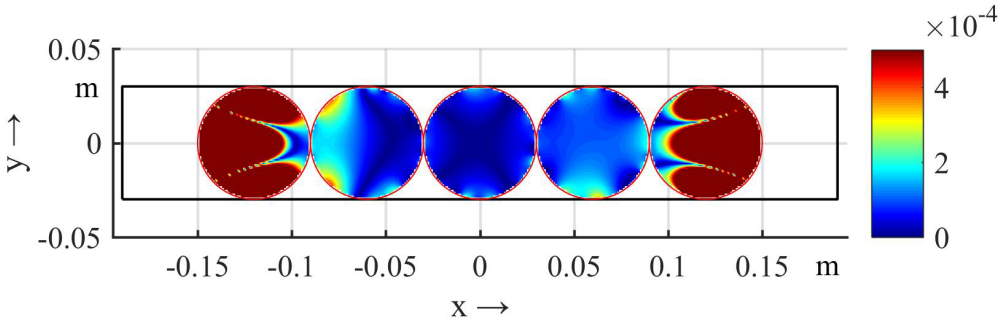

Figure 6.29: Field quality representation of the y component from five distinct measurements on circular domains inside the magnet aperture.

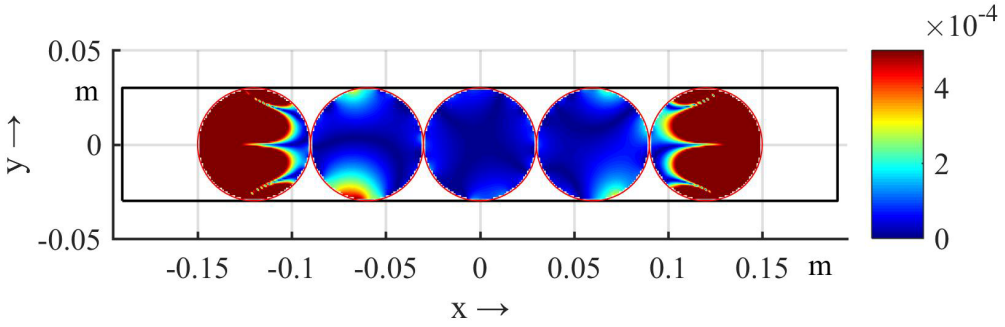

Figure 6.30: Field quality representation of the x component from five distinct measurements on circular domains inside the magnet aperture.

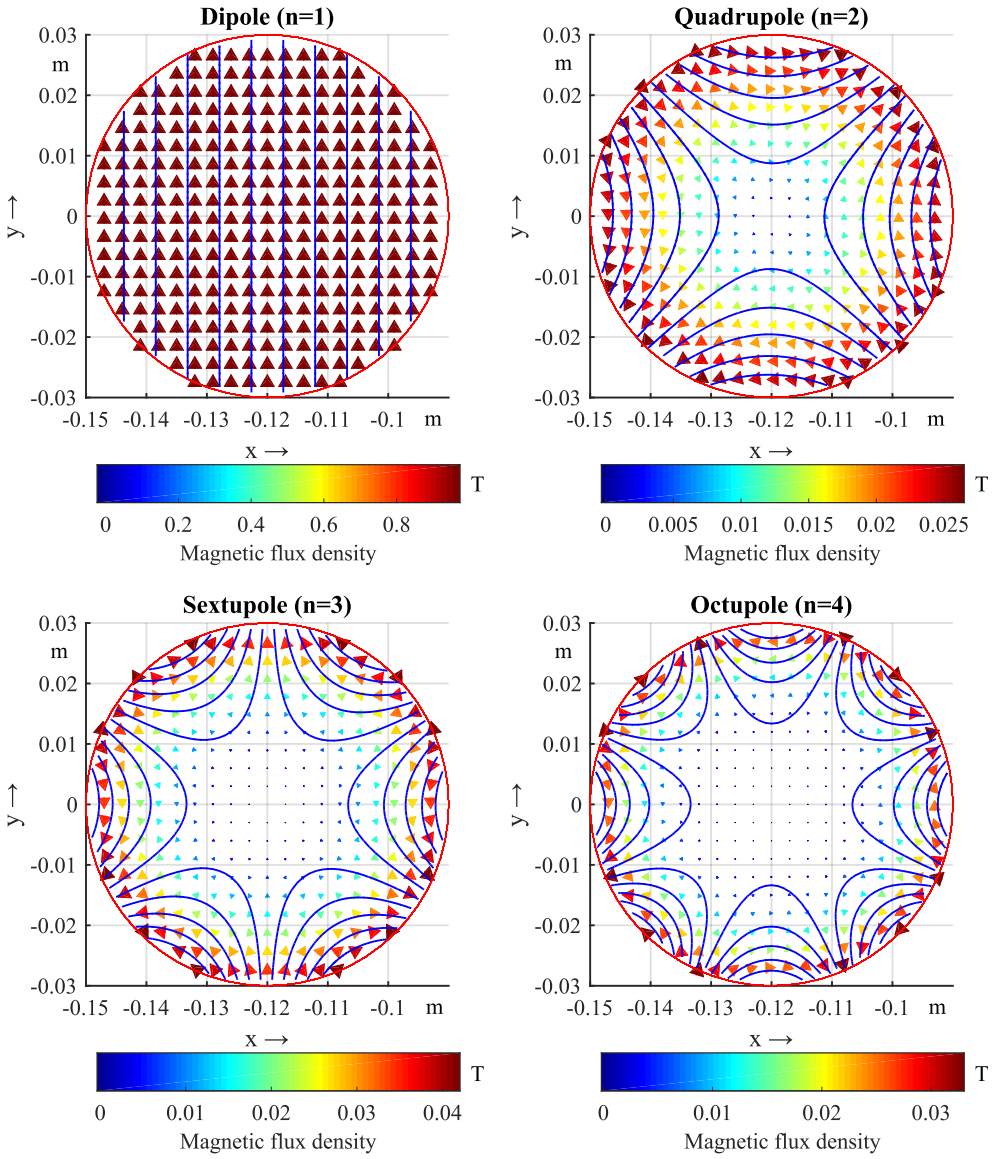

Figure 6.31: Magnetic field **B** maps and equipotential lines reconstructed from the first four coefficients of Fig. 6.25 separately. Arrows size and color are proportional to the Magnetic field absolute value.

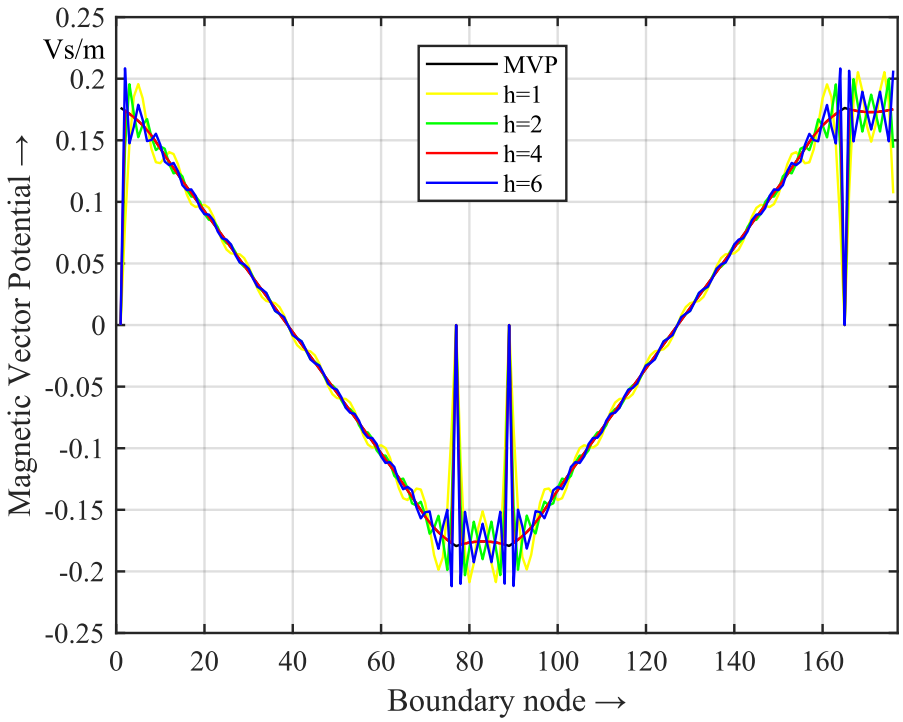

Figure 6.32: Expansion of A_z, over the boundary, as a function of h.

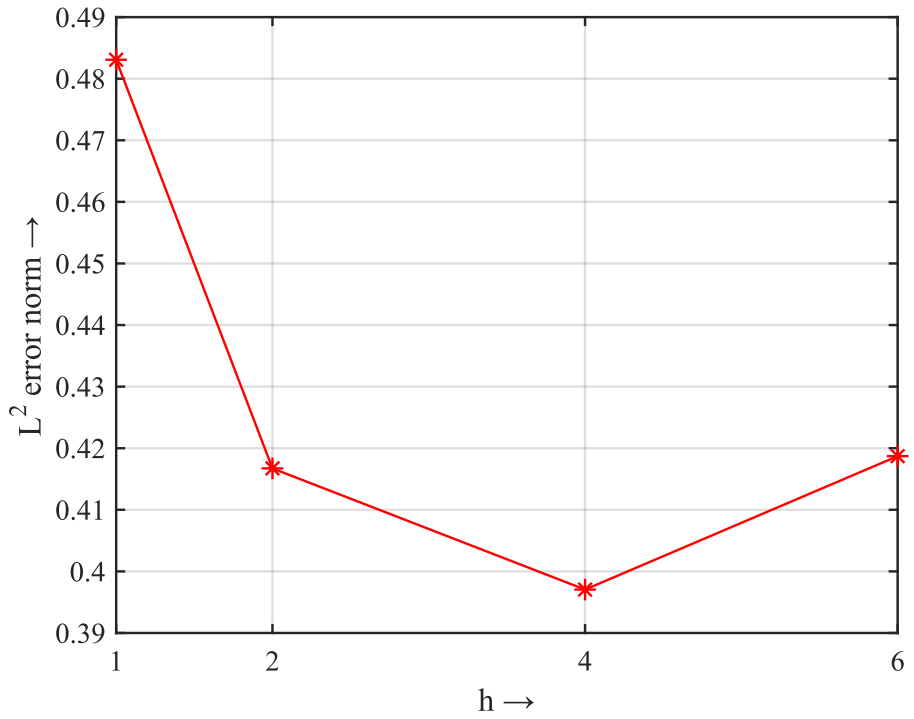

Figure 6.33: L^2 error norm as a function of h.

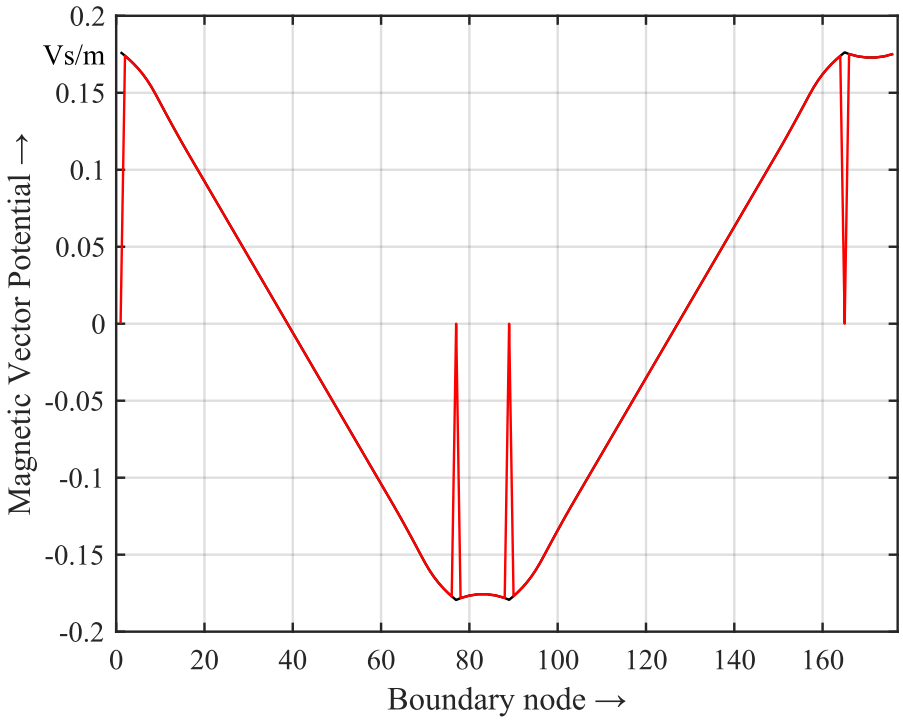

Figure 6.34: Expansion of A_z using $N-1$ Fourier coefficients for each of the four sides.

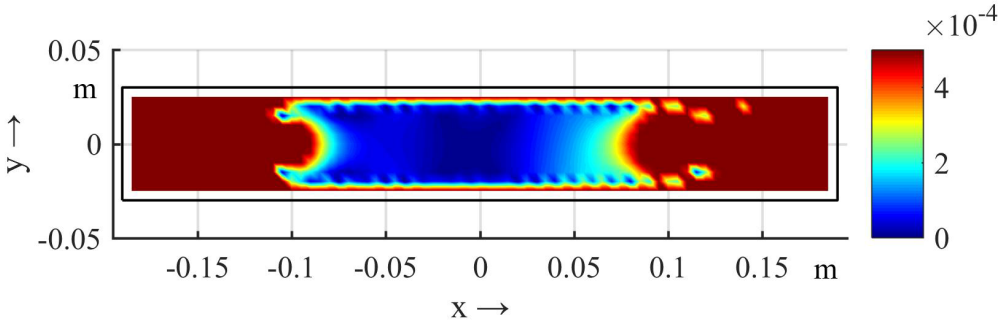

Figure 6.35: Field quality representation for the y component of the field $\mathbf{B}$.

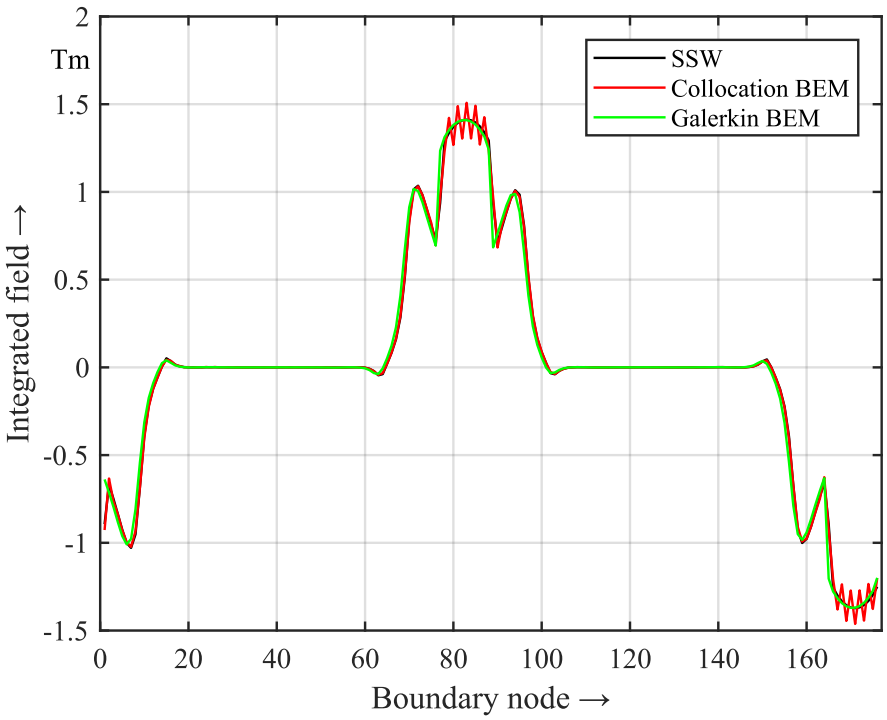

Figure 6.36: Tangential component of the integrated field measured (SSW) and reconstructed by BEM, with two different methods, at the nodes of the boundary.

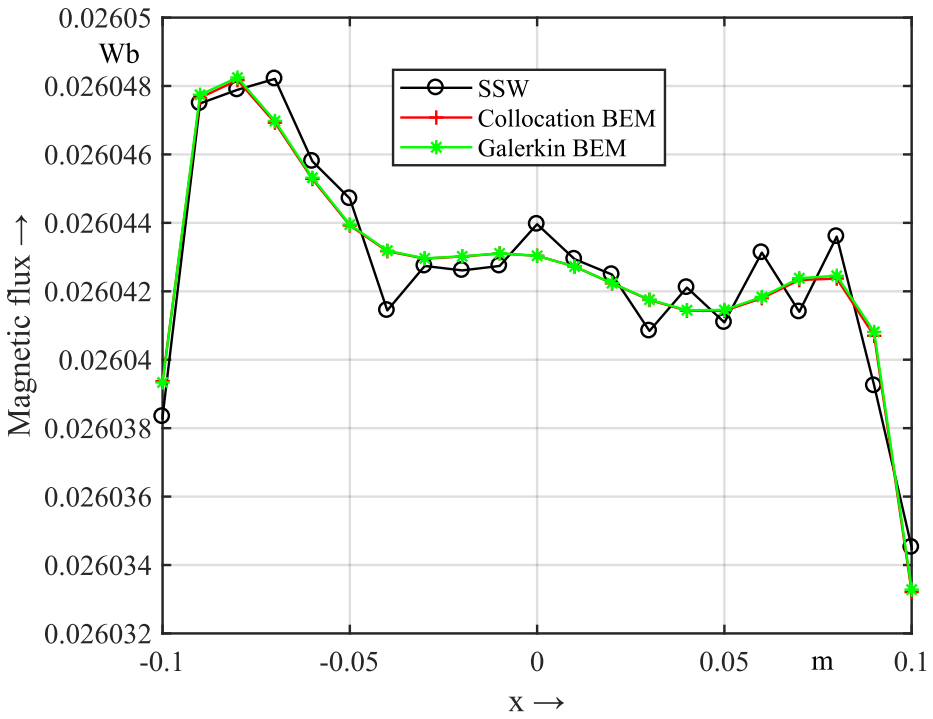

Figure 6.37: Magnetic flux measured (SSW) and reconstructed by BEM, with two different methods, along the central line $y = 0$.

Conclusions

The presented method overcomes the limits imposed by the standard rotating coil device when the integrated magnetic field is reconstructed in apertures with large aspect ratio. This alternative technique is not bounded by particular trajectories. In fact, the boundary can have any continuous shape that best fits the magnet aperture and its fringe field regions too.

The technique is based on the boundary integral equation method in two dimensions, which allows the computation of solutions of boundary value problems in bounded domains by reducing the dimensionality of the problem from $\mathbb{R}^2$ to $\mathbb{R}$.

The numerical implementation is possible by means of the collocation boundary element method (BEM). A dedicated MATLAB® code has been developed for both linear and quadratic elements. The code was successfully validated through a test problem and then implemented for simulated and measured boundary data. The analysis performed with ROXIE simulated data at different levels of discretization shows the convergence rate of the method. The comparison with the Galerkin BEM proves the advantage of the collocation method for this application.

Single-stretched-wire measurements are fluxes out-normal to the boundary, subsequently post-processed in order to retrieve magnetic vector potential values at the BEM nodes. These values are Dirichlet boundary conditions for the boundary value problem. Starting form this considerations, flux values have been reconstructed at internal points, showing a good agreement with respect to the measured values. Since the BEM uses all boundary data for the reconstruction of a single field value within the domain, the method is robust with respect to the measurements uncertainties.

A systematic comparison has been carried out between the results obtained by the new BEM approach and those derived from the field harmonics theory and the expansion in orthogonal eigenfunctions.

Regarding the development of the MATLAB® BEM code, there is still room for improvements. One could extend the study, for example, to a priori error estimations, and consequently develop an adaptive scheme in order to optimize the accuracy with permissible computation time.

The final purpose of this work was the development of the new post-processing

technique for the stretched wire system. The goal has been successfully achieved with the installation of the BEM software directly on the measurement system available in the section's lab. It will be routinely used for measurements in magnets apertures. This will save time during the acquisition process and will be an useful tool for validating measured data.

Bibliography

[1] How an accelerator works. https://home.cern/about/how-accelerator-works.

[2] The large hadron collider. https://home.cern/topics/large-hadron-collider.

[3] S. Russenschuck. *Field Computation for Accelerator Magnets*. WILEY-VCH, 2010.

[4] Te-msc-mm. https://te-msc-mm.web.cern.ch/.

[5] J.T. Katsikadelis. *The Boundary Element Method for Engineers and Scientists*. ELSEVIER, 2016.

[6] M. Costabel. *Principles of Boundary Element Methods*. Technische Hochschule Darmstadt.

[7] A. Keng-Cheng. Introducing the boundary element method with matlab. *International Journal of Mathematical Education in Science and Technology*, 2008.

[8] G. Beer, I. Smith, and C. Duenser. *The Boundary Element Method with Programming*. Springer, 2008.

[9] W.S. Hall. *The Boundary Element Method*. Springer, 1994.

[10] Hilbert (release 3): A matlab implementation of adaptive bem. http://www.asc.tuwien.ac.at/abem/hilbert/.

[11] S. Russenschuck. Roxie: A computer code for the integrated design of accelerator magnets. 2018.

[12] C. Petrone. *Wire Methods for Measuring Field Harmonics, Gradients and Magnetic Axes in Accelerator Magnets*. Ph.d thesis, University of Sannio, Benevento, Italy, 2013.

[13] L. Walckiers. Harmonic coils. *CERN Accelerator School on Magnetic Measurements and Alignment*, 1992.

[14] R.C. Daileda. *The Dirichlet Problem on a Rectangle*. Trinity University.

[15] J.O. Smith III. *Mathematics of the Discrete Fourier Transform (DFT)*. 2007.

[16] W.H. Hayt Jr and J.A. Buck. *Engineering Electromagnetics*. McGraw-Hill, 2012.

[17] B.B. Laud. *Electromagnetics*. NEW AGE, 2005.

Appendix A

Field Harmonics

The field quality in accelerator magnets is conveniently described by a set of Fourier coefficients, known as field harmonics or multipole coefficients. The method used for the calculation of field harmonics is based on finding a general solution that satisfies the Laplace equation in a suitable coordinate system. The integration constants in the general solution, obtained with the separation of variables technique, are then determined by comparison with the boundary values; in 2D circular coordinates these boundary values are given by the field components at a given reference radius.

A.1 Determining multipole coefficients

There are 3 different approaches to the calculation of these coefficients [3]:

- Fourier series expansion of the calculated field component along a circle;
- In the case of an up/down symmetry, comparison of the multipole coefficients with the Taylor coefficients of a series expansion of the known flux density at the horizontal median plane;
- Series expansion of the Green kernel in the potentials generated by transport and magnetization currents, and comparison of the coefficients with the multipoles.

The first approach is developed and used here, since it is the one that fits better the case under study.

A.2 Fourier series expansion of field components

The Fourier series expansion of a function $f = f(\varphi)$, defined over a circle with reference radius r_0, is developed as

$$f(r_0, \varphi) = \frac{C_0(r_0)}{2} + \sum_{n=1}^{\infty} \left[C_n(r_0) \sin(n\varphi) + D_n(r_0) \cos(n\varphi) \right] . \tag{A.1}$$

The Fourier series coefficients in (A.1) are computed as

$$C_0(r_0) = \frac{2}{2\pi} \int_0^{2\pi} f(r_0, \varphi) d\varphi , \tag{A.2}$$

$$C_n(r_0) = \frac{2}{2\pi} \int_0^{2\pi} f(r_0, \varphi) \sin(n\varphi) d\varphi , \tag{A.3}$$

$$D_n(r_0) = \frac{2}{2\pi} \int_0^{2\pi} f(r_0, \varphi) \cos(n\varphi) d\varphi . \tag{A.4}$$

In our practical applications, the function f is a generic field component B, which is measured, or computed, at N equally spaced points in the interval $[0, 2\pi)$; thus, the angle φ assumes the form

$$\varphi_k = \frac{2\pi}{N} k \quad k = 0, 1, 2, 3 \ldots N - 1 . \tag{A.5}$$

By means of the Discrete Fourier Transform, is then possible to compute the set of Fourier coefficients as

$$C_0(r_0) \approx \frac{2}{N} \sum_{k=0}^{N-1} B(r_0, \varphi_k) , \tag{A.6}$$

$$C_n(r_0) \approx \frac{2}{N} \sum_{k=0}^{N-1} B(r_0, \varphi_k) \sin(n\varphi_k) , \tag{A.7}$$

$$D_n(r_0) \approx \frac{2}{N} \sum_{k=0}^{N-1} B(r_0, \varphi_k) \cos(n\varphi_k) . \tag{A.8}$$

The definition (A.1) translates into

$$B(r_0, \varphi_k) = \frac{C_0(r_0)}{2} + \sum_{n=1}^{\infty} \left[C_n(r_0) \sin(n\varphi_k) + D_n(r_0) \cos(n\varphi_k) \right] , \tag{A.9}$$

where each integer value n corresponds to a specific flux distribution generated by ideal magnet geometries ($n = 1$ dipole, $n = 2$ quadrupole, $n = 3$ sextupole...).

Since only N equally spaced points are available over the circle, the maximum harmonic order is limited at $N-1$. This forced approximation introduces unavoidably an error ε

$$\varepsilon(\varphi_k) = B(r_0, \varphi_k) - \left[\frac{C_0(r_0)}{2} + \sum_{n=1}^{N-1} \left[C_n(r_0)\sin(n\varphi_k) + D_n(r_0)\cos(n\varphi_k) \right] \right] . \quad \text{(A.10)}$$

It is worth noting that the same considerations valid for the field expansion, hold also for the magnetic vector potential A_z.

A.3 Normal and Skew multipole coefficients

Once the Fourier series coefficients have been computed from the samples available over the circle, it is possible to retrieve the multipole coefficients according to Tab. A.1, where B_n is the Normal multipole coefficient and A_n is the Skew multipole

	B_r	B_φ	B_x	B_y	A_z
B_n	C_n	D_n	C_{n-1}	D_{n-1}	$-\frac{n}{r_0}D_n$
A_n	D_n	$-C_n$	D_{n-1}	$-C_{n-1}$	$\frac{n}{r_0}C_n$

Table A.1: Relations between the Multipole and the Fourier coefficients.

coefficient. These coefficients are, by definition, given in units of Tesla. However, it is common practice to normalize them with respect to the main field component $B_N(r_0)$, which yields to dimensionless relative multipole coefficients

$$a_n = \frac{A_n}{B_N} , \quad \text{(A.11)}$$

$$b_n = \frac{B_n}{B_N} . \quad \text{(A.12)}$$

The field components and the vector potential can now be expressed as a function of the multipoles computed at the reference radius. Moreover, it is possible to retrieve the values at any radius in the bounded circular domain thanks to the

following relations

$$B_r(r,\varphi) = \sum_{n=1}^{\infty} \left(\frac{r}{r_0}\right)^{n-1} \left(B_n(r_0)\sin(n\varphi) + A_n(r_0)\cos(n\varphi)\right) , \tag{A.13}$$

$$B_\varphi(r,\varphi) = \sum_{n=1}^{\infty} \left(\frac{r}{r_0}\right)^{n-1} \left(B_n(r_0)\cos(n\varphi) - A_n(r_0)\sin(n\varphi)\right) , \tag{A.14}$$

$$B_x(r,\varphi) = \sum_{n=1}^{\infty} \left(\frac{r}{r_0}\right)^{n-1} \left(B_n(r_0)\sin(n-1)\varphi + A_n(r_0)\cos(n-1)\varphi\right) , \tag{A.15}$$

$$B_y(r,\varphi) = \sum_{n=1}^{\infty} \left(\frac{r}{r_0}\right)^{n-1} \left(B_n(r_0)\cos(n-1)\varphi - A_n(r_0)\sin(n-1)\varphi\right) , \tag{A.16}$$

$$A_z(r,\varphi) = -\sum_{n=1}^{\infty} \frac{r_0}{n}\left(\frac{r}{r_0}\right)^{n} \left(B_n(r_0)\cos(n\varphi) - A_n(r_0)\sin(n\varphi)\right) . \tag{A.17}$$

An important parameter that is derived from multipole coefficients is the phase angle of the $2n$-pole term, defined as

$$\psi_n = \begin{cases} \arctan\dfrac{A_n}{B_n} & \text{if } B_n \geq 0 \\ \arctan\dfrac{A_n}{B_n} + \pi & \text{if } B_n < 0 \text{ and } A_n \geq 0 \\ \arctan\dfrac{A_n}{B_n} - \pi & \text{if } B_n < 0 \text{ and } A_n < 0 \end{cases} . \tag{A.18}$$

A.4 Complex representation and Feed-down effect

The solution in Cartesian coordinates could be also obtained from the following transformation

$$B_x = B_r\cos\varphi - B_\varphi\sin\varphi , \tag{A.19}$$

$$B_y = B_r\sin\varphi + B_\varphi\cos\varphi , \tag{A.20}$$

which reads in complex notation

$$B_y + iB_x = (B_\varphi + iB_r)e^{-i\varphi} , \tag{A.21}$$

for $z = x + iy$

$$\begin{aligned} B_y + iB_x &= \sum_{n=1}^{\infty} \left(B_n(r_0) + iA_n(r_0)\right)\left(\frac{r}{r_0}\right)^{n-1} e^{i(n-1)\varphi} \\ &= \sum_{n=1}^{\infty} \left(B_n(r_0) + iA_n(r_0)\right)\left(\frac{z}{r_0}\right)^{n-1} . \end{aligned} \tag{A.22}$$

This formulation is useful when, in the post processing, the misalignment of the measurement axis and the real magnet axis has to be identified. This off centering of the set of measurements is called feed down effect, and can be analytically described starting from the last complex representation [3]. The transformation law for the field harmonics can be derived for a translation of the measurements reference, relying on the fact that the field components in both the coordinate systems must be identical

$$B_y + iB_x = B'_y + iB'_x \ . \tag{A.23}$$

This fact leads to

$$\sum_{n=1}^{\infty} C_n \left(\frac{z}{r_0}\right)^{n-1} = \sum_{n=1}^{\infty} C'_n \left(\frac{z'}{r_0}\right)^{n-1} \ , \tag{A.24}$$

where the complex coefficients in the two different reference systems

$$\begin{aligned} C_n &= B_n + iA_n \ , \\ C'_n &= B'_n + iA'_n \ , \end{aligned}$$

while the relation between the coordinates

$$\begin{aligned} z &= x + iy \ , \\ z_d &= x_d + iy_d \ , \\ z' &= z - z_d \ . \end{aligned}$$

Results the transformation law for the complex field harmonics

$$C'_n = \sum_{k=n}^{\infty} C_k \binom{k-1}{n-1} \left(\frac{z_d}{r_0}\right)^{k-n} \ . \tag{A.25}$$

If (A.25) is solved for $n = 1$ (first order feed down effect) and until the 3^{rd} harmonic order, results the system of equations

$$\begin{cases} B'_1 = B_1 + \dfrac{1}{r_0} B_2 x_d - \dfrac{1}{r_0} A_2 y_d + \dfrac{1}{r_0^2} B_3 x_d^2 - \dfrac{1}{r_0^2} B_3 y_d^2 - \dfrac{2}{r_0^2} A_3 x_d y_d \\ \\ A'_1 = A_1 + \dfrac{1}{r_0} B_2 y_d + \dfrac{1}{r_0} A_2 x_d + \dfrac{1}{r_0^2} A_3 x_d^2 - \dfrac{1}{r_0^2} A_3 y_d^2 + \dfrac{2}{r_0^2} B_3 x_d y_d \end{cases} \ , \tag{A.26}$$

whose solutions x_d and y_d allows to deduce the displacement between the two references. From the previous system of equations, it is possible to evaluate which field components arises due to the measurement off-centering.

Appendix A

Appendix B

Solution of the Laplace Equation with Eigenfunction Expansion

The solution of boundary value problems (bvp), with Dirichlet boundary conditions fixed over a rectangular boundary, can be developed in terms of Fourier series expansion [14]. This evaluation could be an alternative solution of the boundary integral equation method, and for this reason it is useful to compare the numerical implementation of the two methods in order to estimate which one fits better the case under study.

B.1 The Dirichlet problem

In mathematics, a Dirichlet problem is the problem of finding a function which solves a specified partial differential equation (PDE) in the interior of a given region that takes prescribed values on the boundary of that region. In an equivalent way, it is a problem of finding the connection between a continuous function $f(x, y)$, defined over the boundary ∂R of a region $R \subseteq \mathbb{R}$, with an harmonic function $u(x, y)$ taking on the value $f(x, y)$ on ∂R

$$\begin{aligned} \nabla^2 u = 0 \quad &\text{inside } R \ , \\ u(x, y) = f(x, y) \quad &\text{on } \partial R \ . \end{aligned}$$

In the following we consider a rectangular region $\{x_1 \leq x \leq x_2 \ , \ y_1 \leq y \leq y_2\}$ where the boundary conditions are given on each edge separately, as shown in Fig. B.1

$$\begin{aligned} u(x, y_1) &= f_1(x) \ , \\ u(x, y_2) &= f_2(x) \ , \\ u(x_1, y) &= g_1(y) \ , \\ u(x_2, y) &= g_2(y) \ . \end{aligned}$$

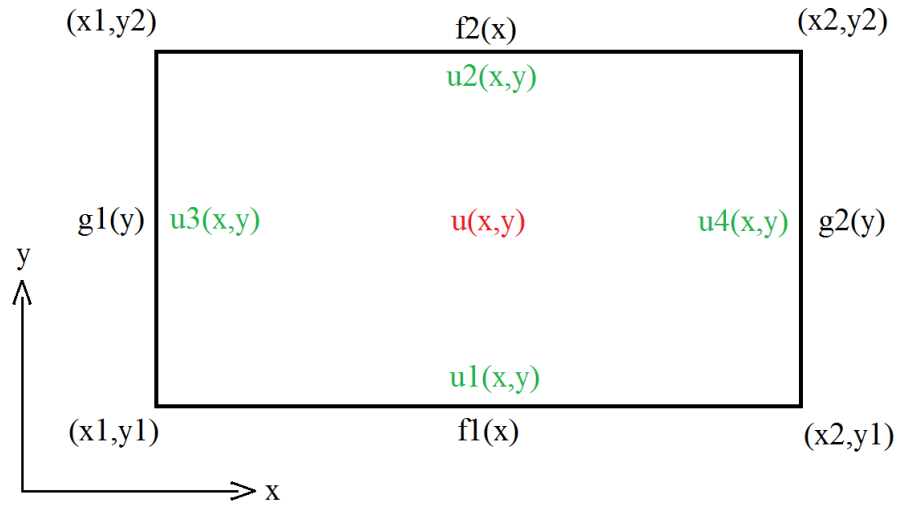

Figure B.1: Dirichlet boundary value problem for the rectangular region. Boundary conditions are fixed on each edge separately.

By the principle of superposition, the final solution of the bvp can be written as the sum of the solutions of four simpler problems

$$u(x,y) = u_1(x,y) + u_2(x,y) + u_3(x,y) + u_4(x,y) \ , \tag{B.1}$$

where each term satisfies the PDE with one of the original non-homogeneous boundary condition and the homogeneous version of the remaining three boundary conditions [14].

B.1.1 Example

The bvp with boundary conditions

$$\begin{aligned} u(x,y_1) &= 0 \ , \\ u(x,y_2) &= f_2(x) \ , \\ u(x_1,y) &= 0 \ , \\ u(x_2,y) &= 0 \ , \end{aligned}$$

is solved with the method of separations of variables. Setting $u(x,y) = X(x) \cdot Y(y)$ we get

$$\begin{aligned} X'' + kX &= 0 \ , \\ Y'' - kY &= 0 \ , \\ X(x_1) = X(x_2) &= 0 \ , \\ Y(y_1) &= 0 \ . \end{aligned}$$

Knowing that the non-trivial solutions for X are given by

$$X(x) = X_n x = \sin[\mu_n(x - x_1)] \ ,$$

where $\mu_n = \dfrac{n\pi}{x_2 - x_1}$ and $k = \mu_n^2$ with $n \in \mathbb{N}$. The hyperbolic cosine and sine functions are defined as

$$\cosh y = \frac{e^y + e^{-y}}{2} \ ,$$
$$\sinh y = \frac{e^y - e^{-y}}{2} \ ,$$

and they satisfy the following identities

$$\cosh^2 y - \sinh^2 y = 1 \ ,$$
$$\frac{d}{dy}\cosh y = \sinh y \ ,$$
$$\frac{d}{dy}\sinh y = \cosh y \ .$$

It follows that the general solution to the Ordinary Differential Equation (ODE) $Y'' - \mu_n^2 Y = 0$ is

$$Y = A\cosh[\mu(y - y_1)] + B\sinh[\mu(y - y_1)] \ ,$$

Using $\mu = \mu_n$ and $Y(y_1) = 0$, we find

$$Y(y) = Y_n(y) = A_n\cosh[\mu_n(y - y_1)] + B\sinh[\mu_n(y - y_1)] \ ,$$
$$0 = Y_n(y_1) = A_n\cosh 0 + B_n\sinh 0 = A_n \ ,$$

yields the separated solutions

$$u_n(x, y) = X_n(x)Y_n(y) = B_n\sin[\mu_n(x - x_1)]\sinh[\mu_n(y - y_1)] \ ,$$

that combine in the general solution

$$u(x, y) = \sum_{n=1}^{\infty} B_n\sin[\mu_n(x - x_1)]\sinh[\mu_n(y - y_1)] \ .$$

Finally, applying the Dirichlet boundary condition $f_2(x)$ at the top edge $y = y_2$

$$f_2(x) = u(x, y_2) = \sum_{n=1}^{\infty} B_n\sin[\mu_n(x - x_1)]\sinh[\mu_n(y_2 - y_1)] \ ,$$

where B_n is a multiple of the sine series coefficient B'_n, computed as

$$B'_n = \frac{2}{(x_2 - x_1)}\int_{x_1}^{x_2} f_2(x)\sin[\mu_n(x - x_1)]dx \ ,$$

$$B_n = \frac{1}{\sinh[\mu_n(y_2 - y_1)]}B'_n \ .$$

B.1.2 The overall solution

The procedure shown in Section B.1.1 is applied for all the edges of the rectangular boundary, leading to the following system of equations

$$u_1(x,y) = \sum_{n=1}^{\infty} A_n \sin\left(n\pi \frac{x-x_1}{x_2-x_1}\right) \sinh\left(n\pi \frac{y_2-y}{x_2-x_1}\right) , \tag{B.2}$$

$$u_2(x,y) = \sum_{n=1}^{\infty} B_n \sin\left(n\pi \frac{x-x_1}{x_2-x_1}\right) \sinh\left(n\pi \frac{y-y_1}{x_2-x_1}\right) , \tag{B.3}$$

$$u_3(x,y) = \sum_{n=1}^{\infty} C_n \sin\left(n\pi \frac{y-y_1}{y_2-y_1}\right) \sinh\left(n\pi \frac{x_2-x}{y_2-y_1}\right) , \tag{B.4}$$

$$u_4(x,y) = \sum_{n=1}^{\infty} D_n \sin\left(n\pi \frac{y-y_1}{y_2-y_1}\right) \sinh\left(n\pi \frac{x-x_1}{y_2-y_1}\right) . \tag{B.5}$$

In each case, the coefficients of the solution are independent of the others, and are just multiples of the Fourier sine coefficients of the non-zero boundary condition. We compute

$$A_n = \frac{2}{(x_2-x_1)\sinh\left(n\pi \frac{x_2-x_1}{y_2-y_1}\right)} \int_{x_1}^{x_2} u_1(x,y_1) \sin\left(n\pi \frac{x-x_1}{x_2-x_1}\right) , \tag{B.6}$$

$$B_n = \frac{2}{(x_2-x_1)\sinh\left(n\pi \frac{x_2-x_1}{y_2-y_1}\right)} \int_{x_1}^{x_2} u_2(x,y_2) \sin\left(n\pi \frac{x-x_1}{x_2-x_1}\right) , \tag{B.7}$$

$$C_n = \frac{2}{(y_2-y_1)\sinh\left(n\pi \frac{y_2-y_1}{x_2-x_1}\right)} \int_{y_1}^{y_2} u_3(x_1,y) \sin\left(n\pi \frac{y-y_1}{y_2-y_1}\right) , \tag{B.8}$$

$$D_n = \frac{2}{(y_2-y_1)\sinh\left(n\pi \frac{y_2-y_1}{x_2-x_1}\right)} \int_{y_1}^{y_2} u_4(x_2,y) \sin\left(n\pi \frac{y-y_1}{y_2-y_1}\right) . \tag{B.9}$$

B.2 Numerical solution

In real applications, the boundary values on each side of the rectangle are available only at a finite number N of equally spaced points. This means that the integrals inside the final solution $u(x,y)$ have to be approximated by the trapezoidal method

$$\int_a^b f(\xi)d\xi \approx \sum_{k=1}^{N} \frac{f(\xi_{k-1}) + f(\xi_k)}{2} \Delta\xi_k . \tag{B.10}$$

Since the function u is defined at N finite and equally spaced points over each side, we can refer to the Discrete Fourier Transform (DFT) theory. It is known that

the DFT of a finite length sequence is linked to the Fourier series coefficients of the continuous periodic signal obtained by repeating and interpolating the original samples. More precisely, the DFT of the N samples comprising one period, equals N times the Fourier series coefficients [15]. In order to satisfy the sampling theorem, and consequently avoid aliasing, the continuous-time signal must be band-limited to less than half the sampling rate: this implies that at most N harmonic components can be nonzero in the original continuous-time signal. For this reason the maximum harmonic order that can be employed is limited, by the number of available samples, at the $(N-1)$-th order.

Appendix B

Appendix C

The Magnetic Potentials

In magnetostatics, one could relate the magnetic field to the magnetic potential by means of two possible formulations, that are the magnetic scalar potential and the magnetic vector potential [16]. We introduce here the two formulation starting from well-known laws, and subsequently we derive that both quantities are harmonic functions which satisfy the two-dimensional Laplace equation.

C.1 The magnetic scalar potential

In classical electromagnetism, the Ampere's circuital law relates the magnetic field $\mathbf{B}$, integrated around a closed loop, to the electric current passing through that loop

$$\oint_{\partial S} \mathbf{B} \cdot d\mathbf{l} = \mu_0 \iint_S \mathbf{J} \cdot d\mathbf{S} \ . \tag{C.1}$$

The application of the divergence theorem to the integral form (C.1) leads to the differential form

$$\nabla \times \mathbf{B} = \mu_0 \ \mathbf{J} \ , \tag{C.2}$$

which states that the curl of a vector field $\mathbf{B}$ is proportional to the current density $\mathbf{J}$. At this point one can introduce a potential function ϕ_m from which the magnetic field can be easily determined

$$\mathbf{B} = \nabla \phi_m \ . \tag{C.3}$$

Since the curl of any gradient is identically zero, in order to do not conflict to the previous results it must be

$$\nabla \times (\nabla \phi_m) = \mu_0 \ \mathbf{J} = 0 \ , \tag{C.4}$$

which means that the magnetic scalar potential must be defined in a region free of sources

$$\mathbf{B} = \nabla \phi_m \qquad (\mathbf{J} = 0) \ . \tag{C.5}$$

Another important law for magnetism is the Gauss' law

$$\oiint_S \mathbf{B} \cdot d\mathbf{S} = 0 \ . \tag{C.6}$$

The equivalent differential form of (C.6) is

$$\nabla \cdot \mathbf{B} = 0 \ , \tag{C.7}$$

which states that the magnetic field has divergence equal to zero, or in other words, that it is a solenoidal vector field. Consequently, by definition, the divergence of the gradient of the scalar potential of (C.5) is also zero

$$\nabla \cdot \mathbf{B} = \nabla \cdot \nabla \phi_m = 0 \ . \tag{C.8}$$

Follows that, in a region free of sources, the magnetic scalar potential obeys

$$\nabla^2 \phi_m = 0 \ , \tag{C.9}$$

where the operator ∇^2 is called Laplacian and is defined as the divergence of the gradient of a function on Euclidean space.

C.2 The magnetic vector potential

From the theorem of divergence-less fields, if the divergence of a vector field $\mathbf{B}$ vanishes, then $\mathbf{B}$ can be expressed as the curl of a vector potential $\mathbf{A}$

$$\mathbf{B} = \nabla \times \mathbf{A} \ . \tag{C.10}$$

Kelvin-Stokes' theorem relates the surface integral of the curl of a vector potential, over a surface S, to the line integral of the vector potential over its boundary ∂S (Fig. C.1)

$$\iint_S (\nabla \times \mathbf{A}) \cdot \mathbf{n} \ dS = \oint_{\partial S} \mathbf{A} \cdot d\mathbf{r} \ . \tag{C.11}$$

Since the potential $\mathbf{A}$ is not uniquely defined by (C.10), an additional condition must be imposed. In magnetostatics, a convenient condition which makes the calculations easier is [17]

$$\nabla \cdot \mathbf{A} = 0 \ . \tag{C.12}$$

The combination of (C.2), (C.10) and (C.12) with the equality

$$\nabla \times (\nabla \times \mathbf{A}) = \nabla (\nabla \cdot \mathbf{A}) - \nabla^2 \mathbf{A} \ , \tag{C.13}$$

yields to the definition of the Laplacian of the vector potential $\mathbf{A}$ in a region free of sources

$$\nabla^2 \mathbf{A} = 0 \quad (\mathbf{J} = 0) \ . \tag{C.14}$$

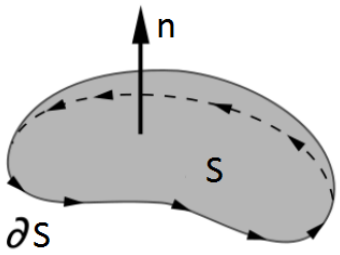

Figure C.1: Integral surface and oriented boundary for (C.11).